Strojniški vestnik

Journal of Mechanical Engineering

no. 5
year 2016
volume 62

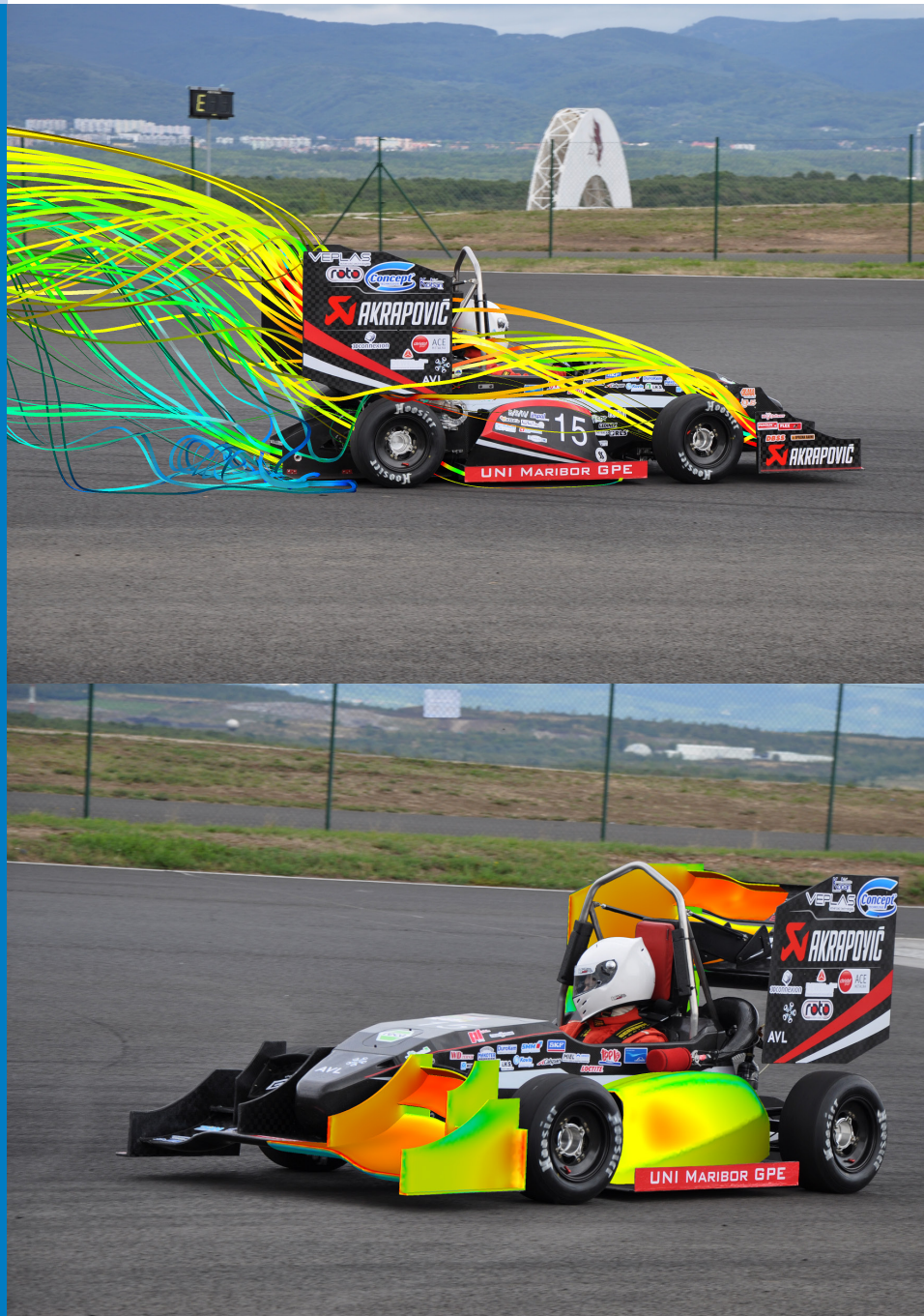

Strojniški vestnik – Journal of Mechanical Engineering (SV-JME)

Aim and Scope
The international journal publishes original and (mini)review articles covering the concepts of materials science, mechanics, kinematics, thermodynamics, energy and environment, mechatronics and robotics, fluid mechanics, tribology, cybernetics, industrial engineering and structural analysis.
The journal follows new trends and progress proven practice in the mechanical engineering and also in the closely related sciences as are electrical, civil and process engineering, medicine, microbiology, ecology, agriculture, transport systems, aviation, and others, thus creating a unique forum for interdisciplinary or multidisciplinary dialogue.
The international conferences selected papers are welcome for publishing as a special issue of SV-JME with invited co-editor(s).

Editorial Office
University of Ljubljana, Faculty of Mechanical Engineering
SV-JME, Aškerčeva 6, SI-1000 Ljubljana, Slovenia
Phone: 386 (0)1 4771 137
Fax: 386 (0)1 2518 567
info@sv-jme.eu, http://www.sv-jme.eu

Print: Grafex, d.o.o., printed in 310 copies

Founders and Publishers
University of Ljubljana, Faculty of Mechanical Engineering, Slovenia
University of Maribor, Faculty of Mechanical Engineering, Slovenia
Association of Mechanical Engineers of Slovenia
Chamber of Commerce and Industry of Slovenia, Metal Processing Industry Association

Cover: The cover shows the aerodynamic package and performance of UNI Maribor GPE formula SAE. The top figure shows the streamlines from the front wing and how the front wing affects the rear one. It can be seen that the front wing is pushing the air under the rear wing, which helps to improve the rear wing downforce. The bottom figure shows the pressure distribution on the side pods, front and rear wing, from where we can observe the effect of end plates and Gurney flaps.

Image Courtesy:
Jurij Iljaž, University of Maribor,
Faculty of Mechanical engineering, Slovenia

ISSN 0039-2480

General information
Strojniški vestnik – Journal of Mechanical Engineering is published in 11 issues per year (July and August is a double issue).

Institutional prices include print & online access: institutional subscription price and foreign subscription €100,00 (the price of a single issue is €10,00); general public subscription and student subscription €50,00 (the price of a single issue is €5,00). Prices are exclusive of tax. Delivery is included in the price. The recipient is responsible for paying any import duties or taxes. Legal title passes to the customer on dispatch by our distributor.

Single issues from current and recent volumes are available at the current single-issue price. To order the journal, please complete the form on our website. For submissions, subscriptions and all other information please visit: *http://en.sv-jme.eu/.*

You can advertise on the inner and outer side of the back cover of the journal. The authors of the published papers are invited to send photos or pictures with short explanation for cover content.

We would like to thank the reviewers who have taken part in the peer-review process.

The journal is subsidized by Slovenian Research Agency.

Strojniški vestnik - Journal of Mechanical Engineering is available on http://www.sv-jme.eu, where you access also to papers' supplements, such as simulations, etc.

Contents

Strojniški vestnik - Journal of Mechanical Engineering
volume 62, (2016), number 5
Ljubljana, May 2016
ISSN 0039-2480

Published monthly

Papers

Jurij Iljaž, Leopold Škerget, Mitja Štrakl, Jure Marn: Optimization of SAE Formula Rear Wing 263
Ayyanar Athijayamani, Raju Ganesamoorthy, Konda Thulasiraman Loganathan, Susaiyappan Sidhardhan: Modelling and Analysis of the Mechanical Properties of Agave Sisalana Variegata Fibre / Vinyl Ester Composites Using Box-Behnken Design of Response Surface Methodology 273
Van Tuan Do, Le Cuong Nguyen: Adaptive Empirical Mode Decomposition for Bearing Fault Detection 281
Luca Petan, José Luis Ocaña, Janez Grum: Effects of Laser Shock Peening on the Surface Integrity of 18 % Ni Maraging Steel 291
K Priya Ajit, Abhinav Gautam, Prabir Kumar Sarkar: Ductile Behaviour characterization of Low Carbon Steel: a CDM Approach 299
David Kaljun, Jože Petrišič, Janez Žerovnik: Using Newton's Method to Model the Spatial Light Distribution of an LED with Attached Secondary Optics 307
Mohammadreza Kamali, Seyed Ali Jazayeri, Farid Najafi, Kenji Kawashima, Toshiharu Kagawa: Study on the Performance and Control of a Piezo-Actuated Nozzle-Flapper Valve with an Isothermal Chamber 318

Strojniški vestnik - Journal of Mechanical Engineering 62(2016)5, 263-272

DOI:10.5545/sv-jme.2016.3240 Original Scientific Paper
Received for review: 2015-11-25
Received revised form: 2016-03-10
Accepted for publication: 2016-04-01

Optimization of SAE Formula Rear Wing

Jurij Iljaž – Leopold Škerget – Mitja Štrakl – Jure Marn
University of Maribor, Faculty of Mechanical Engineering, Slovenia

The main goal of this work was to prove the superiority of a slat vs. a second rear flap in the SAE formula rear wing design, combined with a 3D curved rear flap, for low velocities, by optimization of the rear wing design. Two different main designs were compared, with five different height positions of the main wing and complete analysis carried out of the attack angle on wing performance. A numerical approach was used to test the hypothesis with 3D shear stress transport (SST) Reynolds-averaged Navier-Stokes (RANS) simulation, incorporating the whole formula.

A practical use of this work is in designing a rear wing for maximum downforce within the available rules and regulations. It was found that the multi-element wings were suitable for low speeds and that the base design with two flaps should not be positioned too low. The downforce increases with the height of the wing and reaches its maximum value at 8° angle of attack. For this reason, the new curved design was proposed, including a slat and only one flap. The new wing can cope with a greater angle of attack, has a greater lift coefficient, as well as greater maximal downforce. The advanced design resulted in an increase of downforce of about 6 % at the same wing height.

Keywords: Reynolds-averaged Navier-Stokes equations, rear wing, optimization, computational fluid dynamics, downforce, aerodynamics

Highlights

- *Two different designs for multi-section rear wing in SAE formula are presented.*
- *Several different layouts were analyzed.*
- *The addition of a slat at the expense of a second flap results in significant increase of downforce (about 6 %).*
- *Boundary layer separation causes a significant decrease in lift, and occurs for higher angles of attack in the case of using a slat as opposed to the case without a slat and with the second flap.*

0 INTRODUCTION

This work deals with taking advantage of the available numerical methods when trying to excel in automotive competition. First, the optimization problem is outlined, to be followed by the proposed numerical solution, as well as the practical consequences of this solution, not as a proof of validity of the numerical approach, but rather as a description of a modern design flow.

Formula SAE is an international competition having the common goal of designing and manufacturing of a racing car. While efforts have been made to keep the average velocity as low as possible, for safety reasons (around 50 km/h), by designing an especially tortuous track, there is fierce competition among competitors. This, rather low, velocity presents an additional challenge before the designer – increasing downforce results in higher corner speeds, and this, in turn, leads to better final times during the competition. The design criterion was, therefore, to construct, and manufacture a vehicle which exerted as much downforce as possible.

The body of work related to the rear wings has been performed at Monash University see Wordley and Saunders **[1]**. However, their work covered 2D computational fluid dynamics (CFD) analysis citing availability of a full-scale wind tunnel. This approach, while completely understandable, is not suitable for those without access to such expensive facilities. We believe and have proven in this work, that similar results can be achieved using full-scale 3D CFD modeling. In addition, we believed that modeling rotating wheels and a moving road were absolutely necessary in order to achieve meaningful results. Also, Wordley and Saunders **[1]** were not concerned with optimization of height but were rather changing the angle of attack, such approach being understandable for wind tunnel tests.

Doddegowda et al. **[2]** have also shown generally agreeable computational results without focusing on particular parts of the car. On the contrary, De Silva et al. **[3]** used CFD for fine-tuning of side panels in order to maximize the use of cooling air. They used moving ground however, not spinning wheels, which, in our opinion, is absolutely necessary to capture the vortex formation around the side walls of the car. The importance of a rotating wheel was, albeit from a different perspective, confirmed by Huminic and Chiru **[4]**.

The surprising scientific result shown herein is that the effect of the slat was more pronounced than the effect of the second flap, for the maximum angle of attack, at the upmost main rear wing position, and this is documented herein. Unfortunately, the final design could not incorporate this result as this would

*Corr. Author's Address: University of Maribor, Faculty of Mechanical Engineering, Smetanova ulica 17, 2000 Maribor, Slovenia, jurij.iljaz@um.si

have violated the rules relating to the maximum height of the vehicle; one lower position was therefore chosen for the angle of attack analysis. It should be noticed that slat configuration is not used in Formula 1 competition as technical rules [5] specifically prohibit any structure behind the rear wheel centerline comprised of more than two closed sections (Rule 3.10.1.a):

"When viewed from the side of the car, no longitudinal vertical cross-section may have more than two sections in this area, each of which must be closed". No such limitation exists for the SAE formula.

Hence, this work deals with the rear wing optimization of the SAE formula, and its effect on the downforce of the formula. Such an approach requires the existence of a full-scale numerical model of a formula as opposed to only a rear wing model. The model therefore comprises a front, as well as rear wing, undertray with rear diffusor, monocoque including safety cage, side pods, driver, and rotating wheels. Marn and Iljaž [6] have shown that rotating wheels contribute significantly to suction pressure behind the truck trailer, and the same conclusions are (even more) applicable in this case as the wheels for the SAE formula show no enclosure.

To limit the scope of this problem to manageable size we are concerned only with optimization of rear wing, the rest of the model remains the same. Our objective function is total force on the ground as this force is related directly to tire grip and, consequently, the ability of the vehicle to carry more corner speed.

The optimization was performed with CFD using the Reynolds-averaged Navier-Stokes (RANS) shear stress transport (SST) model. The integral parameter deciding the final question was amplitude of the downforce, because even a small increase in downforce is extremely important to the cornering performance of the car. However, the drag was not discontinued or omitted as the numerical simulation was fully 3D. It should also be stated that the power consumption by the drag at these low vehicle speeds was negligible and, therefore, had a very small effect on the acceleration of the car, which is also one of the reasons why the drag was neglected in the design evaluation.

Literature search reveals that in addition to Wordley and Saunders [1], Venkatesan et al. [7] report on wing profiles and ground effect in cars, Hu and Wong [8] report on the rear wing effect on a personal vehicle, and Kieffer et al. [9] report on front and rear wings in Formula Mazda. It should be stressed, however, that the latter works are only concerned with high speeds, which is not applicable in this case. A comprehensive study was performed by Jensen, [10] who was concerned with undertray analysis. None of the studies found were concerned with 3D rear wing optimization varying distance from the ground, and/or comparing effects of slat vs. second flap.

The results of Wordley and Saunders [1] prove that 2D analysis is, basically, useful only for prediction of general behavior. Huminic and Chiru [4] prove that it is necessary to model spinning wheels as well as a rolling road. In order to compose a suitable model we must therefore explore full 3D analysis, with moving road and spinning wheels, in addition to varying parameters such as distance of rear wing from the ground and angle of attack, as well as adding of a slat in front of the main wing in the rear wing assembly.

Based on the foregoing we explored some more general studies in order to get an insight into neighboring studies.

Zvar Baskovic et al. [11] investigated the use of different turbulence models with different treatment near the wall to do RANS simulation of adiabatic flow in an air-conditioned vehicle compartment. Their findings are that SST $k-\omega$ model provides the best overall performance, despite the needed evaluation.

Bizjan et al. [12] tested a flow image Velocimetry method based on advection-diffusion equation, on a much simpler airfoil than ours and compared the results with the CFD RANS simulation. They found that the used SST model provides good agreement with measured data for mean flow and that the used Velocimetry method is in good agreement with the true velocity field. The paper also shows a promising way of developing a new optical flow measurement method for aerodynamic.

Jošt et al. [13] also discussed about the appropriate turbulence model for Kaplan turbine, where the RANS-SST model showed significantly better results than the usually used $k-\varepsilon$ turbulence model.

In addition, the above referenced CFD studies only referred to straight wings (without 3D curvature) our advance design is also concerned with 3D curvature of the main wing and rear flap just to increase the angle of attack at both sides, to gain some downforce of the undisturbed flow which will be discussed later.

1 BASIC AND ADVANCED DESIGNS

Basic and advanced designs are shown in Figs. 1, and 2, respectively.

In the past the aerodynamic theory was first developed for airplanes. As no or very limited

computational tools were available, general equations were developed in order to compare different designs quickly. Aerodynamic force reads ([14] and [15]):

$$F_i = \frac{1}{2} \cdot C_i \cdot \rho \cdot A \cdot v^2, \quad (1)$$

where F_i is horizontal or vertical aerodynamic force (F_L represents lift or downforce and F_D drag), ρ fluid density, A characteristic surface area, v characteristic velocity, and C_i aerodynamic coefficient (C_L represents lift and C_D drag coefficient). In our case negative lift force is produced by the wing, and called downforce; the force with which the tires press onto the surface. Without the downforce the highest lateral acceleration of a car possible to withstand is around g. Tight curves cause an acceleration component in a radial direction to exceed g quickly resulting in under- or oversteering of a vehicle.

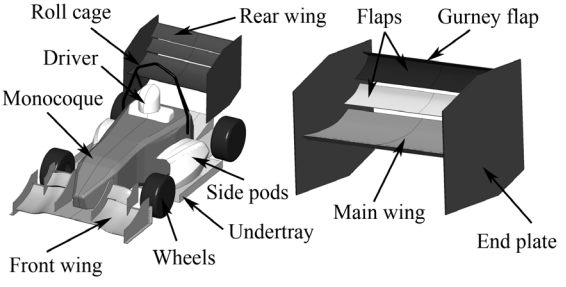

Fig. 1. *Basic design*

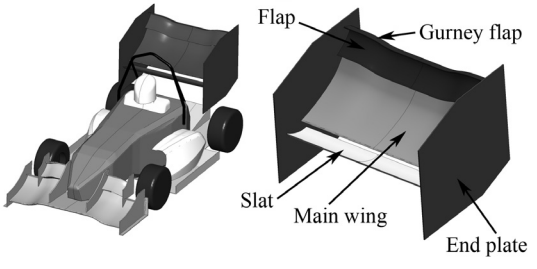

Fig. 2. *Advanced design*

This aerodynamic force can be increased by increasing any of the right-hand side components of Eq. (1). As density and velocity variations (fluid is air, velocity is low) are limited, the only components remaining are surface area and lift coefficient. The obvious variation, the surface area of the wing is limited by regulations. Current SAE regulations [16] limit the wing not to exceed 1.2 m distance from the ground, being wider than the distance between the inner sides of the rear wheels, or exceeding 250 mm in length measured from the end of the rear wheels. Of course, increasing the surface area to maximum makes sense but the real challenge is to construct a wing which would increase the lift coefficient beyond current, and readily available designs.

There are limitations, of course. Wordley and Saunders [1] present convincing arguments showing that, in general, the angle of attack increases downforce up to the point of stalling (flow separation). To prevent this, the wing was separated in several sections (main wing, flaps, slats etc.). It is well known that single section wings achieve $C_L \approx 1$, while multiple section wings arrive at much higher lift coefficients, i.e. $C_L \approx 2$ to 3 due to larger curvature of the wing and angle of attack (Katz [14] and [15] and McBeath [17]). As a consequence, we decided to use a three section rear wing as a compromise between manufacturing capabilities having sufficient material strength, and increased angle of attack.

In order to arrive at a qualitative solution of multi-element airfoil profile we had to perform simplified analysis due to the lack of actual data in open literature. First, we used 2D computations taking advantage of the potential flow based computer code JavaFoil 2.18 which simulates an arbitrary profile, including a multi-section one. For the basic profile, a NACA 63A-2010 was chosen with the flap presenting 33 % of the main wing surface area, and overlap of sections of about 6 %. After that, we evaluated the design multi-element airfoil profile with 2D SST RANS simulation using Ansys CFX 15.0 computer code.

The last step was a set of full 3D calculations of the airfoil profile to arrive at the basic design of rear wing composed of a main wing, two flaps, end plates and Gurney flap attached to the last section. The wing is 970 mm long and 710 mm wide.

Granted, the wing looks much different from what we are accustomed to from Formula 1 or sports cars design, but the difference is in the different treatment of Eq. (1) in Formula 1 (and in the sports car business) the downforce is increased by increasing the velocity and not the surface area, or lift coefficient as in the present case.

For the advance design, we exchanged the last section (second flap) with a slat in front of the main wing, as can be seen from Figs. 1 and 2.

The flaps prevent flow separation and turn flow upward to simulate a larger angle of attack. The slat feeds flow below the main wing in order to prevent stalling, enabling the main wing to attain a higher angle of attack.

2 GOVERNING EQUATIONS

In order to solve the problem at hand the following well-known governing equations were solved [18]. Mass conservation equation:

$$\frac{\partial \rho}{\partial t} + \nabla \cdot (\rho \mathbf{v}) = 0, \tag{2}$$

where ρ is density, t is time, ∇ gradient, $\nabla \cdot$ divergence and $\mathbf{v}$ velocity. Momentum conservation can be written as:

$$\rho \left[\frac{\partial \mathbf{v}}{\partial t} + (\mathbf{v} \cdot \nabla)\mathbf{v} \right] = \rho \cdot \boldsymbol{f}_m - \nabla p + \nabla \cdot \boldsymbol{\tau}, \tag{3}$$

where $\boldsymbol{f}_m$ is body force, p pressure and $\boldsymbol{\tau}$ stress tensor. Taking account for Newtonian fluids having symmetry of stress tensor in mind:

$$\boldsymbol{\tau} = \eta \left(2\nabla \mathbf{v} - \frac{2}{3}\delta \nabla \cdot \mathbf{v} \right), \tag{4}$$

where η is dynamic viscosity and δ is Kronecker delta function without units.

Turbulence was modeled using $k-\omega$ based SST model. $k-\omega$ model links turbulence kinetic energy k and its frequency ω via the relation:

$$\eta_t = \rho \frac{k}{\omega}, \tag{5}$$

where η_t is turbulence viscosity and ρ fluid density. Two transport equations, for turbulence kinetic energy and its frequency, were modeled by Wilcox [19] in the following terms:

$$\frac{\partial (\rho k)}{\partial t} + \nabla (\rho \mathbf{v} k) = \\ = \nabla \left[\left(\eta + \frac{\eta_t}{\sigma_k} \right) \nabla k \right] + P_k - \beta' \rho k \omega + P_{kb}, \tag{6}$$

$$\frac{\partial (\rho \omega)}{\partial t} + \nabla (\rho \mathbf{v} \omega) = \\ = \nabla \left[\left(\eta + \frac{\eta_t}{\sigma_\omega} \right) \nabla \omega \right] + \alpha \frac{\omega}{k} P_k - \beta' \rho \omega^2 + P_{\omega b}, \tag{7}$$

where α, β', σ_k and σ_ω are model constants. The stress tensor is then computed from the Eddy viscosity concept.

The SST model implements a limiter to the formulation of Eddy viscosity, and decreases its over prediction, due to not accounting for the transport of turbulent shear stress. Limited Eddy viscosity is formulated in following form:

$$\nu_t = \frac{a_1 k}{\max (a_1 \omega, SF_2)}, \tag{8}$$

where a_1 is a model constant, $\nu_t = \eta_t / \rho$ turbulence kinematic viscosity, F_2 is a blending function which restricts the limiter to the wall boundary layer and S is an invariant measure of the strain rate.

3 NUMERICAL MODEL

A commercial 3D CFD solver, Ansys CFX 15.0, was used for solving the above referenced governing equations. While we were only concerned with the rear wing, the whole SAE formula was modeled, including rotating wheels. This approach enables a designer to "freeze" the best design of a particular element, and adjusts the other aerodynamic element in order to arrive at the best solution.

Conceptually the governing equations can be treated as parabolic although in fact they are not, but contribution of the upstream flow disturbance is far lower than downstream. This also means that the effect of design changes made on the rear wing will not propagate upstream strongly enough to have an important effect on the front wing or undertray. Therefore, ideally, one would start with designing of the front wing, followed by side pods, undertray, and finally the rear wing.

We have used RANS-SST simulation. Other turbulence models could be used but we opted for SST as we believe that it describes turbulence better close to the wall and allows for better prediction of boundary layer separation, and this, in turn, results in a better description of the recirculation zone and overall downforce. Galilean transformation was applied, and wheels were assumed to rotate with appropriate velocity.

Simplification of the problem is in assuming that the vehicle is moving straight forward. While turning would not have presented significant additional computational effort and would far better describe actual conditions on track such results would be hardly comparable to any other published results.

The numerical domain is seen in Fig. 3 and it is comprised of a vehicle representing the SAE formula, and its immediate environment. The domain is split symmetrically under the assumption that, as no cross wind is modelled, the results should be symmetrical. Strictly speaking, this is not entirely so; vortex shedding may occur alternately. However, as computation was in a steady state, this assumption was considered acceptable. In order to prevent wall effects the computational domain was 16.4 m in

length, 5.8 m in width (double width), and 4.5 m in height. The outer dimensions of SAE formula were 2.8 m in length, 1.4 m in width, and 1.2 m in height; about five length of car was modeled after the vehicle.

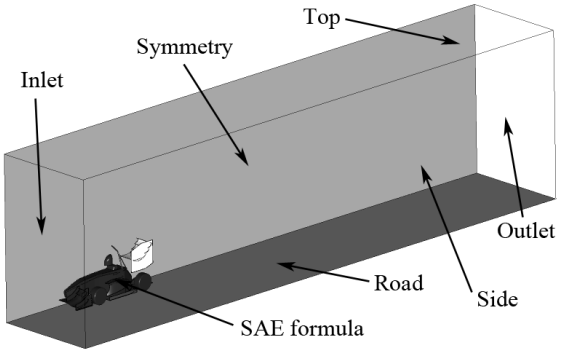

Fig. 3. *Computational domain*

The speed of the vehicle was 14 m/s which corresponds to 50 km/h which is average velocity during the competition. Boundary conditions were uniform flow at the entrance into the computational domain (inlet), open boundary condition (pressure 0 Pa) at the exit out of the computational domain (outlet), slip boundary condition on the top and side wall, symmetry boundary condition at the symmetry border, and no-slip boundary condition on the moving road with the speed of the vehicle.

No-slip boundary condition was present throughout the formula's surfaces with the exception of the wheels. Wheels were assumed smooth, and were assumed to rotate with constant velocity – this velocity was 61.4 rad/s for wheels with an outer diameter of 456.8 mm.

Non-structured mesh was used for discretization of the computational domain, and particular effort was paid to discretization of wings and other aerodynamically relevant elements. Computational mesh was generated with the commercial package ICEM CFD 15.0.

In order to achieve comparable results, mesh and domain analyzes should be performed. The mesh analyze is presented in Tables 1 and 2, and domain analyze in Table 3. We compared the produced downforce and drag of the rear wing among different mesh and domain sizes.

Mesh size was varied between about 2.2 million elements to about 14.4 million elements, distributed among various parts of the vehicle and environment (see Table 1), and domain size (Fig. 3) was varied between box length of 8.4 m to 16.4 m, box half-width of 1.5 m to 2.9 m, and box height of 3 m to 4.5 m.

In order to perform mesh analyze we had to fix domain size, and check for the parameter value varying mesh size. We fixed domain size at $D3$ (i.e. 10.4 m in length, 2.4 m in half-width and 4 m in height). We actually observed five predetermined parameters, namely forces on main wing, on flaps 1 and 2, downforce on the rear wing and drag, respectively. Table 2 shows that while force on main wing was increasing monotonously, the forces on the flaps were oscillating around the same value. However, we can observe the convergence of the downforce and drag of the rear wing. Based on this, and taking into account available resources we decided on mesh m3.

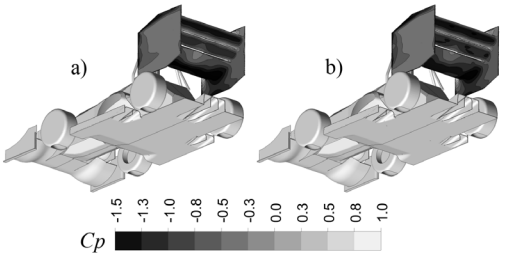

Fig. 4. *Pressure distribution over rear wing (bottom side): a) m3, and b) m4*

Fig. 4 shows the qualitative difference between meshes, showing the pressure coefficient C_P (Katz [14] and [15]). We observed that the difference between most fine meshes was minimal; looking globally the pressure distribution was the same.

After the decision to use mesh m3 was made, we focused on domain size analyze. Varying the box size, we found that downforce and drag of the rear wing converged with increasing domain size and that there was small variance between the domain D4 and D5 (see Table 3). However, we decided to go with the largest box size, as the increase was not prohibitive.

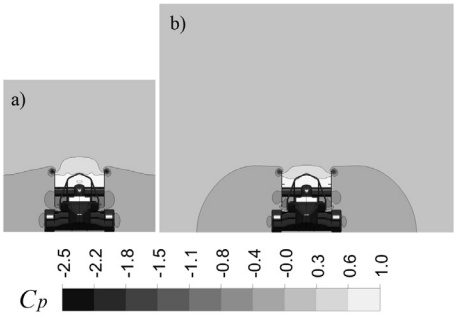

Fig. 5. *Pressure field: a) D1, and b) D5*

Fig. 5 shows clearly the reason for the variation. From Fig 5a one can observe that the isobars intersect

Table 1. *Mesh properties*

Element size [mm]	m0	m1	m2	m3	m4
Monocoque	40	32	25	20	16
Wing	24	19	15	12	10
Undertray	40	32	25	20	16
Road	90	72	57	45	36
Cage	12	9.5	7.5	6	5
Air	240	190	150	120	100
Surroundings	120	95	75	60	50
Number of elements	2,246,162	3,629,026	5,084,677	9,702,520	14,409,563
Number of nodes	516,806	822,227	1,097,061	2,152,744	3,252,490

Table 2. *Mesh analyze on domain D3*

Mesh analisys	m0	m1	m2	m3	m4
F_{main} [N]	55.3	71.0	86.0	89.8	90.8
F_{flap1} [N]	24.4	26.2	24.5	28.8	28.5
F_{flap2} [N]	13.8	15.2	14.9	15.0	16.2
F_{DWN} [N]	93.3	112.2	125.2	133.4	134.8
F_{DRAG} [N]	53.0	57.0	57.0	61.1	61.6

with the border of the domain meaning that borders were actually treated as walls. The Fig. 5b shows correct pressure field distribution, hence the decision for D5 domain size. Mesh and domain analyze showed a variation of parameter value, which was not strictly monotonic.

The absence of monotonic change (either increase or decrease) is considered as a telltale that changes are no longer dependent on mesh or domain size and that further increase in node numbers or decrease in mesh size on one hand or further increase in domain size on the other hand do not yield desirable results.

Based on these results, the mesh m3 on the domain D5 with 12,484,513 elements was used, with lower aspects ratios close to the SAE formula boundary, and higher aspect ratios away. The ratio between the largest and smallest elements was about 10:1.

4 RESULTS AND DISCUSSION

First, basic design was analyzed. The results are summarized in Tables 4 and 5 for the effect of main wing height (distance from ground) and angle of attack, respectively.

We fixed the angle of attack at 10° and varied the main wing distance from the ground in order to find the dependence of various forces on rear wing parts on this variation. The results are presented in Table 4 and Fig. 6. The conclusion here is that the rear wing should be positioned as high as possible, to minimize the effect of other elements like driver, monocoque etc.

Based on these results, and taking note of regulation height limitation, along with the existence of two flaps after the main wing, we decided for the maximum height of 760 mm. This also allowed us to increase the angle of attack slightly, and to stay within the regulation window. The next parameter which could be varied was the angle of attack (AOA). The results are summarized in Table 5 and Fig. 7. We decreased the angle step around the maximum performance angle, to see the stalling point. The stalling occurs at 11° for a height of 760 mm.

Taking downforce as a deciding factor, we concluded that the best scenario for base design is high main wing position (760 mm) and an 8° angle of attack.

Table 3. *Domain analyze*

Domain size [m]	D1	D2	D3	D4	D5
	8.4/1.5/3.0	9.4/1.9/3.5	10.4/2.4/4.0	11.4/2.9/4.5	16.4/2.9/4.5
F_{main} [N]	113.0	101.6	89.8	92.6	93.8
F_{flap1} [N]	31.1	28.5	28.8	25.5	23.8
F_{flap2} [N]	16.5	15.3	15.0	14.5	14.1
F_{DWN} [N]	160.4	145.3	133.4	132.6	131.5
F_{DRAG} [N]	69.5	63.5	61.1	58.0	56.1

The notations in the graphs in Figs. 6 and 7 show "base" for basic design, "CL" for lift coefficient, "CD" for drag coefficient, "advanced" for advanced design and "no-fw" for no-front-wing construction.

Table 4. *Effect of rear wing height for basic design (10° AOA)*

h [mm]	670	700	730	760	790
F_{main} [N]	76.5	93.8	95.8	112.5	121.41
F_{flap1} [N]	25.8	23.8	29.5	30.0	30.8
F_{flap2} [N]	14.6	14.1	15.4	18.3	16.0
F_{DWN} [N]	116.6	131.5	140.7	160.9	168.3
F_{DRAG} [N]	54.9	56.1	59.6	63.2	66.8

In order to explain the reasons better several figures are presented. Fig. 8 shows pressure field

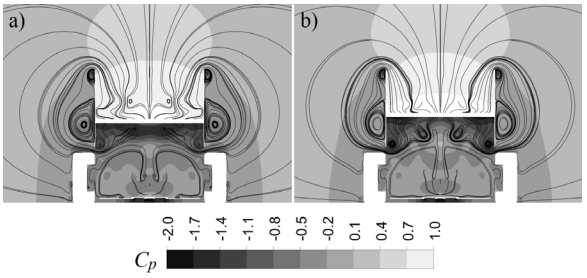

Fig. 8. *Pressure field for base wing: a) 700 mm, and b) 760 mm*

Table 5. *Effect of AOA for basic design (760 mm)*

AOA [°]	0	4	7	8	9	10	11	12	13	16
F_{main} [N]	91.3	98.5	113.0	114.9	113.1	112.5	89.8	95.8	82.5	82.0
F_{flap1} [N]	29.2	28.9	30.0	29.8	30.1	30.0	30.9	30.2	32.3	28.5
F_{flap2} [N]	21.2	19.3	18.2	17.5	17.9	18.3	13.9	13.6	14.6	12.7
F_{DWN} [N]	141.5	159.1	161.4	162.4	161.1	160.9	134.3	139.4	128.9	122.6
F_{DRAG} [N]	40.7	53.9	56.0	58.3	61.3	63.2	66.1	70.9	74.4	78.1

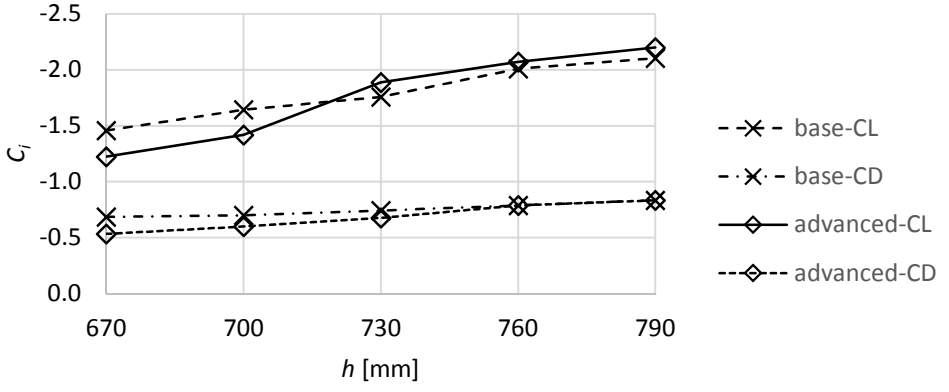

Fig. 6. *Lift and drag coefficients as functions of height*

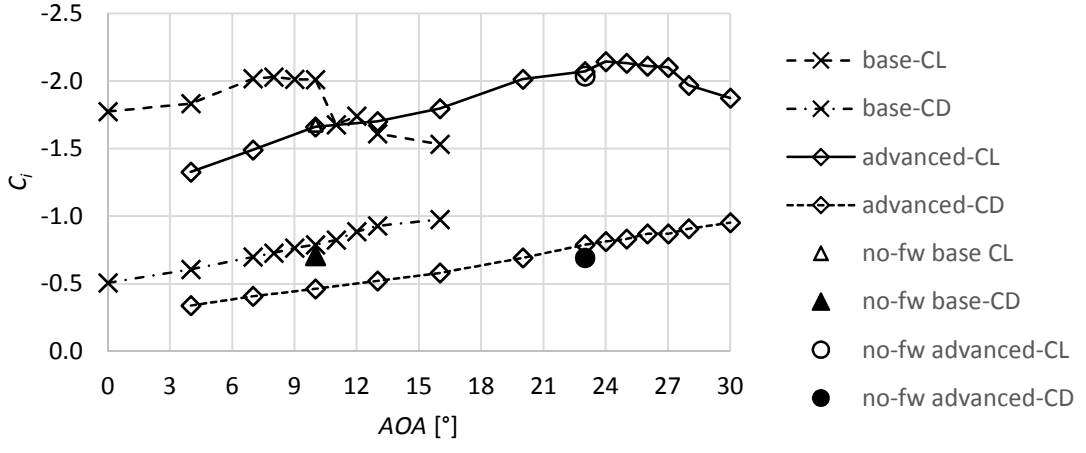

Fig. 7. *Lift and drag coefficients as functions of AOA*

variation with plotted streamlines. One can see the development of side vortices and decreased static pressure under the wing with increased height. We can also observe several vortices, especially on the top of the end plate, producing low-pressure region inside the center, which reflects the strength of vortex.

Fig. 9 shows the positive effect of increasing the height of the main wing on the reduced effect of recirculation; the smaller the recirculation region beneath the rear wing, the better the ride.

Fig. 10 presents the pressure field difference between the optimal angle of attack 8°, and at the 13° angle, when the stalling occurs. The low end plate vortices are much stronger for the former resulting in lower static pressure at the bottom and consequently higher downforce.

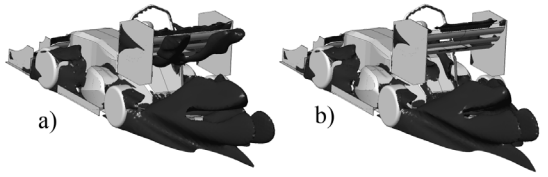

Fig. 9. *Recirculation behind base rear wing: a) 700 mm, and b) 760 mm*

Fig. 11 shows, on the other hand, the negative impact of an increasing angle of attack indiscriminately, showing isosurface of recirculation. The increased angle of attack resulted in stalling; the production of a recirculation region beneath the rear wing, which increased the drag and reduced the downforce drastically.

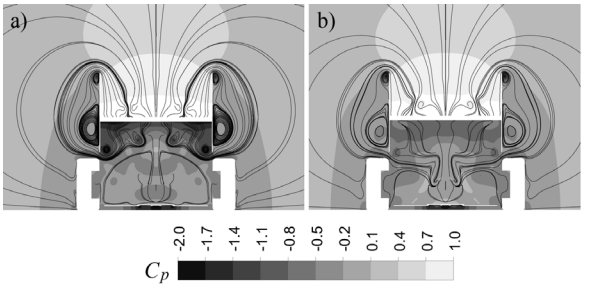

Fig. 10. *Pressure field for base wing: a) AOA 8°, and b) AOA 13°*

Last, but not least, we compared the effect of the front wing. Fig. 12 shows the absence of front wing for base design and 10° AOA. The absence of a front wing eliminates some of the low end-plate vortices and reduces the low static pressure under the wing, which means that the downforce is far smaller, and effects of such change undesirable. The effect of the front wing is much stronger for the base design than for the advanced, as can be seen from the graph in Fig. 7.

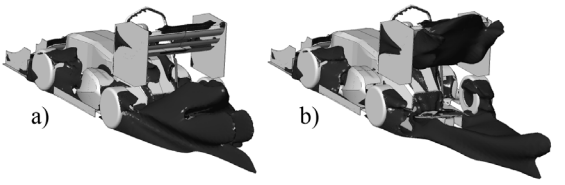

Fig. 11. *Recirculation behind base rear wing: a) AOA 8°, and b) AOA 13°*

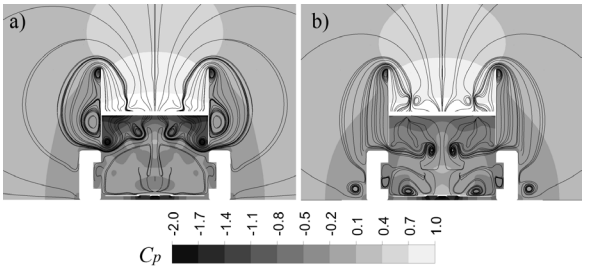

Fig. 12. *Pressure field: a) with, and b) without front wing*

The downforce manifests itself with the formation of side vortices (which is also the main reason why 2D simulation lacked comparison with the experimental data as side vortices are a 3D phenomenon resulting from twisting and stretching term and could not have been predicted with a 2D simulation.

Similar analyze of the advanced design as for that of the basic one yields the results as summarized in Tables 6 and 7, for the effect of main wing height at 23° AOA and main wing angle of attack at height 760 mm, respectively. The results are also presented in Figs. 6 and 7, showing the drag and lift coefficient.

Table 6. *Effect of height for advanced design (23° AOA)*

h [mm]	670	700	730	760	790
F_{main} [N]	61.9	72.8	89.7	104.4	111.8
F_{flap1} [N]	22.9	27.6	42.9	43.9	47.5
F_{flap2} [N]	13.3	13.1	18.2	17.3	16.5
F_{DWN} [N]	97.9	113.4	150.9	165.7	175.8
F_{DRAG} [N]	42.8	48.0	54.3	63.2	66.9

As can be seen from Fig. 7, the basic design suffers from boundary layer separation very early on despite the trend increasing both lift, and drag with increasing angle of attack. This is where the slat comes into play (advanced design). The slat enables much higher angles of attack, which, in turn, increases the formation of side vortices, and they in turn increase total downforce. The logical conclusion (tested, to affirmative, yet not presented herein) is that

Table 7. *Effect of angle of attack for advanced design (760 mm)*

AOA [°]	10	13	16	20	23	24	25	26	27	28	30
F_{main} [N]	91.1	91.9	94.6	103.4	104.4	107.7	105.8	104.5	104.7	95.4	92.4
F_{flap1} [N]	20.9	25.0	30.7	40.2	43.9	47.6	48.3	47.7	49.2	45.7	43.3
F_{flap2} [N]	20.7	19.0	18.2	17.3	17.3	16.3	16.3	16.5	14.1	16.4	14.3
F_{DWN} [N]	132.8	136.1	143.6	161.1	165.7	171.6	170.5	168.8	168.2	157.5	150.0
F_{DRAG} [N]	37.0	41.7	46.6	55.5	63.2	65.0	66.6	69.6	69.7	72.7	76.2

adding additional flap (and violating SAE formula rules) would increase downforce further.

But, also the advanced design is not immune to boundary layer separation which is observed in AOA above 27°. A further increase of AOA results in a decrease in lift, behavior similar to Fig. 11b, formation of recirculation region beneath the rear wing.

While it may be counter intuitive that we are still constrained with 760 mm, this is not so. Namely, the addition of the slat results in a much higher angle of attack, which, in turn, presents the same constraints in height.

The formation of top end-plate side vortices is seen nicely in Fig. 13 for the advanced design at optimal AOA showing streamlines.

Based on these findings we found the best results for advanced design were a height of 760 mm, and 24° AOA. This coincides with the wind tunnel measurement supported findings of Wordley and Saunders **[1]**; of course qualitatively, as quantitative measurements depend on actual wing setup, which was completely different in this case.

Fig. 13. *Streamline formation*

Comparing basic and advanced design we found that eliminating the second flap in favor of a slat, which in turn enables an increasing angle of attack, results in an increase of downforce from 162.4 N to 171.6 N, or an almost 6 % increase! The difference between the base and advanced design at optimal AOA can be also seen from Fig. 14.

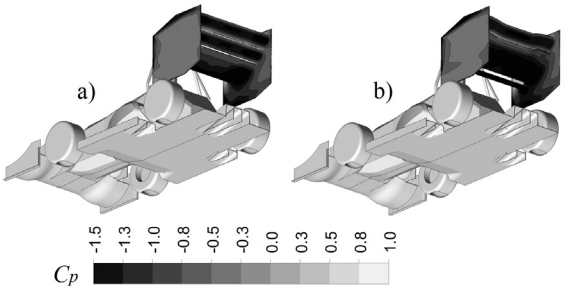

Fig. 14. *Pressure field for a) base, and b) advanced design*

We conclude that for SAE formula to function in optimum regime, the angle of attack should be as high as possible, with wing height also as high as possible. Our greatest fear of rapid boundary layer separation at increased AOA, resulting in drastic reduction of downforce for advanced design, did not materialize.

As a final note, we wish to emphasize that this wing was actually used on track resulting in the 1st position in skidpad (i.e. lateral acceleration), and 1st position in autocross qualification at most race track in the Czech Republic (Fig. 15).

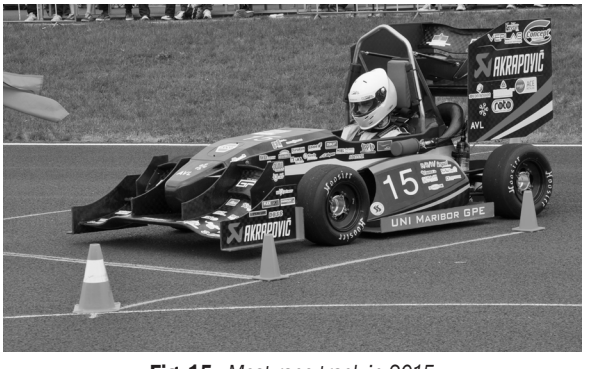

Fig. 15. *Most race track in 2015*

Especially, the skidpad competition is a direct result of a downforce exerted enabling the vehicle to carry high corner speed, which was the aim of this investigation in the first place.

5 CONCLUSIONS

During development of the model there were several lessons learned. First, multi-section wings can be simulated successfully using full-scale 3D numerical modeling, along with SST turbulent flow model, spinning wheels and moving road.

Next, flow separation is the main problem to be expected for development of a rear wing. This problem can be fixed by adding a slat before the main wing instead of the second flap after the first flap.

There is no need to keep main wing basically extruded 2D profile. The 3D wing variation improved results by adding an anti-yaw effect to the end plates.

End plates are as important as a front wing. Without either the side vortices are not developed, and the flow is swept downstream in the form of twisting-and-stretching vortices after the rear wing; while the former increase downforce the latter reduce it.

Provided that flow separation can be avoided, a higher angle of attack and higher main wing position generally lead to higher downforce. However, once flow separation occurs, the effects are immediate, and detrimental.

The main effect of the advanced design is increased downforce and lower sensitivity to sudden flow separation at high AOA, which results in better overall performance.

6 REFERENCES

[1] Wordley, S., Saunders, J. (2006). Aerodynamics for formula SAE: A numerical wind tunnel and on-track study. *SAE Technical Paper*, no. 2006-01-0808, **DOI:10.4271/2006-01-0808**.

[2] Doddegowda, P., Bychkovsky, A., George, A. (2006). Use of computational fluid dynamics for the design of formula SAE race car aerodynamics. *SAE Technical Paper*, no. 2006-01-0807, **DOI:10.4271/2006-01-0807**.

[3] De Silva, C.M., Nor Azmi, M., Christie, T., Abou-saba, E., Ooi, A. (2011). Computational flow modelling of formula-SAE sidepods for optimum radiator heat management. *Journal of Engineering Science and Technology*, vol. 6, no. 1, p. 94-108.

[4] Huminic, A., Chiru, A. (2006). On CFD investigations of vehicle aerodynamics with rotating wheels simulation. *SAE Technical Paper*, no. 2006-01-0804, **DOI:10.4271/2006-01-0804**.

[5] F 1 Technical Regulations. (2014). FIA, from *http://www.fia.com/sites/default/files/regulation/file/2015%20TECHNICAL%20REGULATIONS%202014-12-03.pdf*, accessed on 2015-11-05.

[6] Marn, J., Iljaž, J. (2014). Effect of wheels on flow around truck trailer. *Acta Hydrotehnica*, vol. 27, no. 46, p. 29-41.

[7] Venkatesan, D.V., Sanjay, K.E., Sujith Kumar, H., Abhilash, N.A., Ashwin Ram, D., Sanal Kumar, V.R. (2014). Studies on race car aerodynamics at wing in ground effect. *International Journal of Mechanical, Aerospace, Industrial, Mechatronic and Manufacturing Engineering*, vol. 8, no. 7, p. 1169-1174.

[8] Hu, X.X., Wong, E.T.T. (2011). A numerical study on rear-spoiler of passenger vehicle. *International Journal of Mechanical, Aerospace, Industrial, Mechatronic and Manufacturing Engineering*, vol. 5, no. 9, p. 1800-1805.

[9] Kieffer, W., Moujaes, S., Armbya, N. (2006). CFD study of section characteristics of Formula Mazda race car wings. *Mathematical and Computer Modeling*, vol. 43, no. 11-12, p. 1275-1287, **DOI:10.1016/j.mcm.2005.03.011**.

[10] Jensen, K. (2010). *Aerodynamic Undertray Design for Formula SAE*. MSc thesis, Oregon State University, Corvallis.

[11] Zvar Baskovic, U., Lorenz, M., Butala, V., (2014). Adiabatic flow simulation in an air-conditioned vehicle passenger compartment. *International Journal of Simulation Modelling*, vol. 13, no. 1, p. 42-53, **DOI:10.2507/IJSIMM13(1)4.253**.

[12] Bizjan, B., Orbanić, A., Širok, B., Bajcar, T., Novak, L., Kovač, B. (2014). Flow image velocimetry method based on advection-diffusion equation. *Strojniški vestnik – Journal of Mechanical Engineering*, vol. 60, no. 7-8, p. 483-494, **DOI:10.5545/sv-jme.2013.1614**.

[13] Jošt, D., Škerlavaj, A., Lipej, A. (2014). Improvement of efficiency prediction for Kaplan turbine with advance turbulence models. *Strojniški vestnik – Journal of Mechanical Engineering*, vol. 60, no. 2, p. 124-134, **DOI:10.5545/sv-jme.2013.1222**.

[14] Katz, J. (1995). *Race Car Aerodynamics, Designing for Speed*, Bentley Publisher, Cambridge.

[15] Katz, J. (2006). Aerodynamics of race cars. *Annual Review of Fluid Mechanics*, vol. 38, p. 27-63, **DOI:10.1146/annurev.fluid.38.050304.092016**.

[16] SAE International. 2016 Formula SAE Rules, *from http://www.fsaeonline.com/content/2016_FSAE_Rules.pdf*, accessed on 2016-04-08.

[17] McBeath, S. (2011). *Competition Car Aerodynamics*. Haynes Publishing, Somerset.

[18] Škerget, L. (1994). *Fluid Mechanics*. University of Maribor Technical faculty and University of Ljubljana, Faculty of Mechanical Engineering, Maribor, Ljubljana. (in Slovene)

[19] Wlicox, D.C. (1986). Multiscale model for turbulent flows. *AIAA, 24th Aerospace Sciences Meeting*, **DOI:10.2514/6.1986-29**.

Strojniški vestnik - Journal of Mechanical Engineering 62(2016)5, 273-280

DOI:10.5545/sv-jme.2015.2641 Original Scientific Paper
Received for review: 2015-04-29
Received revised form: 2015-09-22
Accepted for publication: 2015-10-19

Modelling and Analysis of the Mechanical Properties of Agave Sisalana Variegata Fibre / Vinyl Ester Composites Using Box-Behnken Design of Response Surface Methodology

Ayyanar Athijayamani[1,*] – Raju Ganesamoorthy[2] – Konda Thulasiraman Loganathan[3] – Susaiyappan Sidhardhan[4]

[1] Alagappa Chettiar College of Engineering and Technology, Department of Mechanical Engineering, India
[2] Sayasuriya Engineering College, Department of Mechanical Engineering, India
[3] Alagappa Chettiar College of Engineering and Technology, Department of Chemistry, India
[4] Government College of Engineering, Department of Civil Engineering, India

In this paper, the Box-Behnken (BB) experimental design of response surface methodology (RSM) was utilized to study the effect of process parameters on the mechanical properties of agave sisalana variegata (ASV) fibre-reinforced vinyl ester (FRVE) composites. The fibre length, fibre content, and fibre diameter were used as process parameters to develop a model using the BB experimental design. Experimental tests were carried out based on the BB design. The experimental tensile and flexural strength values were fitted with the predicted strength values by a second-order polynomial equation via a multiple regression analysis. The results show that the tensile and flexural strength can be predicted by the developed models with more than 98.54 % of the variation in the tensile strength and 99.24 % of the variation in the flexural strength. The level 3 of fibre length (13 mm), level 2 of fibre content (35.19 wt %), and level 1 of fibre diameter (0.24 mm) were selected as the optimal levels of fabrication process parameters using the response surface graph and models. Finally, it was proved that the BB design of response surface methodology could efficiently be applied to the modelling and optimization of the mechanical properties of natural fibre polymer composites.

Keywords: agave sisalana variegata fibre, composite, tensile strength, flexural strength, Box-Behnken design, response surface methodology

Highlights

- *Agave sisalana variegata fibre-reinforced vinyl ester composite is a new series of polymer composites.*
- *Experimental works were carried out based on the Box-Behnken experimental design of response surface methodology.*
- *Mechanical properties, such as the tensile and flexural strength values of composites, were predicted using a second-order polynomial equation by a multiple regression analysis.*
- *The optimal levels of fabrication process parameters were identified using response surface graph and models.*

0 INTRODUCTION

In recent years, there has been growing interest in the use of plant-based natural cellulose fibers, such as sisal, coir, flax, cotton, hemp, jute, kenaf, pineapple, ramie, bamboo, bagasse, roselle, banana and others. as reinforcing agents for polymer resin matrix such as thermoplastics and thermosets **[1]** and **[2]**. Their merits make them an attractive ecological alternative to man-made synthetic fibres used for the manufacturing of composites **[3]** and **[4]**.

Among the various natural fibres, the sisal fibre (*Agavaceae* family) is an important, environmentally friendly and biodegradable one. Moreover, sisal is a strong, stable, and versatile material, and it has been recognized as an important source of fibre for the preparation of composites **[5]** and **[6]**. The agave sisalana variegata plant is also one of the most important families of *Agavaceae*, and it has the same features as regular sisalana. People use these plants as a nursery plant in their gardens and lands. The fibres are produced from the leaves of these plants. There is no literature available on the characteristics of agave sisalana variegata (ASV) fibre-reinforced vinyl ester (FRVE) composites.

Generally, the properties of fibre-reinforced polymer composites can be varied continuously over a broad range of values under the control of their process parameters and conditions. Careful selection of process parameters, such as fibre length, fibre volume or weight fraction, the fibre aspect ratio, the nature of the matrix, and fibre-matrix interface, etc., enables finished composite characteristics to be tailored to almost any specific applications. The main objective of this study is to focus on the effects of process parameters such as fibre length, fibre content, and fibre diameter on the tensile strength and flexural strength of ASVFRVE composites. Several authors have been used the BB design of response surface methodology (RSM) to understand better the relationship between the parameters and the response and also to optimize the parameters of the technology in various materials **[7]** and **[8]**. In order to have the better understanding and to determine mechanical

*Corr. Author's Address: Alagappa Chettiar College of Engineering and Technology, Department of Mechanical Engineering, India, athimania@rediffmail.com

properties of the composites, the BB experimental design of RSM is used in this study. The experimental tests are performed based on the BB experimental design, and the data sets are recorded. Using these sets of experimental data obtained with experimental tests, mathematical models were then developed to show the effect of each process parameter and their interactions on mechanical properties of ASVFRVE composites. Predicted values were compared with experimental values to examine their agreement.

1 EXPERIMENTAL DETAILS

1.1 Materials

The ASV fibres for this study were procured from Fiber Shop, Tamilnadu, India. The chemical composition and physical properties of ASV fibres were measured at *SITRA*. The chemical composition and physical properties of ASV fibers were obtained by chemical and physical testing at *SITRA*. Table 1 shows the chemical composition and physical properties of ASV fibres.

Table 1. *Chemical composition and physical properties of ASV fibre*

Serial No.	Chemical compositions [%]		Physical properties	
1	Cellulose	69.3	Appearance	Yellowish
2	Hemi-cellulose	19.4	Diameter[mm]	0.67 to 2.4
3	Lignin	7.6	Density [g/cm^o]	1.38
4	Pectin	2.8	Tensile strength [MPa]	63.9 to 170.2
5	Wax	0.9	Modulus [MPa]	8.94 to 17.2

Vinyl ester (VE) resin with a clear yellow appearance, the styrene amount of 40 % to 50 %, a density of 1.145 g/cm³, viscosity of 400 mPa·s, and specific gravity of 1.09, was used as polymer matrices in this study and purchased from GVR Enterprises, India. Methyl Ethyl Ketone Peroxide (MEKP) ($C_8H_{18}O_6$), cobalt 6 % naphthenate (CoNap) ($C_{20}H_{34}CoO_4$) and N–N dimethyl aniline ($C_8H_{11}N$) were used as an accelerator, catalyst, and promoter, respectively.

1.2 Preparation of Composite Specimens

Composite specimens were fabricated with a hand lay-up method using the mould box (150 mm × 150 mm × 3 mm) developed in our laboratory. A mixture of vinyl ester (VE) resin, accelerator, catalyst, and the promoter was prepared with a ratio of 100:2.5:1.5:2 using a mechanical stirrer. ASV fibres were then added to this mixture at a calculated amount and stirred using a mechanical stirrer to ensure the perfect mixture. After pouring the mixture into the mould, the mould box was closed and allowed to cure at room temperature for 24 h. For each set of combinations, five specimens were fabricated and used for mechanical tests.

1.3 Testing of Composite Specimens

For tests, composites specimens were cut to the size of 150 mm × 20 mm × 3 mm using a wooden board cutter. Tensile tests were performed according to ASTM standard D 638-10 [9] procedure at a crosshead speed of 2 mm/min with a Fuel Instruments & Engineers, India (FIE) testing machine. The flexural strength of the composite was measured with the same machine using the 3-point bending fixture according to standard ASTM D-790-10 [10] with a crosshead speed of 2 mm/min. All tests were performed at room temperature. After the testing, the average mechanical property values were recorded and then used for modelling and analysis.

1.4 BB Experimental Design of RSM

In this study, a BB experimental design of RSM was used to divide the process parameters into three levels. Generally speaking, RSM is a collection of statistical and mathematical techniques that are useful for the modelling and analysing of engineering problems. The optimization of the response surface influenced by various process parameters is the main aim of this technique. They also quantify the relationship between the controllable input process parameters and the obtained response surface [11]. The process parameters are independent variables, which are assumed to be continuous and controllable by experiments with negligible errors. For the true functional relationship between independent variables, a suitable approximation is required.

To determine the optimal level, a second-order polynomial model can be used to correlate the relationship between independent variables and response surface, and is written in the matrix form as follows [8]:

$$\mathbf{Y} = b\mathbf{X} + \varepsilon, \tag{1}$$

where $\mathbf{Y}$ is a matrix of measured values, $\mathbf{X}$ is a matrix of independent variables, and b and ε are coefficients and errors, respectively. The value of b is calculated by solving Eq. (1) as follows [8]:

$$b = \left(\mathbf{X}'\mathbf{X}\right)^{-1}\mathbf{X}'\mathbf{Y}, \tag{2}$$

where $\mathbf{X}'$ is the transpose of the matrix $\mathbf{X}$ and $(\mathbf{X}'\mathbf{X})^{-1}$ is the inverse of the matrix $\mathbf{X}'\mathbf{X}$. Usually, a second-order model is utilized in RSM in the following form [8]:

$$Y = \beta_0 + \sum_{i=1}^{k} \beta_i x_i + \sum_{i=1}^{k} \beta_{ii} x_i^2 + \sum_{i=1}^{k-1} \sum_{j=2}^{k} \beta_{ij} x_i x_j + \varepsilon, \quad (3)$$

where Y *is* the response variable (dependent variable), x_i is the predictor variable (independent variable), β_0 is constant, β_{ii} (i = 1, 2, ..., k) and β_{ij} (i = 1, 2, ..., k; j = 1, 2, ..., k) are regression coefficients which are determined by the least square method, and ε is an error.

In this study, the BB experimental design of RSM was chosen for determining the relationship between the response variables (tensile strength, flexural strength and impact strength) and process parameters (fibre length, fibre content, and fibre diameters). A BB experimental design is a spherical, revolving design and has the advantage of requiring fewer experiments (15 trials) than a full factorial design would (27 trials). A BB design is a rotatable second-order design based on three-level incomplete factorial designs. It requires an experiment number according to [12]:

$$N = k_2 + k + c_p, \quad (4)$$

where k is the factor number and (c_p) is the replicate number of the central point [13].

According to the BB experimental design, the process parameters of the ASVFRVE composite were tested in a 15-run experiment to determine their optimal levels. The process parameters chosen for this study were designated as A_1, A_2, A_3 and prescribed into three levels, coded +1, 0, −1 for high, medium and low values, respectively. Table 2 shows the levels of the variable chosen for the BB experimental design. Three test parameters were coded according to the following equation [14]:

$$x_i = \frac{A_i - A_o}{\Delta A} \quad i = 1, 2, 3, \quad (5)$$

where x_i is the coded value of a process parameter (independent variable); A_i is the actual value of a process parameter (independent variable); A_o is the actual value of a process parameter (independent variable) at the center point; and ΔA is the step change value of a process parameter (independent variable). BB experimental design for the three parameters and three levels is shown in Table 3 with a total of 15 trials. The model for three parameters is of the following form [12]:

$$Y = \beta_0 + \beta_1 x_1 + \beta_2 x_2 + \beta_3 x_3 + \beta_{12} x_1 x_2 + \beta_{13} x_1 x_3 + \\ + \beta_{23} x_2 x_3 + \beta_{11} x_1^2 + \beta_{22} x_2^2 + \beta_{33} x_3^2, \quad (6)$$

where Y is the predicted response, β_0 is constant; x_1, x_2, and x_3 are process parameters (independent variables); β_1, β_2 and β_3 are linear coefficients; β_{12}, β_{13} and β_{23} are cross product coefficients and β_{11}, β_{22} and β_{33} are the quadratic coefficients [15]. The quality of the model was checked by an F-test and the determination coefficient R^2.

Table 2. *Levels of variable chosen for the BB experimental design*

Variables	Symbol		Coded variable level		
			Low	Medium	High
	Uncoded	Coded	-1	0	+1
Fiber length fly, [mm]	A_1	x_1	3	8	13
Fiber content f_c [wt%]	A_2	x_2	18.88	35.19	51.49
Fiber diameter f_d [mm]	A_3	x_3	0.24	0.85	1.45

Table 3. *BB experimental design with actual and coded values for mechanical properties of ASVFRVE composites and results*

Trials	Actual and coded level of variables			Experimental properties	
	x_1 f_l [mm]	x_2 f_c [wt%]	x_3 f_d [mm]	Tensile strength; σ_t [MPa]	Flexural strength; σ_f [MPa]
1	3 (–1)	18.88 (–1)	0.85 (0)	30.7	34.7
2	13 (+1)	18.88 (–1)	0.85 (0)	36.6	48.7
3	3(–1)	51.49 (+1)	0.85 (0)	33.5	34.2
4	13 (+1)	51.49 (+1)	0.85 (0)	36.3	43.7
5	3 (-1)	35.19 (0)	0.24 (–1)	35.8	40.8
6	13 (+1)	35.19 (0)	0.24 (–1)	41.3	52.3
7	3 (–1)	35.19 (0)	1.45 (+1)	33.9	36.2
8	13 (+1)	35.19 (0)	1.45 (+1)	38.8	51.3
9	8 (0)	18.88 (–1)	0.24 (–1)	34.2	40.5
10	8 (0)	51.49 (+1)	0.24 (–1)	36.9	39.3
11	8 (0)	18.88 (–1)	1.45 (+1)	31.1	39.6
12	8 (0)	51.49 (+1)	1.45 (+1)	33.1	38.1
13	8 (0)	35.19 (0)	0.85 (0)	37.8	46.9
14	8 (0)	35.19 (0)	0.85 (0)	37.8	46.9
15	8 (0)	35.19 (0)	0.85 (0)	37.8	46.9

2 RESULTS

A BB experimental design with three-parameters and three-coded levels, including three replicates at the centre point, was used to determine the response (mechanical properties of ASVFRVE composite). In 15 trials of the BB experimental designs, three centre point trials were added to provide a measure of process

stability and inherent variability. Fiber length f_l, fibre content f_c and fibre diameter f_d were the independent variables studied to predict the mechanical properties of ASVFRVE composite. Using the relationship between the process parameter mentioned in Table 2, the actual levels of the variables for each of the experiments in the design matrix were calculated, and the experimental results obtained as given in Table 3. From the experimental results listed in Table 3, the second-order response functions representing mechanical properties of the ASVFRVE composites can be expressed as a function of the process parameter. The relationship between the mechanical properties of the ASVFRVE composite and process parameters were obtained from the multiple regression analysis for coded unit as follows:

For the tensile strength model equation:

$$\sigma_t = 13.17 + 0.82x_1 + 1.09x_2 + 0.53x_3 - \\ -9.51\times10^3 x_1x_2 - 0.05x_1x_3 - 0.02x_2x_3 + \\ +2\times10^3 x_1^2 - 0.01x_2^2 - 1.09x_3^2. \quad (7)$$

For flexural strength model equation:

$$\sigma_f = 5.92 + 1.74x_1 + 1.69x_2 + 2.53x_3 - \\ -0.01x_1x_2 + 0.29x_1x_3 - 7.60\times10^3 x_2x_3 - \\ -0.02x_1^2 - 0.02x_2^2 - 3.69x_3^2. \quad (8)$$

The mechanical properties of the ASVFRVE composites at any regime in the interval of our experimental design could be calculated from Eqs. (7) and (8).

The analysis of variance (Table 4) for the tensile strength showed that this model was significant ($P<0.01$) with an F-value of 37.62. There is only a 0.05 % chance that a "Model F-value" this large could occur due to noise. The P-values were used as a tool to check the significance of each coefficient, which also indicates the interaction effects between each independent variable. The regression of all the linear term (x_1, x_2, and x_3) and quadratic coefficients of x_3^2 was significant; two cross-products (x_1, x_2) were also significant. Values greater than 0.1000 indicate the model terms are not significant. The fitness of the model was further confirmed by a satisfactory value of the determination coefficient, which was calculated to be 0.9854, indicating that 98.54 % of the variability in the response could be predicted by the model. The second order quadratic model for tensile strength was regressed by considering only the significant terms and shown as below:

$$\sigma_t = 13.17 + 0.82x_1 + 1.09x_2 + 0.53x_3 - \\ -9.51\times10^3 x_1x_2 - 1.09x_3^2. \quad (9)$$

The analysis of variance for the flexural strength was given in Table 5. The table reveals that the model for the flexural strength is significant ($P < 0.01$) with an F-value of 72.07.

There is only a 0.01 % chance that a "Model F-value" this large could occur due to noise. The P value (Prob > F) less than 0.05 indicates that the model terms are significant. In this case x_1, x_2, x_3, x_1x_2, x_2^2, and x_3^2 are significant model terms. An R^2 of 0.9924 indicates that the model developed explains 99.24 % of the variance in the dependent variable (flexural strength). The second-order quadratic model for flexural strength was regressed by considering only the significant terms and shown as:

Table 4. *ANOVA for response surface quadratic model for optimization of tensile strength of ASVFRVE composites*

Source	Sum of squares	Degree of freedom	Mean square	F-value	p-value Prob>F
Model	118.32	9	13.15	37.62	0.0005
A-Length	45.6	1	45.6	130.48	<0.0001
B-Content	6.48	1	6.48	18.54	0.0077
C-Diameter	15.96	1	15.96	45.67	0.0011
AB	2.4	1	2.4	6.87	0.047
AC	0.09	1	0.09	0.26	0.6334
BC	0.12	1	0.12	0.35	0.5796
A^2	9.231E-003	1	9.231E-003	0.026	0.8773
B^2	47.19	1	47.19	135.02	< 0.0001
C^2	0.59	1	0.59	1.69	0.2503
Residual	1.75	5	0.35	-	-
Lack of fit	1.75	3	0.58	-	-
Pure Error	0	2	0	-	-
Cor Total	120.07	14	-	-	-

$$\sigma_f = 5.92 + 1.74x_1 + 1.69x_2 + 2.53x_3 - \\ -0.01x_1x_2 - 0.02x_2^2 - 3.69x_3^2. \quad (10)$$

3 DISCUSSION

The experimental and predicted values of the mechanical properties of the ASVFRVE composites are given in Table 6.

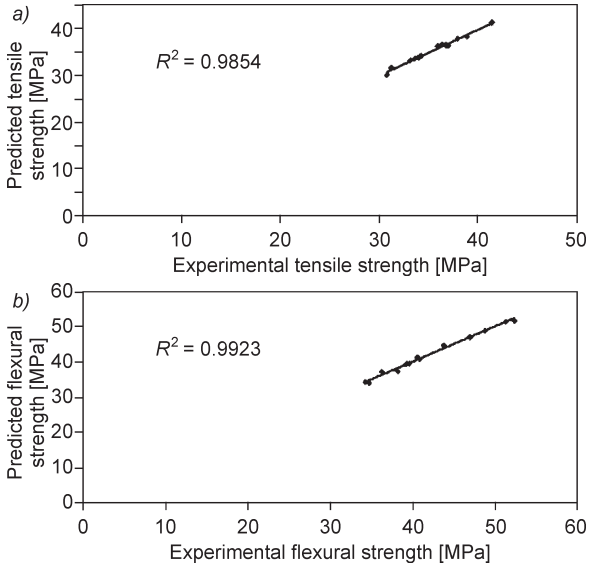

Fig. 1. *Relation between experimental and predicted values of a) tensile strength, and b) flexural strength*

Table 5. *ANOVA for response surface quadratic model for optimization of flexural strength of ASVFRVE composites*

Source	Sum of squares	Degree of freedom	Mean square	*F*-value	*p*-value Prob > *F*
Model	481.6	9	53.51	72.07	<0.0001
A-length	313.75	1	313.75	422.56	<0.0001
B- content	8.41	1	8.41	11.32	0.02
C-diameter	7.41	1	7.41	9.98	0.0251
AB	5.06	1	5.06	6.82	0.0476
AC	3.24	1	3.24	4.36	0.091
BC	0.022	1	0.022	0.03	0.8686
A^2	0.59	1	0.59	0.8	0.4133
B^2	140.79	1	140.9	189.62	<0.0001
C^2	6.73	1	6.73	9.06	0.0297
Residual	3.71	5	0.74	-	-
Lack of Fit	3.71	3	1.24	-	-
Pure Error	0	2	0	-	-
Cor Total	485.31	14	-	-	-

The actual and predicted values of the tensile and flexural strength obtained using model equations (Eqs. (7) and (8)) are presented in Fig. 1. The predicted values are in good agreement with the experimental data values, indicating a good fitness (R^2 value of 0.985 for tensile strength, R^2 value of 0.992 for flexural strength).

Table 6. *Experimental and predicted values of tensile strength and flexural strength of ASVFRVE composites*

Trial	Tensile strength [MPa]		Flexural strength [MPa]	
	Experimental	Predicted	Experimental	Predicted
1	30.7	30.21	34.7	33.96
2	36.6	36.54	48.7	48.74
3	33.5	33.56	34.2	34.16
4	36.3	36.79	43.7	44.44
5	35.8	36.33	40.8	40.75
6	41.3	41.60	52.3	51.48
7	33.9	33.80	36.2	37.03
8	38.8	38.28	51.3	51.35
9	34.2	34.16	40.5	41.29
10	36.9	36.31	39.3	39.39
11	31.1	31.69	39.6	39.51
12	33.1	33.14	38.1	37.31
13	37.8	37.80	46.9	46.90
14	37.8	37.80	46.9	46.90
15	37.8	37.80	46.9	46.90

3.1 Validation of Models

To validate the developed model, ten additional experiments were carried out using random conditions as given in Table 7; the statistical results calculated by the developed model were compared with the experimental results. The relative deviation (RD) was calculated with the following equation:

$$\text{RD} = \frac{\text{Predicted value - Actual value}}{\text{Actual value}} \times 100,$$

The results show the low relative deviation; therefore, this developed model could be used to describe the important process parameters that affect the mechanical properties of ASVFRVE composites.

3.2 Effect of Process Parameters on Mechanical Properties

In order to gain a better understanding of the results, the 3D response surface plots of predicted models are presented in Fig. 2. It is evident from the results that all the input process parameters have a significant effect on the tensile strength of the ASVFRVE composite. Fig. 2a shows the effect of fibre content and fibre length on the tensile strength of the ASVFRVE composite. When the fibre length, fibre loading and fibre diameter was 3 mm, 18.88 wt%, and 0.85

Table 7. *Process parameters and their corresponding experimental and predicted strength values with relative error percentage for validation*

Trials	Process parameters			Tensile strength [MPa]			Flexural strength [MPa]		
	f_l	f_c	f_d	Experimental	Predicted	R [%]	Experimental	Predicted	R [%]
1	4	19.34	1.4	30.13	30.87	2.46	34.11	34.72	1.78
2	7	39.56	0.65	41.94	42.99	2.50	50.89	51.12	0.45
3	11	48.24	1.2	43.71	43.94	0.54	52.96	53.43	0.88
4	5	28.11	0.93	37.46	37.52	0.15	45.44	44.73	1.57
5	9	41.82	0.33	43.84	44.86	2.32	52.51	53.08	1.09
6	12	25.74	0.78	39.98	40.67	1.73	52.65	53.37	1.37
7	6	33.47	1.3	40.19	39.12	2.67	47.33	46.78	1.17
8	8	44.65	0.33	43.97	44.59	1.42	50.88	51.88	1.96
9	10	30.88	0.84	40.79	41.49	1.73	52.87	53.11	0.45
10	5	22.67	1.1	34.62	34.30	0.91	39.92	40.74	2.06

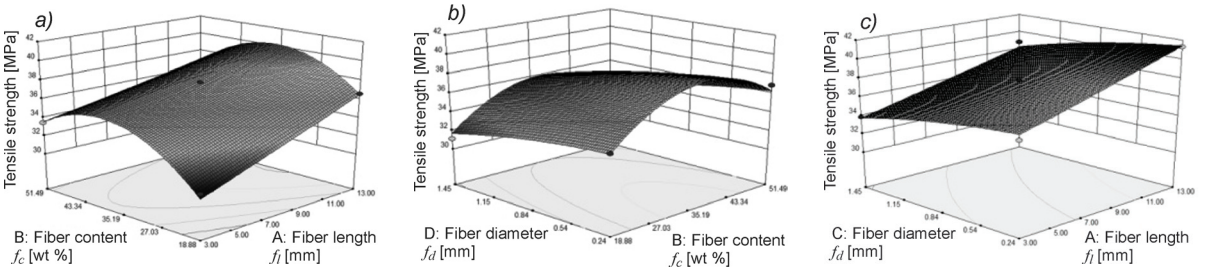

Fig. 2. *3D response surface plots showing a) the effect of fiber length (x_1) and fiber content (x_2), b) the effect of fiber content (x_2) and fiber diameter (x_3), and c) the effect of fiber length (x_1) and fiber diameter (x_3) on the tensile strength of ASVFRVE composites*

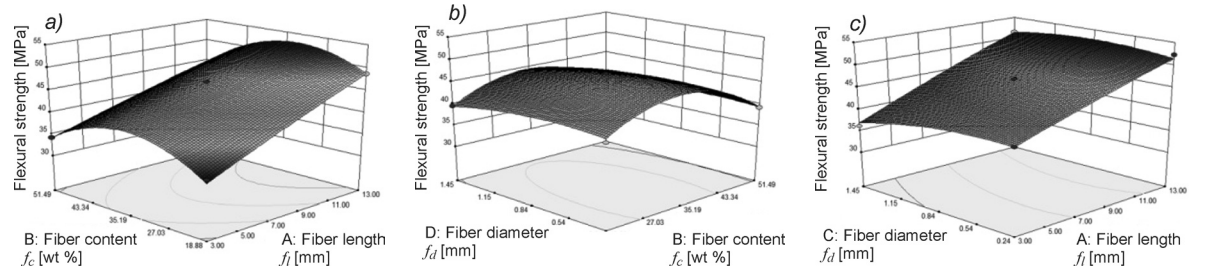

Fig. 3. *3D response surface plots showing (a) the effect of fiber length (x_1) and fiber content (x_2), (b) the effect of fiber content (x_2) and fiber diameter (x_3), and (c) the effect of fiber length (x_1) and fiber diameter (x_3) on the flexural strength of ASVFRVE composites*

mm, the tensile strength of the composites became minimal. Fig. 2b shows the effect of fibre diameter and fibre content on the tensile strength, and Fig. 2c shows the effect of fibre diameter and fibre length on the tensile strength. The maximum tensile strength value was observed in the composite having a fiber content of 35.19 wt%, fiber diameter of 0.24 mm, and a fiber length of 13 mm respectively. Thus, the interaction between the fibre length and fibre loading strongly affected the tensile strength in the composite specimen.

Fig. 3 show the 3D response surface plot for flexural strength. Fig. 3a shows the effect of fibre length and fibre content on the flexural strength. This 3D response graph suggests that as the fibre length increases the flexural strength of composite increases. The flexural strength was also influenced by the fiber content. The flexural strength is found to be greater when the fibre length and fibre content was 13 mm and 35.19 wt% in the ASVFRVE composites. It is observed that the fibre length and fibre content are essential to increase the flexural strength. Fig. 3b shows the effect of fibre diameter and fibre content on the flexural strength and Fig. 3c shows the effect of fibre diameter and fibre length on the flexural strength. The maximum flexural strength values were observed when the fibre diameter is at 0.24 mm when compared to 0.85 mm and 1.45 mm. It was also observed that

the maximum flexural strength value was identified at low fibre content and high fibre length.

3.3 Optimization of Process Parameters and the Response

After studying the effect of the process parameters on the mechanical properties of ASVFRVE composite, the levels of these parameters that give the optimal mechanical properties were determined. It is evident from the second-order quadratic equations (Eqs. (7) and (8)) and 3D response plots (Figs. 2 and 3) that the fiber length (x_1) in level 3, fiber content (x_2) in level 2, and fiber diameter (x_3) in level 1 increases both the tensile strength and the flexural strength of the ASVFRVE composite. This level of fibre length may be higher than the critical fibre length. The most effective fibre reinforcement is achieved if the length of the fibre exceeds the critical fibre length, which is also depending on the diameter of the fibre [16].

The fibre content (35.19 wt%) was identified as the optimal fibre content to obtain the better mechanical properties of ASVFRVE composites and above which the properties of the composite may drop. This level of fibre content is higher than critical fibre content. To be suitable for reinforcement material the fiber materials must increase the tensile strength and modulus of elasticity of the matrix and meet the following conditions: the fibers must exceed critical fiber content; the strength and rigidity of fibers itself must exceed the strength and rigidity of the matrix alone; there must be optimal bonding between the fibers and matrix. In the fibre reinforced polymer composites, composite strength also depends on fibre diameter. The smallest fibre diameter could achieve higher mechanical properties due to its larger specific contact surface with the matrix. In this study, the maximum tensile and flexural strength values were observed in the composite having a fiber diameter of 0.24 mm (x_3) at level 1. The strength values were decreased with increasing fibre diameter to level 2 (0.85 mm) and level 3 (1.45 mm).

Thus, level 3 of fibre length (x_1), level 2 of fibre content (x_2), and level 1 of fibre diameter (x_3) were selected as the optimal levels of process parameters. For confirmation, five fresh experimental tests were carried out at the optimal levels of the process parameters and the results obtained are given in Table 8, which summarizes the process parameters, the average of the experimental strength value, the predicted strength value and the percentages of error. The confirmation result shows that the prediction models developed through the BB design of the RSM are quite accurate as the percentage of error in the prediction was in good agreement.

The effectiveness of the BB design of RSM is also proved by several authors in natural fibres and their polymer composites [17] and [18].

Table 8. *Confirmation test results*

Fiber length [mm]	Fiber content [wt%]	Fiber diameter [mm]	Variable	Tensile strength [MPa]	Flexural strength [MPa]
13	35.19	0.24	Average	41.7	52.1
			Predicted	41.4	51.5
			Error [%]	-0.7194	-1.1516

4 CONCLUSION

A three-level BB design of response surface methodology was employed in this paper to optimize the fabrication process parameters for mechanical properties of ASVFRVE composites. The process parameters selected for this work were fibre length, fibre content, and fibre diameter. The experimental strength values were fitted with the predicted strength values by a second-order polynomial equation by a multiple regression analysis and more than 98.54% of the variation in the tensile strength and 99.24% of the variation in the flexural strength could be predicted with the developed models. The validation results revealed that there was good agreement between the predicted and experimental values. The optimal fabrication process parameters for the tensile and flexural strength of ASVFRVE composites were determined using the response surface graph and models. Level 3 of fibre length (13 mm), level 2 of fibre content (35.19 wt %), and level 1 of fibre diameter (0.24 mm) were selected as the optimal level of fabrication process parameters. Additionally, five fresh, experimental tests were carried out at the optimal levels of the process parameters for the confirmatory study. Under the optimal conditions, the corresponding response value predicted for the tensile and the flexural strength were 41.7 MPa and 52.1 MPa, respectively. The present paper has proved that the BB design of response surface methodology could efficiently be applied for the modelling and optimization of the mechanical properties of natural fibre polymer composites. It is also an economical way of obtaining the maximum amount of information in a short time duration and with a reduced number of experiments.

5 NOMENCLATURE

SITRA	South India Textile Research Association, India
ANOVA	Analysis of variance
f_l	Fiber length [mm]
f_c	Fiber content [wt%]
f_d	Fiber diameter [mm]
R	Relative error percentage [%]

6 REFERENCES

[1] Chen, H., Miao, M., Ding, X. (2009). Influence of moisture absorption on the interfacial strength of bamboo/vinyl ester composites. *Composites Part A: Applied Science and Manufacturing*, vol. 40, no. 12, p. 2013-2019, **DOI:10.1016/j.compositesa.2009.09.003**.

[2] Laftah, W.A, Hashim, S. (2014). The influence of plant natural fibers on swelling behavior of polymer hydrogels. *Journal of Composite Materials*, vol. 48, no. 5, p. 555-569, **DOI:10.1177/0021998313476323**.

[3] Jeencham, R., Suppakarn, N., Jarukumjorn, K., (2014). Effect of flame retardants on flame retardant, mechanical, and thermal properties of sisal fiber/polypropylene composites. *Composites Part B: Engineering*, vol. 56, p. 249-253, **DOI:10.1016/j.compositesb.2013.08.012**.

[4] Wongsorat, W., Suppakarn, N., Jarukumjorn, K. (2014). Effects of compatibilizer type and fiber loading on mechanical properties and cure characteristics of sisal fiber/natural rubber composites. *Journal of Composite Materials*, vol. 48, no. 19, p. 2401-2411, **DOI:10.1177/0021998313498790**.

[5] Misra, S., Misra, M., Tripathy, S.S., Nayak, S.K., Mohanty, A.K. (2002). The influence of chemical surface modification on the performance of sisal polyester biocomposites. *Polymer Composites*, vol. 23, no. 2, p. 164-170, **DOI:10.1002/pc.10422**.

[6] Joseph, P.V., Joseph, K., Thomas, S., Pillai, C.K.S., Prasad, V.S., Groeninckx, G., Sarkissova, M. (2003). The thermal and crystallization studies of short sisal fiber reinforced polypropylene composites. *Composites Part A: Applied Science and Manufacturing*, vol. 34, p. 253-266, **DOI:10.1016/S1359-835X(02)00185-9**.

[7] Maran, J.P., Sivakumar, V., Thirugnanasambandham, K., Sridhar, R. (2013). Response surface modeling and analysis of barrier and optical properties of maize starch edible films. *International Journal of Biological Macromolecules*, vol. 60, p. 412-421, **DOI:10.1016/j.ijbiomac.2013.06.029**.

[8] Manohar, M., Joseph, J., Selvaraj, T., Sivakumar, D. (2013). Application of Box Behnken design to optimize the parameters for turning Inconel 718 using coated carbide tools. *International Journal of Scientific & Engineering Research*, vol. 4, no. 4, p. 620-644, **DOI:10.14299/000000**.

[9] ASTM D 638-10. (2010). Standard test method for tensile properties of plastics. *Annual Book of ASTM Standards*, vol. 08.01, p. 1-16, ASTM International, West Conshohocken

[10] ASTM D 790–10. (2010). Standard test methods for flexural properties of un-reinforced and reinforced plastics and electrical insulating materials. *Annual Book of ASTM Standards*, vol. 08.01, p. 1-11, ASTM International, West Conshohocken.

[11] Kwak, J.-S. (2005). Application of Taguchi and response surface methodologies for geometric error in surface grinding process. *International Journal of Machine Tools and Manufacture*, vol. 45, no. 3, p. 327-334, **DOI:10.1016/j.ijmachtools.2004.08.007**.

[12] Khajvand, T., Chaichi, M.J., Nazari, O.L., Golchoubian, H. (2011). Application of Box–Behnken design in the optimization of catalytic behavior of a new mixed chelate of copper (II) complex in chemiluminescence reaction of luminol. *Journal of Luminescence*, vol. 131, no. 5, p. 838-842, **DOI:10.1016/j.jlumin.2010.11.015**.

[13] Souza, A.S., dos Santos W.N.L., Ferreira S.L.C. (2005). Application of Box–Behnken design in the optimization of an on-line pre-concentration system using knotted reactor for cadmium determination by flame atomic absorption spectrometry. *Spectrochimica Acta Part B: Atomic Spectroscopy*, vol. 60, no. 5 p. 737–742, **DOI:10.1016/j.sab.2005.02.007**.

[14] Dong, C.-H., Xie, X.-Q., Wang, X.-L., Zhan, Y., Yao, Y.-J. (2009). Application of Box-Behnken design in optimization for polysaccharides extraction from cultured mycelium of Cordyceps sinensis. *Food and Bioproducts Processing*, vol. 87, no. 2, p. 139-144, **DOI:10.1016/j.fbp.2008.06.004**.

[15] Montgomery, C.D. (2001). *Design and Analysis of Experiments*. John Wiley and Sons, Singapore.

[16] Callister, Jr., W.D. (2003). *Materials Science and Engineering—An Introduction, Composites*. John Wiley & Sons, Hobocken.

[17] Toupe, J.L., Trokourey, A., Rodrigue, D. (2014). Simultaneous optimization of the mechanical properties of postconsumer natural fiber/plastic composites: Phase compatibilization and quality/cost ratio. *Polymer Composites*, vol. 35, no. 4, p. 730-746, **DOI:10.1002/pc.22716**.

[18] Aly, M., Hashmi, M.S.J., Olabi, A.G., Benyounis, K.Y., Messeiry, M., Hussain, A.I., Abadir, E.F. (2012). Optimization of alkaline treatment conditions of flax fiber using Box–Behnken method. *Journal of Natural Fibers*, vol. 9, no. 4, p. 256-276, **DOI:10.1080/15440478.2012.738036**.

Strojniški vestnik - Journal of Mechanical Engineering 62(2016)5, 281-290
DOI:10.5545/sv-jme.2015.3079
Original Scientific Paper
Received for review: 2015-09-29
Received revised form: 2016-03-08
Accepted for publication: 2016-03-21

Adaptive Empirical Mode Decomposition for Bearing Fault Detection

Van Tuan Do* – Le Cuong Nguyen
Electric Power University, Department of Electronics and Telecommunication, Vietnam

Many techniques for bearing fault detection have been proposed. Two of the most effective approaches are using envelope analysis and the empirical mode decomposition method (EMD), also known as Hilbert-Huang transform (HHT), for vibration signals. Both approaches can detect the bearing fault when the vibration data are not strongly disturbed by noise. In the approach using EMD method, the EMD algorithm is used to decompose the vibration data into components with a well-defined instantaneous frequency called intrinsic mode functions (IMFs). Then a spectral analysis is used for selected IMFs to indicate the appearance of nominal bearing defect frequencies (nominal frequencies), which are caused by bearing faults. However, when the data are strongly disturbed by noise and other sources, the approach can be failed. The EMD algorithm generates IMFs itself; hence, the IMFs will also contain both a fault signal part and other components. It becomes more severe when the other components are dominant and have significant amplitudes near the same frequencies as the fault signal part. Moreover, in the IMF extracting process, the EMD methods keeps removing the low-frequency components until the residual is an IMF; therefore, until the IMF is found, some of the fault signal parts can be removed and will appear in the next IMFs. Therefore, it must be emphasized that the energy of the fault signal part can spread in some IMFs that will lead the detecting faulty features in any of those IMFs to be weak. In this paper, we address the weakness of the EMD method for bearing fault detection by introducing an adaptive EMD (AEMD). The AEMD algorithm is intended to generate IMFs so that one of them contains most of the energy of the fault signal part; thus, it assists our model to detect the bearing fault better. Moreover, the bearing fault detection model using the AEMD method with simulation data is compared with those of using envelope analysis and the latest version of the EMD, called an ensemble EMD algorithm. An application study of bearing fault detection with AEMD method is also carried out.

Keywords: bearing fault detection, Hilbert-Huang transforms, empirical mode decomposition, intrinsic mode function, envelope analysis, nominal frequency

Highlights

- *Bearing faults in the low-speed bearing system are hard to detect with the original EMD algorithm as well as the envelope analysis.*
- *By considering the energy of the IMF, the proposed adaptive EMD algorithm works well in bearing fault detection and performs better than the original EMD algorithm.*

0 INTRODUCTION

There have been a huge number of studies on rotating machine fault detection, especially for bearings, which are main components of the inner ring, outer ring, bearings (rolling elements) and cage. There are a number of mechanisms leading to bearing failures such as fatigue damage, wear damage, plastic deformation, corrosion, mechanical damage, and lubrication deficiency [1] to [3]. The most common faults on bearing components are fatigue damage including wear, pitting, and spalling. Such damage is a fatigue phenomenon that occurs when a fatigue crack initiates at the surface of bearing's components or at a small depth below the surface. The crack usually propagates for a short distance in a direction roughly parallel to the surface before turning or branching to the surface. As cracks progress further into the surface, the rate of propagation increases. When the cracks have grown to the extent that they separate a piece of the surface material, a pit is formed. The material is torn away from the damaged area by the relative motion of the contacting part. A loss of material that reaches some level is frequently termed spalling [4].

When fatigue damage occurs on a bearing's component and this defective component is in contact with another component at the damage point, an impulsive force is incurred that causes the bearing to vibrate. The vibration signal obtained from the bearing consists of an impulse whenever a rolling element passes over the damage point, which can be in the outer race, inner race, or the surfaces of rolling elements or cage. The pulse appearance frequencies are dependent on the damage point locations and are called nominal bearing defect frequencies (or, more briefly nominal frequency) (or characteristic defect frequency (CDF) as called in [5]). The nominal frequencies corresponding to bearing components are calculated by Eqs. (1) to (4). The vibration signal from each pulse presents the ringing of the bearing at its resonance frequency, also called ringing pulse frequency. The pulse occurs with high amplitude

*Corr. Author's Address: Electric Power University, Department of Electronics and Telecommunication, 235 Hoang Quoc Viet, Hanoi, Vietnam, tuandv@epu.edu.vn

and then the amplitude attenuates rapidly. This will cause the appearance of ringing pulse frequency and its sidebands in the vibration data. The sidebands are results of the modulation between the ringing pulse frequency and nominal frequency.

Ball pass frequency outer race (BPFO):

$$f_{outer} = \frac{N_b}{2}\left(1 - \frac{B_d}{P_d}\cos\theta\right)\frac{RPM}{60}, \quad (1)$$

ball pass frequency inner race (BPFI):

$$f_{inner} = \frac{N_b}{2}\left(1 + \frac{B_d}{P_d}\cos\theta\right)\frac{RPM}{60}, \quad (2)$$

rolling elements' frequency (BSF):

$$f_{roller} = \frac{P_d}{2B_d}\left(1 - \left(\frac{B_d}{P_d}\cos\theta\right)^2\right)\frac{RPM}{60}, \quad (3)$$

cage or train frequency (FTF):

$$f_{train} = \frac{1}{2}\left(1 - \frac{B_d}{P_d}\cos\theta\right)\frac{RPM}{60}, \quad (4)$$

where RPM is the shaft rotation speed, N_b is the number of the balls or rollers, B_d is the ball or roller diameter, P_d is the bearing pitch diameter and θ is the contact angle.

The bearing fault detection problems are generally concerned with algorithms and models in order to detect increased vibration amplitudes at the nominal frequencies. The envelope analysis is a well-known and easy method for bearing fault detection and reported in various research, such as in **[1]**. This paragraph concentrates on the state-of-the-art techniques that use the EMD method for fault detection of rotating machines, especially for bearings. In **[5]** and **[6]**, the authors suggested using an empirical mode decomposition (EMD) method **[7]** for bearing fault detection. The EMD algorithm was used to decompose the vibration signal into intrinsic mode functions (IMFs). The authors used a fast Fourier transform (FFT) amplitude spectrum for each IMF and found that the defect frequency (nominal frequency) appeared in the FFT spectrum of the first IMF. In general, when the vibration data are weakly disturbed, the method will work well. However, if the data are influenced by noise or other frequency components, the method can fail to perform adequately. For example, the fault signal part can be influenced by other rotating frequencies, sensor noise, and sensor resonant frequencies, which will be demonstrated in the later sections of this paper.

Since **[5]** and **[6]** were reported, several proposed methods utilizing the EMD algorithm have been for bearings and other rotating machines. In **[8]**, the authors proposed a diagnosis method based on artificial neural networks (ANN). The entropy of each IMF was estimated to determine which IMF signal should be selected for the training process of the ANN network. The classification method using ANN was established to classify different bearing conditions: normal, outer race and inner race faults. In **[9]**, the authors showed that instead of using entropy energy, which was not useful for non-stationary vibration signals, they introduced a new feature called IMF energy moment. They used the wavelet package decomposition (WPD) to de-noise the vibration data and then calculated each IMF energy component. The IMF containing the highest IMF energy component will be selected to extract faulty features mostly related to defect frequencies such as 1X, 2X, and its harmonics. The features were then served as inputs to a back propagation network. The network was employed as a classification model for machine fault diagnosis. In **[10]**, the authors utilized the EMD algorithm to decompose vibration data from defect roller bearings into IMFs. The autogressive models (AR) were established for each IMF to extract AR parameters and residual variations, which were then aggregated into one feature vector. A proposed diagnosis model with the Mahalanobis distance of feature vectors was used to recognize bearing faults in three conditions: normal, outer race and inner race damage. The authors in **[11]** explained that using the IMFs alone for rotating machine fault detection could not work well with noisy vibration data. They combined some of the consecutive IMFs into one and called it a combined mode functions (CMD) and utilized it for the fault detection of generators. If there was a sudden change in the waveform of the next IMF, then the CMDs was suggested be used more than the original IMFs. Recently, an approach called ensemble EMD (EEMD) **[12]** was proposed to solve the mode mixing problem that happens in the original EMD method by adding white noise to the IMFs during the decomposition process of the original EMD. The authors in **[13]** showed that it was not necessary to add white noise to all the decomposition modes since the low-frequency part will be affected by noise, worsening the EMD process. It also brings a higher computational complexity to the algorithm. Therefore, they simply suggested using band-limited noise instead of white noise into the signal to be decomposed. Other than proposed research with EMD for bearing fault detection, there are also several

approaches, such as in [14] to [16]. In [14] the authors converted one dimension of the vibration signal into a two-dimension domain, and then a recognition model is applied for fault classification including bearing faults. In [15], a Meyer-Wavelet-Packets algorithm was used to detect the bearing faults and the author stated that the proposed approach provided better results than that of using coif4 wavelet. In [16], the discrete wavelet transforms and an adaptive resonance theory neural network were used to detect the gear crack. This method can be applied for bearing faults as well.

Some adaptive techniques using Morelet wavelets were successfully proposed for rotating machine component fault detection, such as [17] and [18]. In this paper; an adaptive EMD is proposed; however, two major topics are addressed: (i) improving of the original EMD algorithm in order to enhance the appearance of the nominal frequencies, and (ii) proposing a model for both simulation and experiment data for bearing fault detection. The EMD algorithm will be modified so that the output IMFs will only be adapted for the purpose of bearing fault detection. The method is called adaptive EMD (AEMD). The AEMD is used especially for addressing the weaknesses of the original EMD method proposed in [5] and [6] when data are strongly disturbed by other components and noise. The AEMD method is intended to be better than original EMD in term of showing the nominal defect frequency for bearing fault detection only. Please note that if the data is so clean in term of no influences to the ringing pulse frequency band, then the original and adaptive EMD will work equally well.

The rest of the paper is organized as follows. The EMD and ensemble EMD algorithms will be presented in Section 2. Section 3 is about the proposed adaptive EMD algorithm. The bearing analysis comparison with simulation data will be presented in Section 4, while a bearing fault detection application study with adaptive EMD is discussed in Section 5. The conclusion is follows in Section 6.

1 EMD AND ENSEMBLE EMD ALGORITHMS

1.1 Empirical Mode Decomposition

The empirical mode decomposition method is a signal processing technique proposed for extracting all the oscillatory modes embedded in a signal without any requirement of stationarity or linearity of the data. The

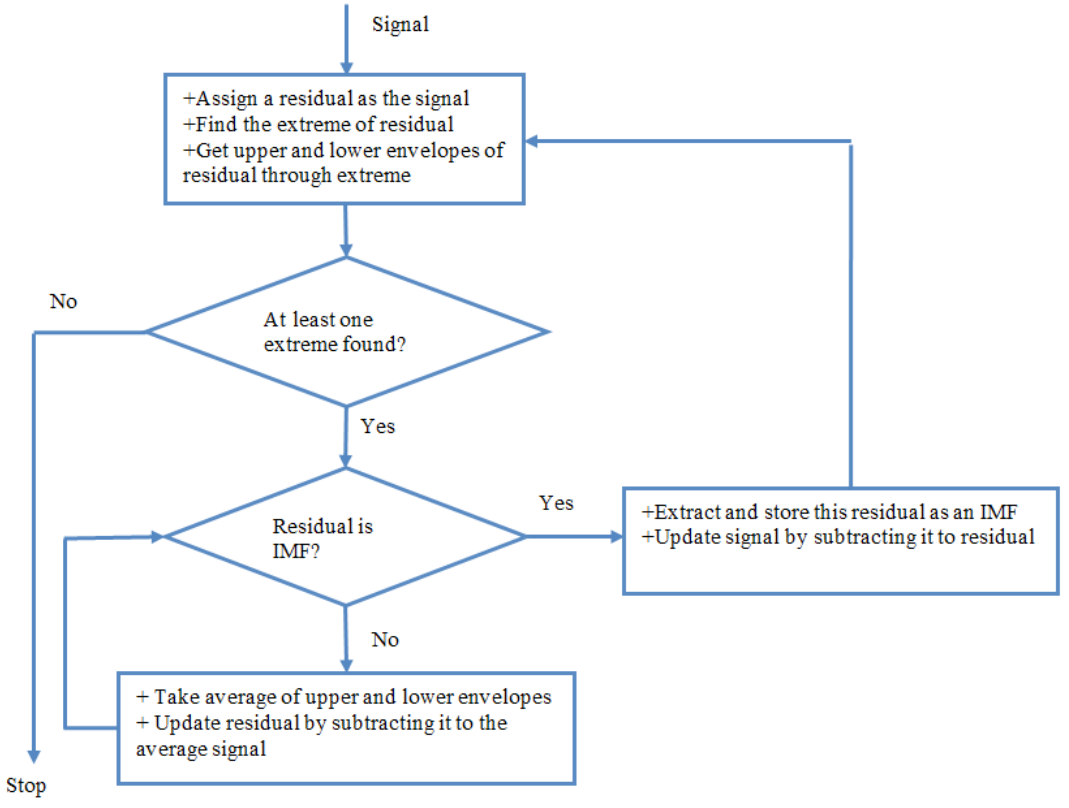

Fig. 1. *Flow chart of the original EMD algorithm*

goal of this procedure is to decompose a time series into components with well-defined instantaneous frequencies by empirically identifying the physical time scales intrinsic to the data, which is the time lapse between successive extrema. Each characteristic oscillatory mode extracted, named IMF, has only one extreme (minima or maxima) between zero crossings and the mean value between the upper and lower envelope, which are established based on the extreme, is equal to zero. Therefore, in the algorithm, conditions for a signal to be an IMF are as follows:

- Differences in the number of maxima and zero-crossings must not be more than 1.
- The mean of the average of upper and lower envelopes should be smaller than a defined threshold, which is close to zero.

The detailed algorithm can be found in [7]. The algorithm flowchart is presented in Fig. 1. The outcomes of the EMD algorithm will be several IMFs. The number of the IMFs may be different depending on the signal analysed. Among the IMFs extracted, some of them contain a fault signal part that will help identify the faults. The extracted features can be used individually or as inputs to fault diagnosis models. The bearing fault diagnosis methods using the EMD method so far deal with three problems: (i) finding the relevant IMFs; (ii) extracting relevant features, possibly related to faults from those IMFs; (iii) establishing fault detection and diagnosis models utilizing the features.

1.2 Ensemble Empirical Mode Decomposition

The EEMD is an improvement on the EMD algorithm targeting to remove mixing mode problems [12]. Comparing to the EMD method, the improvement of the ensemble EMD is described as follows:

- Add a white noise series to the targeted data.
- Decompose the data noise into IMFs with added white.
- Repeat step 1 and step 2 multiple times, but with different white noise series each time.
- Obtain the (ensemble) means of corresponding IMFs of the decompositions as the final result.

2 ADAPTIVE EMPIRICAL MODE DECOMPOSITION

As previously discussed, the envelope analysis is easy to implement and a method of choice for bearing analysis if a suitable band pass filter is available. However, for implementation on an automation system or embedded system, the EMD method is preferred. The indication of the nominal frequency appearance fails with the EMD method when the data are strongly disturbed, which will be indicated in the analysis result section. Looking into the decomposition process of the original EMD algorithm, the EMD method extracts the IMF with the highest frequencies first, followed by the lower frequencies. In other words, the first IMF will contain the highest frequency components, and the last one will contain the lowest frequency components. To extract an IMF, the algorithm keeps removing low-frequency components until the residual (signal after removing low-frequency components) is an IMF. The reasons the EMD method failed in the previous example can be explained as follows:

- The signal part caused by faults can easily share the energy among some IMFs if it has a high-frequency bandwidth that will lead to detecting the fault features in any of those IMFs to be weak.
- When data is complicated, it is easy for the algorithm to extract IMFs, including the other components that interfere with the fault signal part.

In the AEMD, we supplement the decomposition process of the EMD algorithm to avoid the first reason. On the process of removing low-frequency components in the EMD algorithm, the AEMD algorithm keeps calculating the energy of frequency components of the residual concentrating on the frequency segment that contains the nominal frequency and its harmonics. The energy is called "peak energy", determining whether the low frequencies are related to faults or not. The IMF will be assigned as the residual at the point that the peak energy of the residual has the highest value. If the low-frequency components are related to faults, then they will be retained in the extracted IMF. Otherwise, they will be removed and will appear in the next IMFs. The peak energy value in this paper is calculated as the total power spectrum density at the nominal frequency and its first two harmonics. Other energy indicators can be considered to replace power spectrum density, such as the amplitude of nominal frequency and its first harmonics, the power spectrum of the nominal frequency and its first two harmonics, etc. [19]. The details of the AEMD algorithm can be seen in Fig. 2.

The goal of a bearing fault detection model based on a vibration signal is to identify the fault symptom that is embedded into the vibration signal; here, it is the nominal frequency. Our proposed model using the proposed AEMD method is as follows:

- Use the AEMD algorithm for the vibration data to extract IMFs signals.

- Choose the best IMF.
- Calculate the power spectrum of the envelope signal of this IMF.
- Estimate the amplitude of nominal frequency in the plots of the power spectrum.

3 BEARING ANALYSIS DECOMPOSITION

3.1 Simulation Data

In this section, we simulate the vibration data for a normal bearing and for a bearing with fatigue damage on its outer race. Whenever a rolling element goes over the damage point on the surface of the outer race, there will be a ringing pulse appearing in the bearing vibration data. The vibration data measured from the bearing will be covered by high-level imbalance and misalignment components, random vibrations accompanied by friction and other sources such as environment noise, sensor noise, and sensor resonance signals. The following frequency components are dominant in the vibration data measured by accelerometers on the surfaces of bearings: (i) shaft frequency, which is 1X frequency component, caused by rotor rotation; (ii) imbalance vibration (1X), its harmonics (2X, 3X, 4X), and its sidebands caused by misalignment components; (iii) other rotating components, such as gear-mesh frequency, sidebands, and gear rotating frequencies. Simulations of vibration data from bearings are well explained in [3] and [20].

The simulated vibration signal, $x(t)$, is generated as follows:

$$x(t) = a(t) + n(t) + r(t), \tag{5}$$

where $a(t)$ are approximation signals, $n(t)$ is Gaussian noise and $r(t)$ are ringing pulse signals. More explanation can be found in [20]. In this paper, the vibration data for outer race defect bearings are simulated as explained in Eq. (5) and without ringing pulse part, $t(t)$ for a normal bearing. The nominal

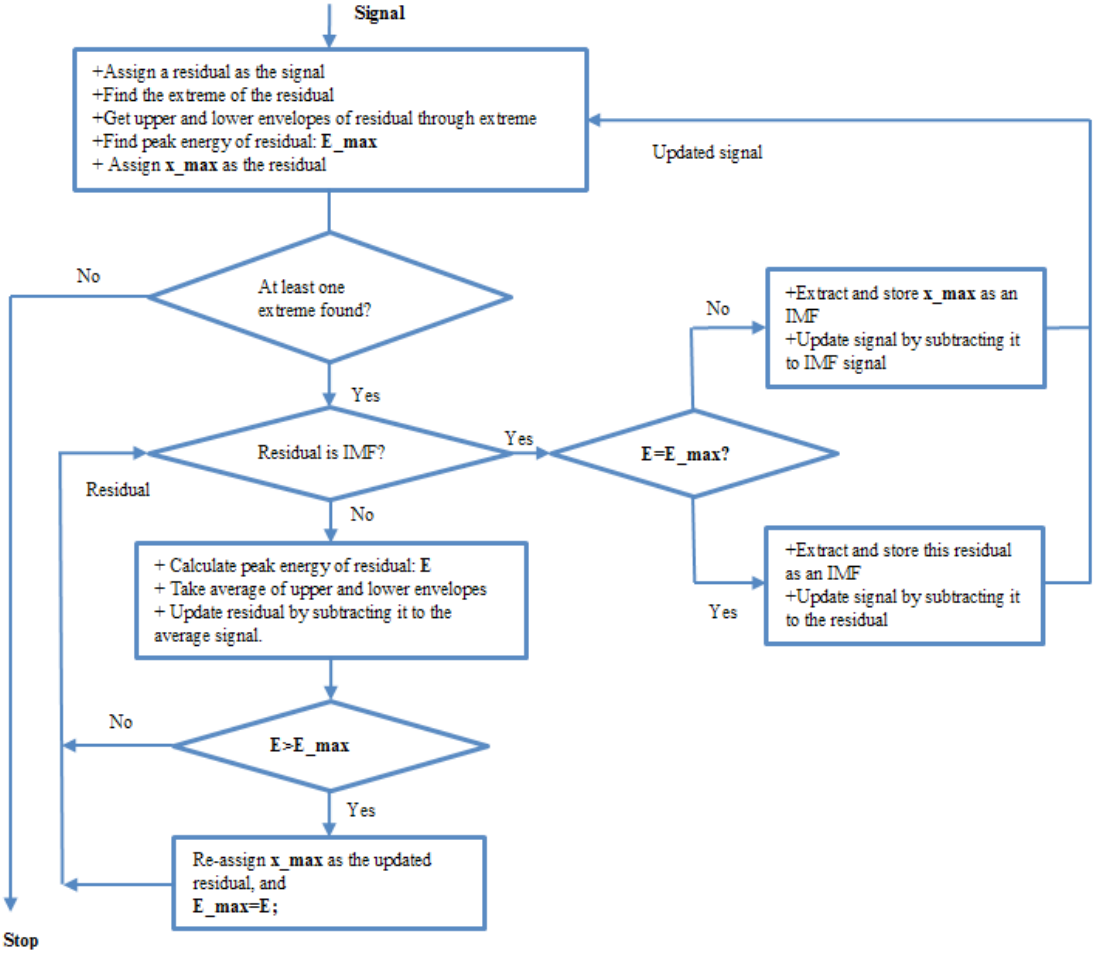

Fig. 2. *Flowchart of the proposed AEMD algorithm*

frequency f_{outer}, is 20 Hz and ringing pulse frequency is 1000 Hz.

3.2 Bearing Fault Detection with Envelope Analysis and Original EMD Methods

This section is aimed to show that the envelope analysis and the EMD method work when data are clean, and do not work when data are not.

The envelope analysis method [1] and [20] is used with both normal and faulty bearing simulation vibration data. The plots of the power spectrum of the signal after the envelope analysis are intuitively used to estimate the appearance of the nominal frequency of the outer race defect bearing. For the EMD method, it is used to generate the IMFs. With the nominal frequency of 20 Hz and ringing pulse frequency is 1000 Hz, the IMF #1 (IMF1) is selected. The Hilbert analytic signal of the IMF1 is generated. Then the plots of the power spectrum of the analytic signal are intuitively used. We use both methods for normal and faulty bearing data, which are supposed to indicate the appearance of the nominal frequency (20 Hz) in power spectrum plots for faulty bearing signal but do not for normal bearing data.

In Fig. 3, the differences between the normal and faulty bearing can be seen in Fig. 3b in Region I where the ringing pulse frequency components (around 1000 Hz) occur. Note that the ringing pulse frequency components only appear when the bearing fault is present. With this example, the f_{outer} (20 Hz) and its harmonics are clearly shown in the Figs. 3c and d. This proves that both envelope analysis and EMD methods work well for clean vibration data.

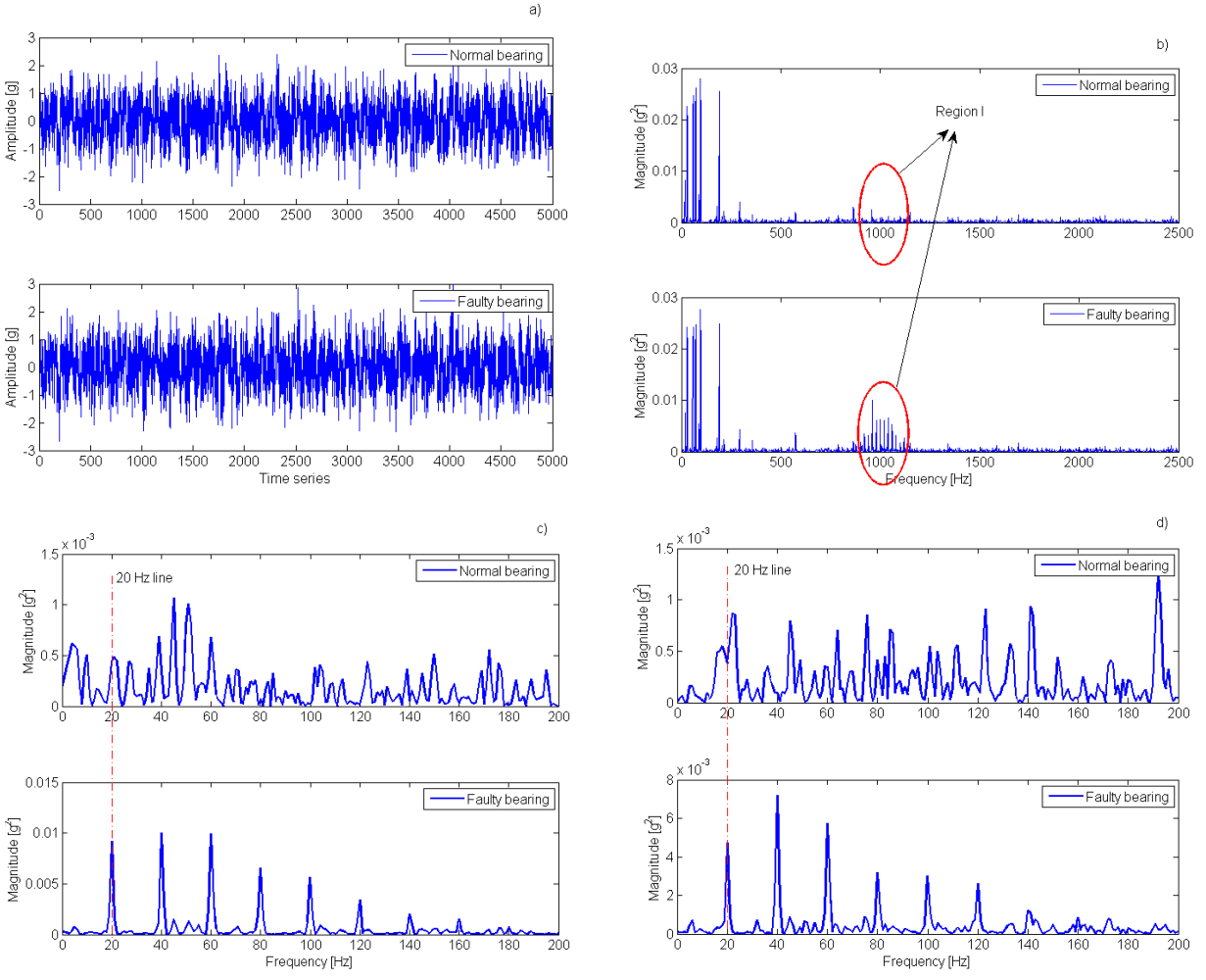

Fig. 3. *Simulation of bearing detection with envelope analysis and EMD method with clean vibration data; a) waveform of perfect and faulty bearing signal, b) power spectrum of perfect and faulty bearing signal, c) power spectrum of the outcomes with envelope analysis; here, the band-pass filtering for [500 Hz to1500 Hz] is applied in envelope analysis, and d) power spectrum of envelope signal of first IMF*

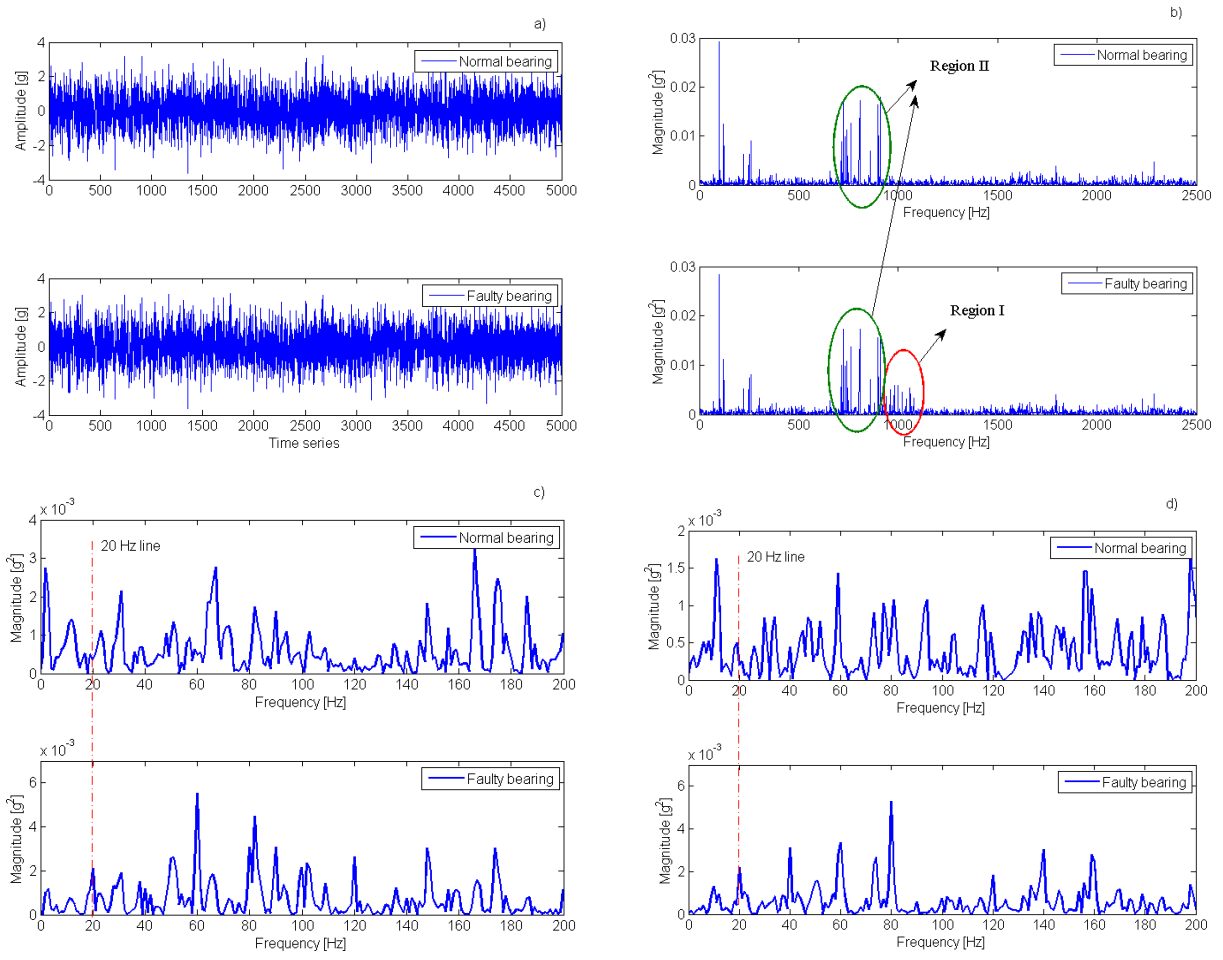

Fig. 4. *Simulation of bearing detection with envelope analysis and EMD method with disturbed vibration data, the disturbance is Region II; a) waveform of perfect and faulty bearing signal, b) power spectrum of perfect and faulty bearing signal, c) power spectrum of the outcomes with envelope analysis; here, the band-pass filtering for [500 Hz–1500 Hz] is applied in envelope analysis, and d) power spectrum of envelope signal of first IMF*

In Fig. 4, the differences between normal and faulty bearings are only in Region I; however, Region II close to region I which contains dominant components. As discussed before, Region II would cause both the envelope analysis and EMD to not work well. Indeed, looking at Fig. 4c and d, we are unable to emphasize the nominal defect bearing frequency, f_{outer} (20 Hz). Region II interfered with the outcomes of the both methods.

3.3 Comparison of Envelope Analysis, EEMD, and AEMD with Simulation Data

In this section, the bearing fault detection model provided in section 3 using AEMD will be compared with those of using EEMD and envelope analysis. The simulated data for an outer race defect bearing above

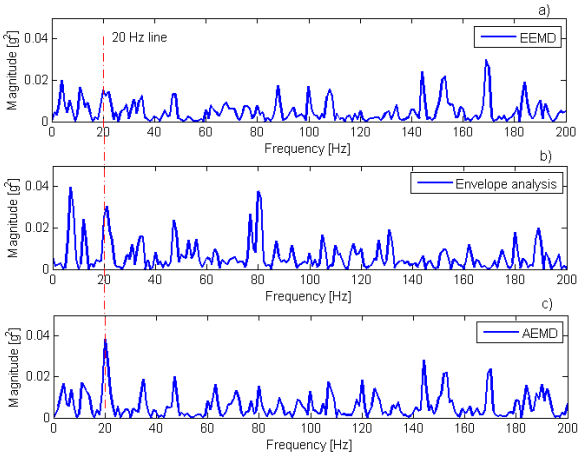

Fig. 5. *Comparison the power spectrum with three methods: a) EEMD, b) envelope analysis and c) adaptive EMD with simulation data*

is used. Fig. 5 shows the average power spectrum of 10 trials. The plots show that the amplitude of the nominal frequency with adaptive EMD is higher than that of with the EEMD and envelope analysis. It is also the highest peak found in the plots. The amplitude even cannot be recognized with EEMD method since it is not dominant and weak in comparison to other peaks in the plot. With envelope analysis, the amplitude is relatively high but not the most dominant one in the plot.

The performance of the AEMD method is intuitively better than ensemble EMD method and envelope analysis in terms of indicating the nominal defect frequency (20 Hz).

4 APPLICATION STUDY FOR BEARING FAULT DETECTION WITH THE AEMD METHOD

The test rig consisted of a genuine railway wagon bearing structure, where both the supporting bearings and test bearings were two-row roller bearings (SKF 229750). The shaft rotation speed could be adjusted between 0 rpm to 100 rpm. Furthermore, the loading of the test bearing was adjustable. For the test measurements, the rig was supplied with a bearing with a minor outer race defect as shown in Figs. 6a and b. In Fig. 6c, on the left are the two adjacent supporting bearings, the damaged bearing to be tested is in the middle, and on the right there are another two adjacent supporting bearings. The bearing parameters are provided in Table 1.

The experiment was carried out at a sampling rate of 4000 Hz, rotating of the input shaft of 79 rpm, and a load of 78 kN. Vibration data collected from vertical and horizontal accelerometers have a duration of 60 seconds and from both normal and outer race defect bearings.

Table 1. *Bearing parameters*

Number of rolling elements	22
Rolling element diameter	20 mm
Bearing pitch diameter	180 mm
Contact angle	18 degrees

With bearing parameters provided in Table 1, the nominal frequencies f_{outer} are 13 Hz calculated by Eq. (1).

In this experiment, the bearing parameters are known. To identify the fault happening on the outer race of the bearing, the bearing fault detection model must be able to indicate the appearance of the nominal frequency in the vibration data. This section is intended to use the proposed model mentioned

Fig. 6. *a) Location of the outer race damage; b) closer look at the damage; c) test rig; 1 supporting bearings, 2 test bearing, 3 load adjusting nut; d) sensor locations; 1 vertical acceleration, 2 horizontal acceleration, 3 axial acceleration 4 Acoustic emission sensor (magnetic fastening) and, 5 Acoustic emission sensor (screw fastening)*

in Section 3 for vibration data to detect the bearing fault. The bearing experimental data is analysed with the adaptive EMD. Following the bearing fault detection model mentioned in Section 3, both normal and faulty bearing data were applied with an adaptive EMD algorithm to extract 10 IMFs for each data. In our analysis, 10 IMFs are extracted and among them, via plots of the power spectrum of each IMF, the first IMF (IMF#1) is selected. The next step is to examine the amplitudes of the power spectrum of the first IMFs. Fig. 7 shows the plots of the power spectrum of the first IMFs of both normal and faulty bearing data. Since the power spectrum, amplitudes of high-frequency components are much smaller than those of low-frequency components, Fig. 7 is only for frequency components from 0 Hz to 40 Hz. It is clearly shown that the nominal frequency (13 Hz) has a very high amplitude in the bottom plot for faulty signals in comparison to the other frequency components. By contrast, the amplitude of 13-Hz-frequency component is negligible in the plot for the normal bearing. This confirms that the proposed model using the adaptive EMD algorithm can detect the bearing fault on the outer race.

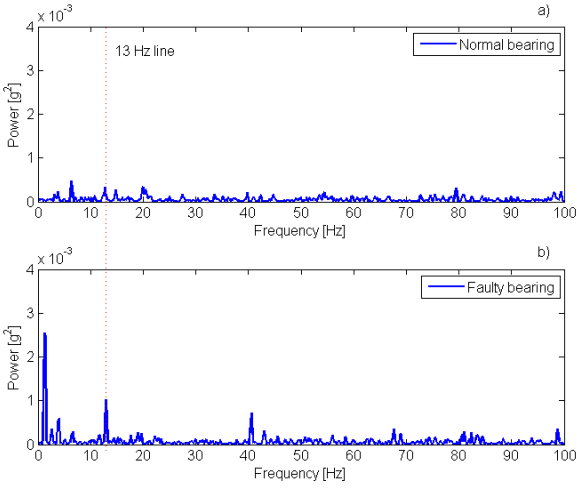

Fig. 7. *Power spectrum with adaptive EMD of envelope signal of IMF #1 of a) normal and b) faulty bearing data using proposed bearing fault detection method*

Moreover, Fig. 8 shows the advantages of the proposed method over the original EMD and envelope analysis methods in terms of identifying the appearance of the faults. With the envelope analysis, the fault, which appeared in 13 Hz, seems budding with a small peak. It is easily submerged by other peak components. The original EMD produced a better result with a higher peak, but it is not as high as the peak by the proposed method. In Fig. 8, it is clearly said that the adaptive EMD produced a better identification of the fault.

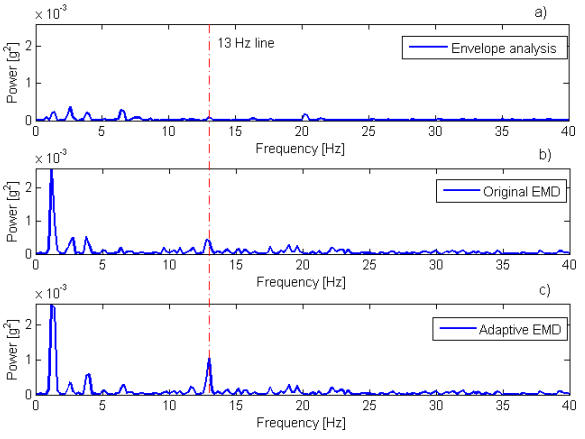

Fig. 8. *Comparison of power spectrum with faulty bearing of three methods; a) envelope analysis, b) original EMD and c) AEMD*

5 CONCLUSIONS

This paper introduces an AEMD algorithm. The advantage of the AEMD algorithm over the envelope analysis and the ensemble EMD algorithm in bearing fault detection is avoiding the fault signal energy shared among IMFs. The AEMD extracts IMFs so that the bearing fault signal will be mostly concentrated on one IMF. A performance comparison among bearing fault detection methods using envelope analysis, ensemble EMD and adaptive EMD with simulation data was carried out. It showed that the fault detection model using AEMD performs better than others. Moreover, we also validated the performance of the model with AEMD by the experimental data from practical bearing experiments. The result also indicated that the fault signature, presented by nominal frequencies, was clearly shown in the power spectrum plots.

6 REFERENCES

[1] Halme, J., Andersson, P. (2009). Rolling contact fatigue and wear fundamentals for rolling bearing diagnostics – state of the art. *Journal of Engineering Tribology*, vol. 224, no. 4, p. 377-393, **DOI:10.1243/13506501JET656**.

[2] Li, J. (1992). Bearing localized defect detection through wavelet decomposition of vibrations. Liang, S.Y., Wu, C.L. (eds.), *Sensors and Signals Processing for Manufacturing*, vol. 55, p. 187-197, American Society of Mechanical Engineers, New York.

[3] Howard, I. (1994). *A Review of Rolling Element Bearing Vibration "Detection, Diagnosis and Prognosis"*, Aeronautical

and Maritime Research Laboratory. Defence Science and Technology Department, Melbourne.

[4] Blau, P.J. (1992). *Friction, Lubrication, and Wear Technology,* ASM Handbook, vol. 18(), ASM International, Cleveland.

[5] Rai, V.K., Mohanty, A.R. (2007). Bearing fault diagnosis using FFT of intrinsic mode functions in Hilbert–Huang transform. *Mechanical Systems and Signal Processing*, vol. 21, no. 6, p. 2607-2615, **DOI:10.1016/j.ymssp.2006.12.004**.

[6] Peng, Z.K., Tse, P.W., Chu, F.L. (2005). A comparison study of improved Hilbert–Huang transform and wavelet transform: Application to fault diagnosis for rolling bearing. *Mechanical Systems and Signal Processing*, vol. 19, no. 5, p. 974-988, **DOI:10.1016/j.ymssp.2004.01.006**.

[7] Huang, N.E., Shen, Z., Long, S.R., Wu, M.C., Shih, H.H, Zheng, Q., Yen, N.C., Tung, C.C., Liu, H.H. (1998). The empirical mode decomposition and Hilbert spectrum for nonlinear and non-stationary time series analysis. *Proceeding of the Royal Society A*, vol. 454, no. 1971, p. 903-995, **DOI:10.1098/rspa.1998.0193**.

[8] Yu, Y., Yu, D.J., Cheng, J.S. (2006). A roller bearing fault diagnosis method based on EMD energy entropy and ANN. *Journal of Sound and Vibration*, vol. 294, no. 1-2, p. 269-277, **DOI:10.1016/j.jsv.2005.11.002**.

[9] Bin, G.F., Gao, J.J., Li, X.J., Dhillon, B.S. (2012). Early fault diagnosis of rotating machinery based on wavelet packets—Empirical mode decomposition feature extraction and neural network. *Mechanical Systems and Signal Processing*, vol. 27, p. 696–711, **DOI:10.1016/j.ymssp.2011.08.002**.

[10] Cheng, J., Yu, D., Yang, Y. (2006). A fault diagnosis approach for roller bearings based on EMD method and AR model. *Mechanical Systems and Signal Processing*, vol. 20, no. 2, p. 350-362, **DOI:10.1016/j.ymssp.2004.11.002**.

[11] Gao, Q., Duan, C., Fan, H., Meng, Q. (2008). Rotating machine fault diagnosis using empirical mode decomposition. *Mechanical Systems and Signal Processing*, vol. 22, no. 5, p. 1072-1081, **DOI:10.1016/j.ymssp.2007.10.003**.

[12] Wu, Z., Huang, N.E. (2009). Ensemble empirical mode decomposition: a noise assisted data analysis method. *Advances in Adaptive Data Analysis*, vol. 1, no. 1, p. 1-41, **DOI:10.1142/S1793536909000047**.

[13] Zhang, J., Yan, R., Gao, R.X., Feng, Z. (2010). Performance enhancement of ensemble empirical mode decomposition. *Mechanical Systems and Signal Processing*, vol. 24, no. 7, p. 2104-2123, **DOI:10.1142/S1793536909000047**.

[14] Do, V.T., Chong, U.P. (2011). Signal model-based fault detection and diagnosis for induction motors using features of vibration signal in two dimension domain. *Strojniški vestnik - Journal of Mechanical Engineering*, vol. 57, no. 9, p. 655-666, **DOI:10.5545/sv-jme.2010.162**.

[15] Kahaei, H.M., Torbatian, M., Poshtan, J. (2007). Bearing-fault detection using the Meyer-wavelet-packets algorithm. *Strojniški vestnik - Journal of Mechanical Engineering*, vol. 53, no. 3, p. 186-192.

[16] Li, Z., Ma, Z., Liu, Y., Teng, W., Jiang, R. (2015). Crack fault detection for a gearbox using discrete wavelet transform and an adaptive resonance theory neural network. Strojniški vestnik - Journal of Mechanical Engineering, vol. 61, no. 1, p. 63-73, **DOI:10.5545/sv-jme.2014.1769**.

[17] Lin, J., Zuo, M.J. (2003). Gearbox fault diagnosis using adaptive wavelet filter. *Mechanical Systems and Signal Processing*, vol. 17, no. 6, p. 1259-1269, **DOI:10.1006/mssp.2002.1507**.

[18] Chen, H.X., Chua, P.S.K., Lim, G.H. (2006). Adaptive wavelet transform for vibration signal modelling and application in fault diagnosis of water hydraulic motor. *Mechanical Systems and Signal Processing*, vol. 20, no. 8, p. 2022-2045, **DOI:10.1016/j.ymssp.2005.04.007**.

[19] Norton, M.P., Karczub, D.G. (2003). *Fundamentals of Noise and Vibration Analysis for Engineers*. Cambridge University Press, Cambridge, **DOI:10.1017/CBO9781139163927**.

[20] McInerny, S.A., Dai, Y. (2003). Basic vibration signal processing for bearing fault detection. *IEEE Transactions on Education*, vol. 46, no. 1, p. 149-156, **DOI:10.1109/TE.2002.808234**.

Strojniški vestnik - Journal of Mechanical Engineering 62(2016)5, 291-298

DOI:10.5545/sv-jme.2015.3305 Original Scientific Paper
Received for review: 2015-12-16
Received revised form: 2016-03-11
Accepted for publication: 2016-03-21

Effects of Laser Shock Peening on the Surface Integrity of 18 % Ni Maraging Steel

Luca Petan[1] – José Luis Ocaña[2] – Janez Grum[1,*]

[1] University of Ljubljana, Faculty of Mechanical Engineering, Slovenia
[2] Polytechnic University of Madrid, Laser Center, Spain

Maraging steels represent a special group of steels where ultrahigh strength is achieved with precipitation hardening. Because of their superior mechanical properties, maraging steels are used for the manufacturing of parts in the aerospace and tooling industry. Usually these mechanical components operate in demanding environments and conditions where they are subject to mechanical fatigue, thermo-mechanical fatigue, corrosion, and wear. The scope of the research presented in this paper is to analyze the effects of laser shock peening (LSP) on surface integrity characteristics of X2NiCoMo18-9-5 maraging steel. In this study, maraging steel specimens, in both quenched and aged condition, were treated with LSP by varying the pulse density. The effects of laser treatment on surface integrity were analyzed with roughness, residual stress, and microhardness measurements. According to the measurement results, LSP generated high compressive residual stresses in the steel surface layer with relatively low surface roughness, which indicates possible fatigue resistance improvements in 18 % Ni maraging steel.

Keywords: laser shock peening, dislocation, compressive residual stress, microhardness, surface roughness

Highlights

- *Maraging steel specimens were treated with LSP.*
- *Surface integrity of untreated and LSP treated maraging steel specimens was analyzed.*
- *LSP generated compressive residual stresses in the maraging steel surface layer.*
- *Strain hardening of the maraging steel surface layer occurred after LSP.*
- *High compressive residual stresses in combination with relatively low surface roughness can be achieved even without the use of an absorbent coating.*

0 INTRODUCTION

Maraging steels represent a special group of ultrahigh strength steels which can be hardened by precipitation of intermetallic compounds at temperatures around 480 °C [1]. These steels have a high content nickel, cobalt, and molybdenum, while the content of carbon, considered an impurity, is kept as low as possible. Commercially available maraging steels can reach yield strengths up to 2400 MPa. In addition to high strength, they are characterized by high resistance to thermal fatigue, high fracture toughness, and good weldability [2]. In order to achieve martensitic transformation during quenching, lower cooling rates are sufficient, and there is less probability for cracking to occur. During age hardening there is very little distortion. Therefore, parts can be machined to final dimensions before the aging process. Maraging steels were primarily developed as high strength structural materials, intended for applications in aeronautical and aerospace. Later on, because of their superior mechanical properties, maraging steels started to be used in the manufacturing of tools [3] such as molds and die-casting dies. Maraging steels are used for the manufacturing of mechanical parts and tools which operate in demanding environments and conditions where they are subject to mechanical fatigue, thermo-mechanical fatigue, corrosion, and wear. These phenomena have a negative effect on fatigue life and may cause an early failure of the mechanical part.

Fatigue behavior of highly stressed metallic components can be significantly improved by mechanical surface treatments [4] such as shot peening (SP) and laser shock peening (LSP). LSP is an innovative surface treatment [5] that can increase the fatigue strength of metallic parts by generating compressive residual stresses in the thin layer of the treated surface. During LSP, the surface of the treated component is exposed to nanosecond long laser pulses of intense energy from 5 J to 100 J [6]. The material in the interaction area with the laser beam vaporizes, and by further absorption of laser energy it ionizes and transforms into plasma. The newly created plasma continues to absorb the laser energy and generates pressure on the surface by transmitting shock waves into the treated material, Fig. 1. When shock wave stresses exceed the yield strength, plastic deformation occurs under the interaction zone between the laser beam and the material. The surrounding material prevents dilatation of the irradiated area of the surface layer, generating compressive residual stresses, which can reach depths up to 1 mm [7]. LSP treatment is far

*Corr. Author's Address: University of Ljubljana, Faculty of Mechanical Engineering, Aškerčeva 6, 1000 Ljubljana, Slovenia, janez.grum@fs.uni-lj.si

more effective if it is carried out in confined mode, where the metal surface is cowered with absorbent coating and confined by a transparent material like water or glass.

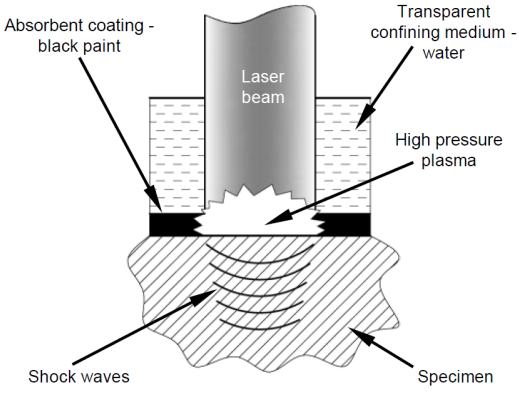

Fig. 1. *Schematic representation of the LSP process*

Another surface treatment method with the aim of increasing fatigue strength [8] is SP, whose development began in the late 1920s. During SP, the surface of the treated metallic component is exposed to a flux of small particles of high hardness. These particles, also called shot peening medium or simply shots, with a specific size and hardness, usually have a spherical shape and are made out of a metal, ceramic material, or glass. If the kinetic energy of the peening particle exceeds the yield strength threshold of the treated material, plastic deformation under the interaction zone will occur. Each particle, after a high-velocity impact, acts as a small hammer leaving a dent and generating a field of compressive residual stresses [9] and enhancing the hardness of the material [10]. By overlapping the impact zones during SP, or laser beam spots in case of LSP, it is possible to create a relatively uniform layer with compressive residual stresses.

An overview of scientific papers over the last few years shows there is an interest in investigating the possibility of applying surface peening techniques in order to improve the thermal and mechanical fatigue resistance of high-strength steels and tool steels. The first study on the effects of LSP treatment on maraging steel was carried out by Banas et al. [11]. Weldments of 18Ni(250) maraging steel were exposed to high-power short laser pulses using an Nd:YAG laser. A microstructural study showed an increased dislocation density in the heat-affected zone as a result of laser-shock loading. Fatigue test results indicated a 17 % increase in fatigue strength after LSP. Grum et al. [12] and [13] analyzed the effects of LSP on the thin surface layer of maraging steel X2NiCoMo12-8-8, which is suitable for the production of dies for die casting at temperatures of up to 600 °C. After LSP, compressive residual stresses up to 800 MPa were generated in the surface layer. Lavender et al. [14] carried out a study, whose objective was to investigate the effects of LSP on the life and failure behavior of pilger dies, made of A2 tool steel. After LSP, the life of the pilger dies, which was determined by in-process visual inspection of the tubes being processed, increased by 300 %.

Harada et al. [15] examined the influence of shot peening on the surface characteristics of AISI M2, a molybdenum-type high-speed steel. SP with cemented carbide microshots improved surface characteristics as compressive residual stresses up to 2000 MPa were generated near the surface at low surface roughness. The properties of cold work tool steel AISI D2 after SP by FeCrB gas atomized powder were analyzed by Sawada and Yanagitani [16]. Fatigue test results showed the higher fatigue strength of the peened specimens, which was attributed to crack initiation suppression caused by compressive residual stresses generated by the SP process.

Chang et al. [17] conducted various tests to evaluate the effects of shot peening on thermal cracking and mechanical properties of H13 hot work tool steel. Test results indicate that SP could increase the fatigue strength by two to three times due to the induced compressive stresses.

The main goal of the research presented in this paper is to investigate the effects of LSP treatment on the surface integrity of X2NiCoMo18-9-5 maraging steel with an emphasis on the residual stress state of the treated surface layer and surface roughness, which can have a significant influence on fatigue resistance. The strain hardening effect of LSP was also analyzed by performing in-depth microhardness measurements.

1 METHODS AND EXPERIMENTAL DETAILS

The research presented in this paper was carried out on maraging steel X2NiCoMo18-9-5 / DIN 1.6358, suitable not only as a high strength structural material, but also as a tool steel for molds and die casting tools. The chemical composition and mechanical properties of X2NiCoMo18-9-5 in quenched and artificially aged condition are given in Tables 1 and 2.

The chosen maraging steel was delivered as a soft annealed rolled plate with 9.5 mm thickness. In the first stage of our experimental work, square shape specimens measuring 40 mm × 40 mm were cut out of the maraging plate. The square specimens were then heat treated. The first phase of heat treatment consisted of solution annealing, for 1 h at a

Table 1. *Chemical composition of X2NiCoMo18-9-5 maraging steel (DIN 1.6358)*

Fe	C	Co	Ni	Mo	Ti	Al	Mn	Si	P	S
Bal.	≤0.03	8.0-10.0	17.0-19.0	4.5-5.5	0.5-0.8	0.05-0.15	≤0.10	≤0.10	≤0.01	≤0.01

Table 2. *Mechanical properties of X2NiCoMo18-9-5 maraging steel (DIN 1.6358)*

Heat treatment condition	Ultimate tensile strength R_m [MPa]	Yield strength $R_{p0.2}$ [MPa]	Young's modulus E [GPa]	Density ρ [kg/m³]	Rockwell Hardness HRC
QUENCHED	1070	870	195	8100	32 to 37
AGED	2050	1900			52 to 56

temperature of 820 °C, and cooling by air quenching. Afterwards, half of the quenched specimens were exposed to the age hardening process, performed for 3 h at a temperature of 480 °C. In order to achieve equal initial surface roughness conditions, all specimens were ground and polished. Heat treated and polished specimens were then exposed to laser shock peening in confined mode without an absorbent coating. Water was chosen as a transparent overlay. LSP was carried out using a Q-switched Nd:YAG laser with a wavelength of 1064 nm. The peening treatment was performed using three different laser pulse densities (900 cm^{-2}, 1600 cm^{-2}, 2500 cm^{-2}), while the laser pulse energy and duration were constant, i.e. 2.8 J and 10 ns. During LSP, the longitudinal direction of the laser beam path was parallel to the rolling direction, Fig. 2. Specimens with the corresponding designation and LSP processing parameters are listed in Table 3. Effects of the laser treatment on surface integrity were analyzed with roughness, residual stress (RS), and Vickers microhardness (HV) measurements.

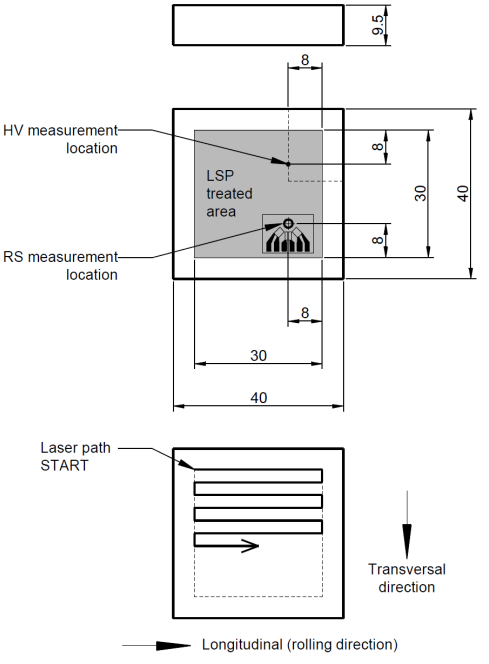

Fig. 2. *Specimen dimensions with the LSP treated area*

2 RESULTS AND DISCUSSION

2.1 Surface Roughness

Arithmetical mean deviation of the surface profile *Ra* (ISO 4287) **[18]** and mean roughness depth *Rz* (DIN 4768) **[19]** were the chosen surface parameters to describe the effects of the LSP treatment on surface roughness of maraging steel. Parameters *Ra* and *Rz* can give complementary information about the surface profile **[20]**. Roughness measurements were carried out using a Surtronic 3+ contact profilometer by Taylor Hobson, while the input data was processed with TalyProfile software.

The surface roughness of each specimen was calculated as the average between 5 longitudinal and 5 transversal measurements. The calculated average values with the corresponding standard deviations for parameters *Ra* and *Rz* are represented with column charts in Fig. 3 and Fig. 4, respectively. The initial topographic state, before exposure to the laser treatment, is represented by specimens Q and A. The

Table 3. *Specimens with the corresponding designation and LSP process parameters*

Specimen designation	Pulse density [cm^{-2}]	Laser spot diameter [mm]	Power density [GW · cm^{-2}]	Overlapping rate [%]
Q	-	-	-	-
Q-900	900	1.5	15.8	78
Q-1600	1600	1.5	15.8	83
A-2500	2500	1.5	15.8	87
A	-	-	-	-
A-900	900	1.5	15.8	78
A-1600	1600	1.5	15.8	83
A-2500	2500	1.5	15.8	87

arithmetic mean roughness of un-shocked specimens is around 0.17 μm. The column charts clearly show a significant increase in surface roughness after LSP was applied. The *Ra* of LSP treated quenched specimens and aged specimens ranges from 0.71 μm to 0.93 μm and from 0.69 μm to1.11 μm, respectively. Minimum roughness was achieved on specimens Q-900 and A-900, which were shock peened using 900 cm^{-2} pulse density. Specimens Q-2500 and A-2500, treated with the highest pulse density, have the highest *Ra* roughness. We can obtain similar findings for *Rz* roughness measurement results by comparing both column charts.

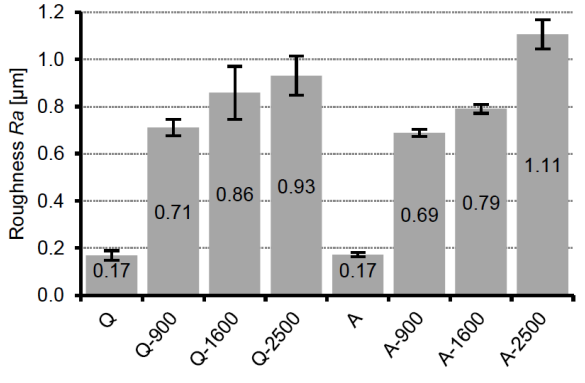

Fig. 3. *Roughness Ra of untreated and LSP treated maraging steel specimens*

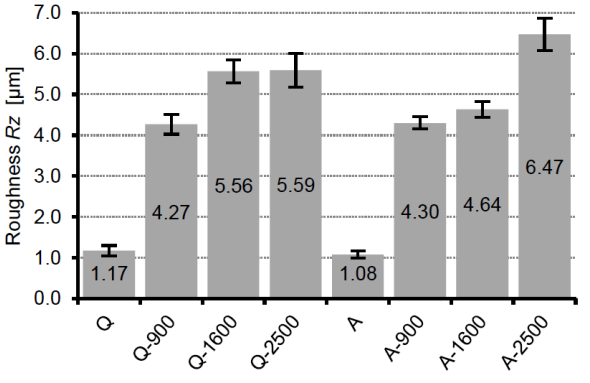

Fig. 4. *Roughness Rz of untreated and LSP treated maraging steel specimens*

Roughness measurements indicate that by increasing the LSP pulse density a surface with a higher *Ra* roughness is generated. The increase in surface roughness is a consequence of the combined effect of the laser pulse pressure and the ablative nature of the laser process. Surface roughness increases with higher pulse densities as a result of the cumulative effect of greater overlapping between the laser spots during LSP.

2.2 Residual Stress Distribution

Residual stress analysis of the surface layer was conducted following the standard hole-drilling strain-gage method ASTM E837 [21], according to which our maraging steel specimens can be considered as "thick" workpieces since their thickness of 9.5 mm is well above the minimum required value. According to ASTM E837, the workpiece thickness for a type B rosette should be at least 1.2*D* or 6.156 mm, where *D* represents the diameter of the gage circle and is 5.13 mm.

Blind holes were drilled with an RS-200 Milling Guide, while deformations due to relaxation during drilling were detected using CEA-06-062-UM strain gage rosettes by Vishay Measurement Group. The hole-drilling process on all maraging steel specimens was performed to a depth of 1.1 mm in a stepwise manner with an increment of 0.1 mm. Deformation values were recorded at each increment using LabVIEW. The residual stress distributions were then obtained by processing the deformation data with H-Drill software. Residual stresses were calculated using the integral method with automatic smoothing. In order to determine the effects of LSP on the residual stress state, measurements were carried out on both untreated and LSP treated specimens.

The residual stress measuring point was located on the LSP treated area and approximately 8 mm from the boundary as shown in Fig. 2.

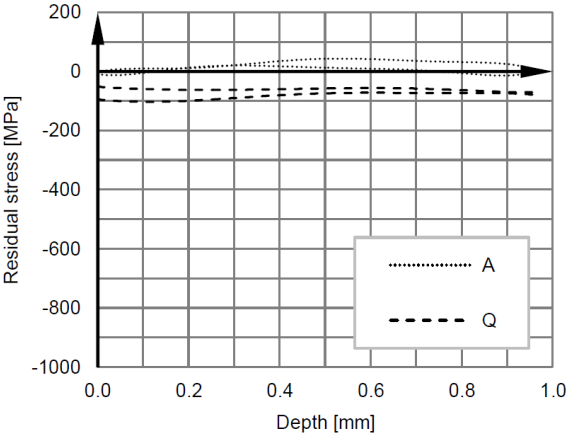

Fig. 5. *Residual stress distributions of untreated maraging steel specimens Q and A*

Charts represented in Figs. 5 to 7 show residual stress profiles in the thin surface layer of the maraging steel specimens, obtained by the hole-drilling strain-gage method. Each distribution is displayed using two curves, which represent the maximal and minimal

residual stress component. After LSP treatment, compressive residual stresses are generated in the surface layer because of the mechanical effects of shock waves, which exceed the dynamic yield strength of the maraging steel and cause plastic deformation.

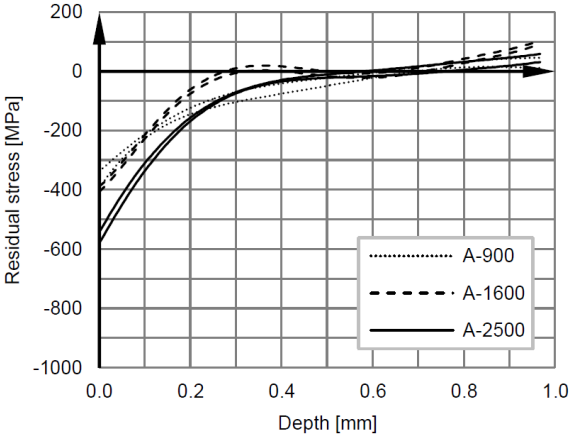

Fig. 6. *Residual stress distributions of LSP treated aged maraging steel specimens*

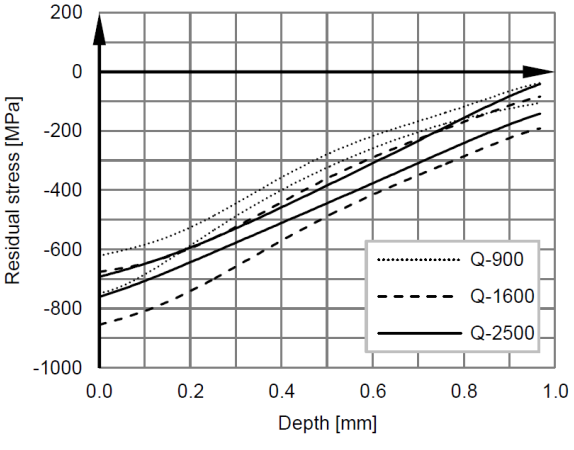

Fig. 7. *Residual stress distributions LSP treated quenched maraging steel specimens*

As can be observed in Fig. 6, which shows stress distributions after laser peening of aged maraging specimens, compressive stresses reach their maximum at the surface, ranging from –580 MPa to –340 MPa, while the transition from compressive to tensile state occurs at a depth of approximately 0.7 mm. The lowest compressive stress at the surface was measured on specimen A-900, treated with the lowest pulse density, while the maximum compressive value was noted on specimen A-2500, treated with the highest pulse density.

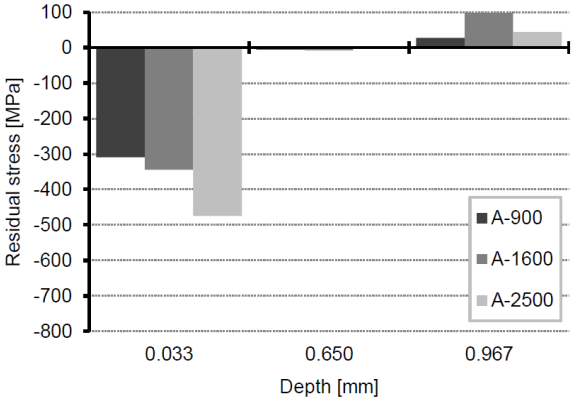

Fig. 8. *Residual stresses of LSP treated aged specimens*

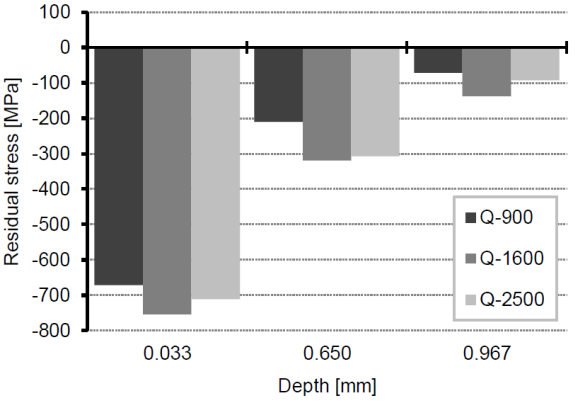

Fig. 9. *Residual stresses of LSP treated quenched specimens*

LSP generates higher and deeper compressive stresses in quenched maraging steel specimens, as shown in Fig. 7. This phenomenon can be attributed to a greater mechanical effect of shock waves due to the lower yield strength of the quenched condition. After LSP, surface stresses between –850 MPa and –620 MPa are detected. The difference in compressive stress generation is evident by comparing the column charts in Figs. 8 and 9. The value of each column was calculated as the average between the maximal and minimal stress component at the corresponding depth. Compressive residual stresses are still present at depth 0.967 mm in the surface layer of LSP treated quenched specimens. In the case of aged specimens, the transition from compressive to tensile state occurs already at depth 0.650 mm. Average tensile residual stresses at depth 0.967 mm in the surface layer of aged specimens amount between 30 MPa and 100 MPa. The compressive stresses near the surface and in-depth increase by using higher LSP pulse density. Higher stresses are a result of the cumulative effect of greater overlapping between the laser spots during LSP.

2.3 In-Depth Microhardness Distribution

The in-depth microhardness distribution was analyzed on specimens Q-2500 and A-2500, which were peened with the highest pulse density and should display more pronounced strain hardening of the surface layer. Microhardness was measured following the standard Vickers test method in accordance with ISO 6507-1:2005 [22]. The location of the in-depth measurement line is shown in Fig. 2. Indentations were carried out using a Vickers indentation unit, applied to a Leitz ORTHOPLAN microscope. The indentation force was performed with a 200 g load and 15 s load time. The image of the indentation was then captured through an Olympus ColorView III digital camera, while diagonal lengths were measured with AnalySISdocu software by Olympus Soft Imaging Solutions. Microhardness distribution was obtained with 20 in-depth measurements, where the distance between two separate indentations in the direction perpendicular to the LSP treated surface was 0.1 mm. The average microhardness of unpeened specimens Q and A was 341 HV 0.2 and 667 HV 0.2, respectively.

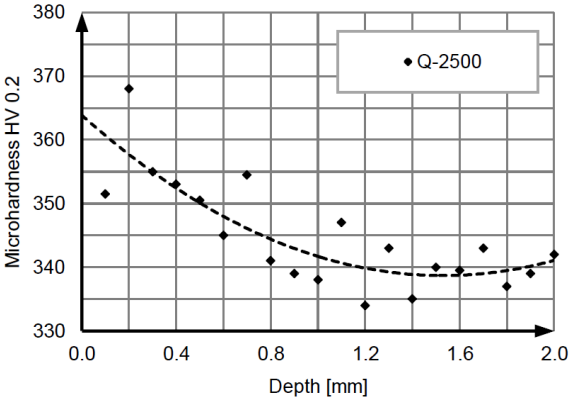

Fig. 10. *In-depth microhardness distribution of LSP treated aged specimen Q-2500*

In-depth microhardness distributions of the surface layer of laser peened maraging steel specimens Q-2500 and A-2500 are shown in Figs. 10 and 11, respectively. A polynomial trend line of the second order is added to determine if there is any change in the microhardness distribution due to the LSP treatment. As can be observed from the generated regression curves, strain hardening occurs after exposure to the LSP process. Strain hardening, as a consequence of the dislocation density increase due to the mechanical effect of shock waves, is detected as an increase in microhardness. Surface microhardness, determined at the intersection point between the vertical axis and the trend line, is 747 HV 0.2 for aged specimen A-2500, and 384 HV 0.2 for the quenched specimen Q-2500.

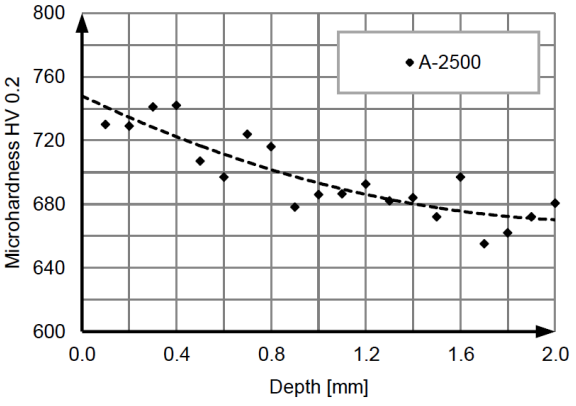

Fig. 11. *In-depth microhardness distribution of LSP treated aged specimen A-2500*

3 CONCLUSIONS

The effects of laser shock peening on the surface integrity characteristics of X2NiCoMo18-9-5 maraging steel were investigated. Specimens, in both quenched and artificially aged condition, were exposed to LSP using different laser pulse densities, while laser pulse energy and duration were constant. The investigated surface integrity characteristics were: surface roughness, in-depth microhardness, and residual stress distribution in the surface layer. In accordance with our research, the following conclusions were established:

- A significant increase in surface roughness, determined with *Ra* and *Rz* measurements, occurs after exposure to LSP. The increase in surface roughness is a consequence of the combined effect of the laser pulse pressure and the ablative nature of the laser process. A comparison between quenched and aged specimens shows similar *Ra* and *Rz* values after LSP treatment.
- After LSP treatment, compressive residual stresses are generated in the maraging steel surface layer due to the mechanical effects of shock waves, which cause plastic deformation. Compressive residual stresses are generated in all LSP treated specimens. LSP generates higher and deeper compressive stresses in quenched maraging steel specimens, ranging between –850 MPa and –620 MPa. The greater mechanical effect of shock waves is attributed to the lower yield strength of the quenched condition.

Compressive residual stresses increase by using higher LSP pulse density as a result of the cumulative effect of greater overlapping between the laser spots during LSP.

- LSP causes strain hardening in the maraging steel surface layer, which is detected as an increase in microhardness.

The performed surface integrity analysis shows that a combination of high compressive residual stresses and relatively low surface roughness can be achieved with the appropriate LSP processing parameters. While these surface characteristics may be beneficial for fatigue resistance of 18 % Ni maraging steel, other influential factors have to be taken into account, such as specimen thickness and the relative distance of edges of the LSP treated area from crack tips. When peening specimens of a few millimeters thick, local tensile residual stresses close to the edges of the LSP irradiated area may occur and have a detrimental effect. In order to confirm a beneficial effect of LSP on mechanical properties of X2NiCoMo18-9-5 maraging steel, fatigue testing should be conducted in future research.

4 ACKNOWLEDGMENTS

The authors would like to express their gratitude to the Laser Center of the Polytechnic University of Madrid and its staff for their assistance with the LSP treatment.

5 REFERENCES

[1] Rohrbach, K., Schmidt, M. (1990). Maraging steels. Davis, J.R. (ed.), *ASM Handbook Volume 1: Properties and Selection: Irons Steels and High Performance Alloys*. ASM International, Metals Park, p. 729-800.

[2] Decker, R.F., Floreen, S. (1988). Maraging steel - the first 30 years. *Maraging Steels Recent Developments and Applications - Proceedings of Symposium TMS Meeting*, p. 1-38.

[3] Cajner, F., Landek, D., Leskovšek V. (2010) Surface modifications of maraging steels used in the manufacture of moulds and dies. *Materials and Technology*, vol. 44, no. 2, p. 85-91.

[4] Nalla, R.K., Altenberger, I., Noster, U., Liu, G.Y., Scholtes, B., Ritchie R.O. (2003). On the influence of mechanical surface treatments - deep rolling and laser shock peening - on the fatigue behavior of Ti-6Al-4V at ambient and elevated temperatures. *Materials Science A*, vol. 355, no. 1-2, p. 216-230, **DOI:10.1016/S0921-5093(03)00069-8**.

[5] Trdan, U., Oca-a, J.L., Grum, J. (2011). Surface modification of aluminium alloys with laser shock processing. *Strojniški vestnik - Journal of Mechanical Engineering*, vol. 57, no. 5, p. 385-393, **DOI:10.5545/sv-jme.2010.119**.

[6] Bolger, J.A., Montross C.S., Rode, A.V. (1999). Shock waves in basalt rock generated with high-powered lasers in a confined geometry. *Journal of Applied Physic*s, vol. 86, no. 10, p. 5461-5466, **DOI:10.1063/1.371546**.

[7] Peyre, P., Fabbro, R., Merrien, P., Lieurade, H.P. (1996). Laser shock processing of aluminium alloys. Application to high cycle fatigue behaviour. *Materials Science and Engineering A*, vol. 210, no. 1-2, p. 102-113, **DOI:10.1016/0921-5093(95)10084-9**.

[8] Zupanc, U., Grum, J. (2011). Surface integrity of shot peened of 7075-T651 aluminium alloy. *Strojniški vestnik - Journal of Mechanical Engineering*, vol. 57, no. 5, p. 379-384, **DOI:10.5545/sv-jme.2010.142**.

[9] Schulze, V. (2006). *Modern Mechanical Surface Treatment*. WILEY-VCH Verlag GmbH & Co. KGaA, Weinheim.

[10] Žagar, S., Grum, J. (2011). Surface integrity after mechanical hardening of various aluminium alloys. *Strojniški vestnik - Journal of Mechanical Engineering*, vol. 57, no. 4, p. 334-344, **DOI:10.5545/sv-jme.2010.092**.

[11] Banas, G., Elsayed-Ali, H.E., Lawrence, F.V., Rigsbee, J.M. (1990). Laser shock-induced mechanical and microstructural modification of welded maraging steel. *Journal of Applied Physic*s, vol. 67, no. 5, p. 2380-2384, **DOI:10.1063/1.345534**.

[12] Grum, J., Zupančič, M., Oca-a, J.L. (2007). Laser shock processing of the maraging steel surface. *Materials Science Forum*, vol. 537-838, p. 655-662, **DOI:10.4028/www.scientific.net/MSF.537-538.655**

[13] Grum, J., Zupančič, M., Oca-a, J.L., Morales, M., Porro, J.A. (2008). Laser shock processing as a method of decreasing fatigue of a die-casting die made of maraging steel. *International Journal of Microstructure and Materials Properties*, vol. 3, no. 2/3, p. 271-281, **DOI:10.1504/IJMMP.2008.018734**.

[14] Lavender, C.A., Hong, S.-T., Smith, M.T., Johnson R.T., Lahrman, D. (2008). The effect of laser shock peening on the life and failure mode of a cold pilger die. *Journal of Materials Processing Technology*, vol. 204, no. 1, p. 486-491, **DOI:10.1016/j.jmatprotec.2008.02.002**.

[15] Harada, Y., Kobayashi, Y., Nagashima, E., Takeda, H. (2008). Influence of microshot peening on surface characteristics of high-speed tool steel. *Proceedings from the 10th ICSP*, Tokyo.

[16] Sawada, T., Yanagitani, A. (2010). Properties of cold work tool steel shot peened by 1200HV-class Fe-Cr-B gas atomized powder as shot peening media. *Journal of the Japan Institute of Metals*, vol. 51, no. 4, p. 735-739, **DOI:10.2320/matertrans.MBW200922**.

[17] Chang, S.-H., Tang, T.-P., Tai, F.-C. (2011). Enhancement of thermal cracking and mechanical properties of H13 tool steel by shot peening treatment. *Surface Engineering*, vol. 27, no. 8, p. 581-586, **DOI:10.1179/026708409X12490360425882**.

[18] ISO 4287:1997. *Geometrical Product Specifications (GPS) - Surface texture: Profile method - Terms, definitions and surface texture parameters*. International Organization for Standardization, Geneva.

[19] DIN 4768:1990-05: *Determination of values of surface roughness parameters Ra, Rz, Rmax using electrical contact (stylus) instruments; concepts and measuring conditions.* German Institute for Standardization, Berlin.

[20] Amaral, M.M., Raele, M.P., Caly, J.P., Samad, R.E., Vieira Jr, N.D., Freitas, A.Z. (2009). Roughness measurement methodology according to DIN 4768 using optical coherence tomography (OCT). *SPIE Proceedings - Modeling Aspects in Optical Metrology II*, vol. 7390, Bellingham, **DOI:10.1117/12.827748**.

[21] ASTM E837. *Standard Test Method for Determining Residual Stresses by the Hole-Drilling Strain-Gage Method*. ASTM International, West Conshohocken.

[22] ISO 6507-1:2005. *Metallic materials - Vickers hardness test - Part 1: Test method.* International Organization for Standardization, Geneva.

Strojniški vestnik - Journal of Mechanical Engineering 62(2016)5, 299-306

DOI:10.5545/sv-jme.2015.3200 Original Scientific Paper
Received for review: 2015-11-15
Received revised form: 2016-01-29
Accepted for publication: 2016-03-21

Ductile Behaviour Characterization of Low Carbon Steel: a CDM Approach

K Priya Ajit[1,*] – Abhinav Gautam[2] – Prabir Kumar Sarkar[2]
[1]Indian School of Mines, Department of Mining Machinery Engineering, India
[2]Indian School of Mines, Department of Mechanical Engineering, India

In this paper, the ductile behaviour of two different low carbon steels, C-Mn-440 and interstitial free high strength (IFHS), is presented using a continuum damage mechanics (CDM) approach. The damage growth law is adopted to predict the ductile response of the specified materials. Cyclic load-unload tensile tests in combination with standard uniaxial tensile tests helped to estimate the necessary parameters: damage variable, D, fracture stress, σ_f, threshold damage strain, ε_0, and strain hardening exponent, n, required to apply the model. The strain hardening exponent estimated from the cyclic test data is used to predict the damage variable, D. Increase of damage shows deterioration of the hardening exponent magnitudes varying nonlinearly. The simulated flow curve by the damage variable, D, corresponding to the load-unload test is observed to approximate the experimental true stress-true strain curve very closely up to the onset of necking for both the materials. The experimental values of D, as obtained for C-Mn-440 and IFHS steels, vary from 0.10 to 0.44 and 0.09 to 0.45, respectively. The critical damage parameters, D_C, for the considered materials are 0.44 and 0.45, representing their good ductile response.
Keywords: damage, continuum damage mechanics, modulus degradation, low carbon steel

Highlights
- *The damage parameter is evaluated experimentally through the cyclic load-unload tensile test.*
- *The direct relation between the strain-hardening exponent (n) and damage parameter (D) is revealed.*
- *The damage parameter estimated through chosen model are almost similar to experimental findings.*
- *The flow curve of both the materials coupled with damage shows similar behaviour as the true stress-strain curve before necking.*

0 INTRODUCTION

Ductile damage is a material behaviour demonstrated by diminishing strength with the increasing plastic strain until rupture of the load-bearing member. This is a consequence of micro-separation in metallic polycrystalline aggregates during severe local plastic flow assumed to be caused by a process of evolution of voids or cavities. Voids grow during a high degree of macroscopic plastic flow. These can appear inside the grains, eventually leading to transgranular fracture. The continuum damage mechanics (CDM) encompasses such micro-separations contained in a representative volume element (RVE) viewed at a mesoscale. It defines a damage variable as an effective surface density of void intersections in the RVE plane. A measure of damage helps in formulating its evolutionary laws necessary to depict the ductile response up to fracture for each of the engineering materials [1] and [2]. A constitutive law can then be used to predict the damage governed failure of the structure in service. Its evaluation may provide a guidance requisite to control and secure a better utilization of materials. It can also help post-fracture analysis of components to identify the cause of failure.

Many approaches have emerged to predict damage growth for different kinds of industrial applications since the seminal idea of CDM proposed by Kachanov [3] and Rabotanov [4] for creep in metals. Now damage mechanics is considered to be a viable framework to describe distributed material damage events such as material stiffness degradation, microcrack initiation, growth and coalescence, damage induced anisotropy, etc. Damage mechanics is pervasive in almost every dissipative material degradation process describing creep, fatigue, ductile and brittle damage by their respective model, incorporating the damage-governing parameter [5]. The scope and applications of damage mechanics are now widened to describe all large deformation behaviour for most of the engineering materials.

For nonlinear elastoplasticity coupled with damage as distributed interacting micro-voids, any clear micromechanical model is still a matter of future research. Krajcinovic [6] remarked that a purely micromechanical theory may never replace a properly formulated phenomenological theory as a design tool. The phenomenological CDM-based theories are proposed using the thermodynamics of an irreversible processes, the state variable theory along with physical considerations like the assumption of RVE in the definition of the micromechanical damage variable, the kinetic law of damage growth giving

*Corr. Author's Address: Indian School of Mines, Department of Mining Machinery, Dhanbad, India, ajit160984@gmail.com

strain energy release rate density, plasticity-damage coupling in terms of effective stress, etc.

CDM deals with the phenomena before crack initiation [7]. The CDM law describes the progressive loss of integrity of a material, measurable in terms of a scalar damage variable, D, to predict the ductile behaviour up to fracture. Damage mechanics depicts the microscopic events, such as ductile deformation, fatigue damage, creep, also embrittlement and stress corrosion [8] within its framework. In order to determine the ductile behaviour of a material from CDM, the influence of strain hardening exponent, n, on damage parameter or damage growth has not been explicitly considered thus far. It remains embedded in several damage flow models, however. It is a measure of formability, which is directly related to the ductility and void density. Thus, strain hardening can also be used as a measure of ductile damage. A uniaxial ductile damage model, developed by Bhattacharya and Ellingwood [8], relates damage as a function of plastic strain and strain hardening exponent. In this paper, damage variable estimation from the experimental hardening exponent is shown for the first time.

Low carbon steels, such as IFHS and C-Mn-440, show a good combination of strength and formability. These attributes aid in manufacturing shape-critical structures of automobiles. The current study is accordingly focused on the ductile damage behaviour estimation of these two steels using CDM. The study involves a load-unload cyclic test for direct estimation of the damage variable and other parameters required to show the influence of the strain-hardening exponent on the damage variable, D. The ductile flow behaviour then becomes predictable from the flow model invoking damage D in effective stress term.

1 CONTINUUM DAMAGE MODEL

In the CDM approach, damage is a process involving the growth of micro-voids and micro-cracks expressed by the volume density of micro-cracks and voids in RVE. Damage variable D is assumed to be isotropic, and it physically defines the surface density of one-dimensional micro-cracks and/or micro-separations contained in the plane of RVE. This effect is given by [2]:

$$D = \frac{\partial S_D}{\partial S}, \tag{1}$$

where ∂S_D is the cumulative surface area of micro cracks and ∂S represents the associated area of RVE planes. The critical values of D are D = 0 for undamaged condition and D = 1 for the fully damaged state called "rupture". Now the effective resisting area of undamaged part is assumed to be continuous so that $\partial(\tilde{S}) = \partial S - \partial S_D$. The corresponding effective stress is [2]:

$$\tilde{\sigma}\partial\tilde{S} = \sigma\partial S, \tag{2}$$

$$\tilde{\sigma} = \frac{\sigma\partial S}{\partial\tilde{S}} = \frac{\sigma}{1-D}, \tag{3}$$

here $\tilde{\sigma}$ is the effective stress. The stress in a material's virgin section is replaced by the effective stress term in its damage state. In case of multi-axial isotropic damage, the effective stress tensor is used [2]:

$$\tilde{\sigma}_{ij} = \frac{\sigma_{ij}}{1-D}. \tag{4}$$

Lemaitre [9] states that the strain associated with a stress level on the undamaged body is equivalent to the strain in its damaged state under effective stress. It can be expressed as:

$$\varepsilon = \frac{\sigma}{E} \text{ (undamaged state)}, \tag{5}$$

$$\varepsilon = \frac{\tilde{\sigma}}{E} = \frac{\sigma}{(1-D)E} \text{ (damaged state)}. \tag{6}$$

By using Eqs. (5) and (6), the ductile damage variable becomes:

$$D = 1 - \frac{\tilde{E}}{E}, \tag{7}$$

where $\tilde{E}$ the effective elasticity modulus of damaged material and E is the Young's modulus of virgin material. This relation is one of the best way of expressing ductile damage.

1.1 Thermodynamics of Damage

Evolution of damage is associated with a thermodynamic potential which is the Helmholtz specific free energy ψ. It is assumed here that elasticity and plasticity are uncoupled and provides the law of thermoelasticity coupled with damage [10] and [11]:

$$\psi = \psi_e(\varepsilon_e, T, D) + \psi_P(T, h), \tag{8}$$

where ψ_e is the elastic contribution and function of state variables; ε_e the elastic strain tensor, T the temperature and D the damage variable while ψ_p is the plastic contribution taken to be the function of state variables: temperature T and isotropic hardening h. Treating W_e as the elastic strain energy density (ESED), the elastic energy density release rate (EDRR), Y, becomes:

$$-Y = \frac{W_e}{(1-D)} = \frac{1}{2}\frac{dW_e}{dD}\Big|(\sigma \text{ and } T = \text{constant}). \tag{9}$$

From the concept of strain equivalence and damage equivalent stress, W_e can be expressed in terms of shear energy and hydrostatic energy. Correspondingly, the ESED becomes:

$$W_e = \rho\psi_e^* = \frac{1+\upsilon}{2E}\frac{\sigma_{ij}^D\sigma_{ij}^D}{(1-D)} + \frac{3(1-2\upsilon)}{2E}\frac{\sigma_H\sigma_H}{(1-D)} = \\ = \frac{1+\upsilon}{2E}\left(\frac{2}{3}\right)\frac{\sigma_{eq}^2}{(1-D)} + \frac{3(1-2\upsilon)}{2E}\frac{\sigma_H^2}{(1-D)}. \quad (10)$$

Substituting W_e from Eq. (10) in Eq. (9), the EDRR, Y, becomes:

$$-Y = \frac{\sigma_{eq}^2}{2E(1-D)^2}\left[\frac{2}{3}(1+\nu) + 3(1-2\nu)\left(\frac{\sigma_H}{\sigma_{eq}}\right)^2\right] = \\ = \frac{\tilde{\sigma}_{eq}^{\ 2}}{2E}R_v, \quad (11)$$

where σ_H is the hydrostatic stress, $\sigma_{eq} = \sqrt{\left[(3/2)\sigma^D\cdot\sigma^D\right]}$ represents the Mises equivalent stress in which σ^D is the deviatoric stress part of the applied stress state and $\sigma^D\cdot\sigma^D$ is a tensor product. In Eq. (11), σ_H/σ_{eq} is the triaxiality ratio. The ductility measure at fracture decreases as the triaxiality ratio increases [9]. Accordingly R_v is a function of the triaxiality ratio. This is expressed as:

$$R_v = \frac{2}{3}(1-\nu) + 3(1-2\nu)\left(\frac{\sigma_H}{\sigma_{eq}}\right)^2. \quad (12)$$

Most of the CDM models are proposed in terms of dissipation potential and damage variables [10]. The thermodynamic approach ensures that the damage rate $\dot{D}$ be governed by the plastic strain which is introduced through the plastic multiplier ($\dot{\lambda}$) and dissipative damage potential (F_D). According to Lemaitre, the damage rate is given by:

$$\dot{D} = \dot{\lambda}\frac{\partial F_D}{\partial Y}. \quad (13)$$

The plastic multiplier, ($\dot{\lambda}$), represents a scalar multiplier ensuring normal condition of yield function for plastic flow, can be evaluated from the modified constitutive equation of plasticity coupled with damage.

$$\dot{\epsilon_p} = \frac{\dot{\lambda}}{1-D}. \quad (14)$$

Based on the various experimental results, the damage dissipation potential (F_D) is found to be a nonlinear function of EDRR (Y). The expression of F_D is given by:

$$F_D = \frac{S}{(N+1)(1-D)}\left(\frac{Y}{S}\right)^{N+1}, \quad (15)$$

where N is the unified damage law exponent and S signifies energetic damage law parameter. These parameters are a function of temperature and assume a different value for different material.

Substituting $\dot{\epsilon_p}$, the plastic strain rate and F_D, the damage dissipation potential, from Eqs. (14) and (15) into Eq. (13), the unified damage law becomes:

$$\dot{D} = \begin{cases} \left(\frac{Y}{S}\right)\dot{\epsilon_p} & \text{if } \dot{\epsilon_p} \geq \epsilon_0 \\ 0 & \text{if } \dot{\epsilon_p} < \epsilon_0 \end{cases}. \quad (16)$$

The unified damage law under monotonic loading assumes that hardening saturates at σ_u, the ultimate strength. The equivalent stress is then equal to σ_u. Combining Eq. (11) and Eq. (16) also setting R_V=1, the relation for damage rate modifies to:

$$\dot{D} = \left(\frac{\sigma_u^2}{2ES}\right)^N\dot{\epsilon_p}. \quad (17)$$

Then damage parameter D becomes:

$$D = \left(\frac{\sigma_u^2}{2ES}\right)^N(\epsilon_p - \varepsilon_0), \quad (18)$$

where, ϵ_p is plastic strain and ε_0 represents threshold-accumulated plastic strain.

At the seizure of damage evolution, a mesocrack is initiated when the density of defects reaches a value for which the process of localization and instability develops. This represents a material property called "critical damage value", D_C. This is expressed as:

$$D_c = \left(\frac{\sigma_u^2}{2ES}\right)^N(\epsilon_{pR} - \varepsilon_0), \quad (19)$$

where ϵ_{pR} is the local rupture strain in the necking region. Other parameters are as defined above.

1.2 Damage Growth Model for Ductile Material under Uniaxial Loading

In the ductile flow of materials, the strain acts through their difference:

$$\varepsilon_e = \varepsilon - \varepsilon_p, \quad (20)$$

where ε_e is elastic strain, ε_p is plastic strain and ε is the total strain.

A Ramberg-Osgood material obeys the constitutive law:

$$(\sigma / E) = \varepsilon - (\sigma / K)^{1/n}, \quad (21)$$

where, E is the elastic modulus, K is the hardening modulus and n is the strain-hardening exponent.

The free energy per unit volume, ψ, associated with the isotropic damage growth during ductile deformation has its general form presented in [1]:

$$\psi = \int \sigma_{ij} d\varepsilon_{ij} - \gamma(D), \quad (22)$$

where γ is the surface energy of voids and discontinuities that arise due to damage growth, specified per unit volume.

By adding the influence of effective stress and effective strain parts, associated with damage, the elastic and plastic components in Eqs. (20) and (21) are modified. These when used to evaluate the first term of Eq. (22) yeild:

$$\int_0^{\varepsilon} \sigma d\varepsilon = \int_0^{\varepsilon_{e0}} E\varepsilon_e d\varepsilon_e + \int_{\varepsilon_{e0}}^{\varepsilon_e} E(1-D)\varepsilon_e d\varepsilon_e + \int_0^{\varepsilon_p} K{\varepsilon_p}^n d\varepsilon_p + \int_{\varepsilon_0}^{\varepsilon_p} K(1-D)\varepsilon_p^n d\varepsilon_p, \quad (23)$$

where ε_p is plastic strain, ε_0 is threshold strain at the onset of damage growth. The second term, the surface energy density, evaluated from the energy of deforming a plane circle void to a spherical volume, is given as [1]:

$$\gamma = \frac{3}{4}\sigma_f D, \quad (24)$$

where σ_f signifies the true fracture stress. The growth rate of damage with respect to plastic strain is [1]:

$$\frac{dD}{d\varepsilon_p} = -\frac{\sigma_\infty}{\psi_D}\frac{d\varepsilon}{d\varepsilon_p}, \quad (25)$$

where $\psi_D = \partial\psi/\partial D$, is the rate of change of free energy with respect to damage D.

Using the strain equivalence condition of damage the Hollomon plastic flow rule is modified to $\sigma_\infty = K(1-D)\varepsilon_p^n$, where σ_∞ is the remote stress.

By partial differentiation of Eq. (22) with respect to D, gives ψ_D, obtainable as:

$$\psi_D = -\frac{K^2}{2E}\left[\varepsilon_p^{2n} - \varepsilon_0^{2n}\right] - \frac{K}{1+n}\left[\varepsilon_p^{1+n} - \varepsilon_0^{1+n}\right] - \frac{3}{4}\sigma_f. \quad (26)$$

Now, differentiating Eq. (20), with respect to plastic strain, one can find:

$$\frac{d\varepsilon}{d\varepsilon_p} = 1 + \frac{d\varepsilon_e}{d\varepsilon_p}. \quad (27)$$

For the entire practical ductile damage strain range, a near close form solution to Eq. (25) can be obtained by putting $d\varepsilon/d\varepsilon_p$ equivalent to 1 and $K/(2E)$ equivalent to 0. Accordingly, the damage law becomes:

$$D = 1 - \frac{C_2}{\varepsilon_p^{1+n} + C_1}. \quad (28)$$

At the onset of damage evolution, $D=0$ and $\varepsilon_p = \varepsilon_0$. Thus, the constants in Eq. (28) can be estimated from:

$$C_1 = \frac{3}{4}(1+n)\frac{\sigma_f}{K} - \varepsilon_0^{1+n}, \quad (29)$$

$$C_2 = C_1 + \varepsilon_0^{1+n}. \quad (30)$$

For most ductile metals and alloys, the constant C_1 is greater than the plastic strain range of interest. For such a condition, Eq. (28) simplifies to:

$$D = 1 - \frac{C_2}{C_1} + \frac{C_2}{C_1^2}\varepsilon_p^{1+n}. \quad (31)$$

This law, in Eq. (31), specifies damage to be a function of plastic strain and strain hardening exponent.

2 EXPERIMENTAL RESULTS AND DISCUSSION

Among all different possible non-direct methods identified for ductile damage measure of metal under a large amount of deformation, elasticity modulus degradation measure is found to be the most suitable [2]. To evaluate D, a load-unload cyclic tensile test is carried out upto fracture. The effective elastic modulus corresponding to each cycle is captured to estimate D. Other parameters used in the damage law are obtained from load-unload cyclic test as well as uniaxial tensile test for specimens of IFHS and C-Mn-440 steels conforming to ASTM E8 standards [12].

2.1 Uniaxial Tensile Test Evaluation

A uniaxial tensile test is conducted on Instron 8801 keeping strain rate of 10^{-3} s^{-1}. Fig. 1 presents a representative stress-strain diagram for both the materials. Corresponding mechanical properties are presented in Table 1. C-Mn-440 has higher strength, but IFHS steel shows better ductility.

Table 1. Mechanical property of steel

Property	C-Mn-440	IFHS
Yield strength [MPa]	320.97	258.16
Tensile strength [MPa]	452.26	387.59
Elongation [%]	36.55	44.03
Uniform strain [%]	26.2	33.6

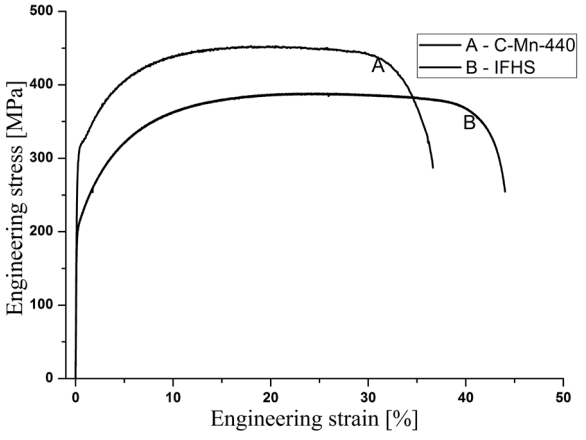

Fig. 1. *Stress-strain curve*

2.2 Load-Unload Tensile Test Evaluation

The damage variable of D is obtained from Eq. (7). Each cycle proceeds with a position controlling of cross-head displacement followed by unloading limit. The tests are performed on Instron 8801 universal testing machine with a strain rate of 10^{-3} s^{-1} in a load-control mode. A set of three specimens are taken for each of the materials. The clip extensometer of 25 mm gauge length gives the strain measure. Fig. 2 provides the resulting stress-strain curve for both the steels. These are used to evaluate D of each cycle. The effective elasticity modulus for each cycle is the slope taken from 15 % to 85 % of the unloading path. This eliminates the effect of nonlinearity at the beginning and the end of the cycle.

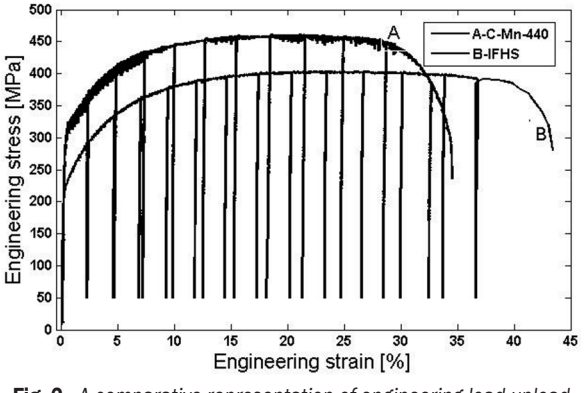

Fig. 2. *A comparative representation of engineering load-unload experimental curves for C-Mn-440 and IFHS Steels*

The effective elastic modulus with increment in plastic strain for each cycle is found to remain almost linear for either of the steels (Fig. 3). The respective values for C-Mn-440 steel varies from 174.65 GPa to 97.63 GPa in the strain range of 2.2 % to 32.4 % and for the IFHS steel, these are from 178.24 GPa to 98.73 GPa in the strain range of 2.2 % to 36 %. The variations in isotropic damage parameter, D, for the chosen steels are shown in Fig. 4. D increases with plastic deformation almost linearly for both the materials. Its magnitudes for C-Mn-440 and IFHS steel are from 0.10 to 0.44 and 0.09 to 0.45, respectively. These are well within the specified range suggested by Lemaitre and Dufailly [2]. At the onset of rupture, D is considered to be critical damage, D_c .Its values for C-Mn-440 and IFHS steels are recorded to be 0.44 and 0.45 respectively. This also conforms to the limits suggested by Lemaitre.

2.3 Effect of Hardening Exponent

From the above-stated test data, variations of strain hardening exponent can be estimated by taking the slope of true stress-strain curve of each step in load-unload cycle test. The Hollomon constitutive relation [13] is used for the purpose:

$$\sigma = K\varepsilon^{n}. \tag{32}$$

Here, K is the hardening modulus and n designates the strain hardening exponent. The hardening exponent is then obtainable as:

$$n = \frac{d(\log\sigma)}{d(\log\varepsilon)}. \tag{33}$$

The constants in ductile damage model, described in Eq. (31), are now obtainable from the experimental result for both the materials incorporating data from Table 2. A continuous decrement in the hardening exponent is observable up to necking (Fig. 5). This is in agreement with the concept of density deterioration during large tensile elongation. Furthermore, the void density increases with increasing plastic strain [14]. The increase in the void density reduces the effective area available for carrying load, and consequently, the stiffness of the material. With the increase in load, the phenomena of void evolution, growth and coalescence lead to macro-crack formation and growth upto fracture. Thus, a decrease in the hardening exponent increases the rate of damage. The same is observable in the model given by Bhattachrya and Ellingwood (Eq. (31)). These results are shown in Fig. 5 for both of the materials. The damage variable, D, obtained from the test and the model (Eq. (31)) are compared, after incorporating the values of the strain-hardening exponent to indicate the influence of the exponent, in Fig. 6.

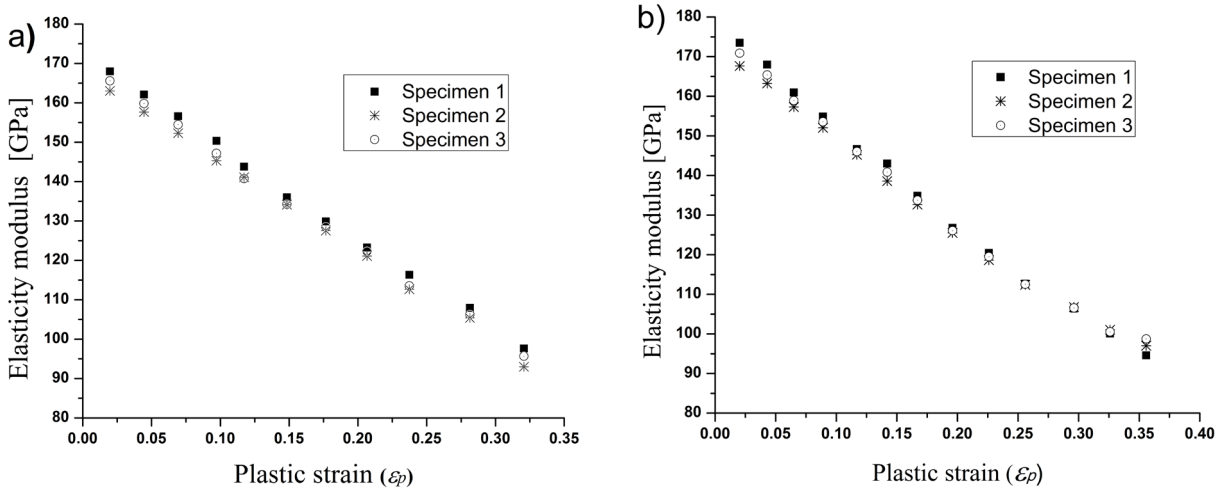

Fig. 3. *Progressive degradation of elastic modulus with strain increment; a) for C-Mn-440 steel, and b) for IFHS steel*

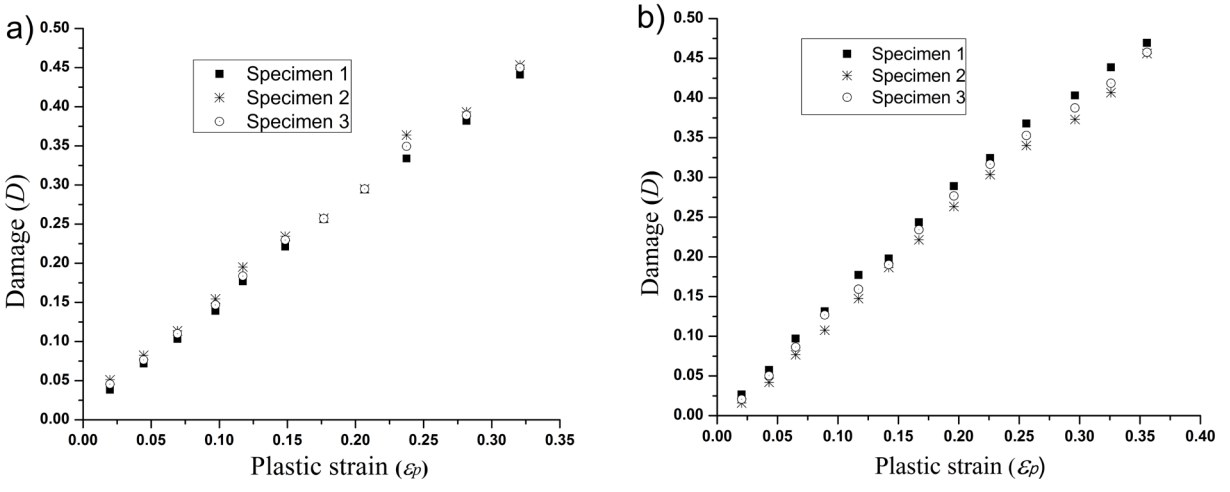

Fig. 4. *Damage evolution with increase in plastic strain; a) for C-Mn-440 steel, and b) for IFHS steel*

Table. 2 *The property values of hardening modulus (K), threshold plastic strain (ε_0) and fracture stress (σ_f) for each of the materials*

Material	True fracture strength (σ_f) [MPa]	Hardening modulus (K) [MPa]	Threshold strain (ε_0)
C-Mn-440	600	732	0.0198
IFHS	515	694	0.020

2.4 Flow Curve Simulation with Damage

The experimental isotropic damage variable is used as the input parameters to recreate the flow characteristic of both the materials. This is designated as the simulated flow curve. These are then compared with the true stress-strain flow curve from the uniaxial tensile test. These are shown in Fig. 7. Good agreement up to the onset of necking is visible. Beyond this point, the curve deviates due to unpredictable change of triaxiality factor. A similar nature of flow curve is observable with AISI1090, AISI1045 and DP590 steels **[15]** and **[16]**.

3 CONCLUSION

An experimental determination of the ductile damage response of C-Mn-440 and IFHS steel is presented. The indirect method of damage evaluation from the load-unload cyclic test is employed to estimate damage variable D and the strain hardening exponent, n. D is shown to be obtainable from the chosen damage growth model (Eq. (31)) by applying strain hardening index, n. The D values for both the materials, obtained from test and by the damage growth law remarkably show identical results. This justifies the fact that strain hardening exponent can also be used as a damage growth measure. The flow curves obtained

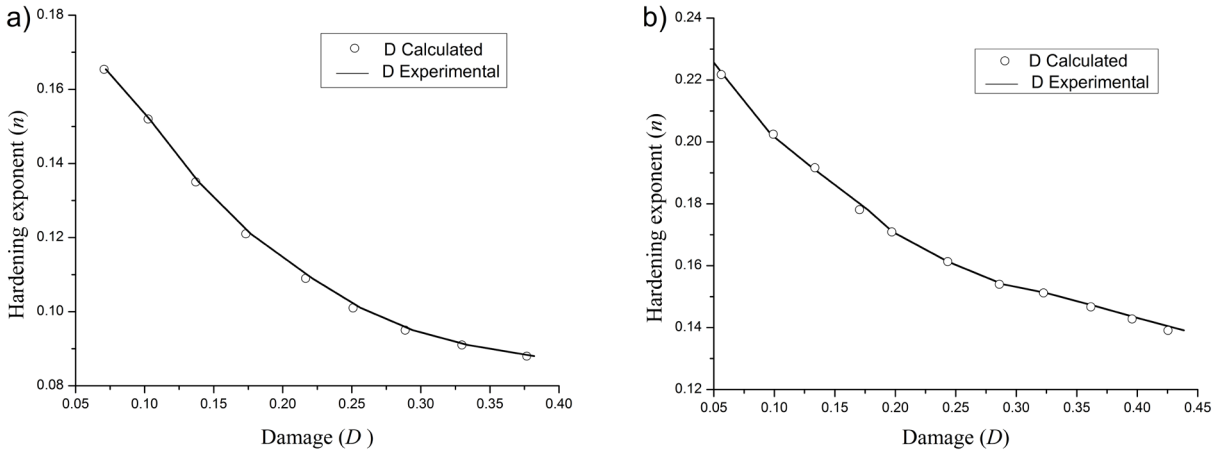

Fig. 5. *Variation of damage with hardening exponent; a) for C-Mn-440, and b) for IFHS*

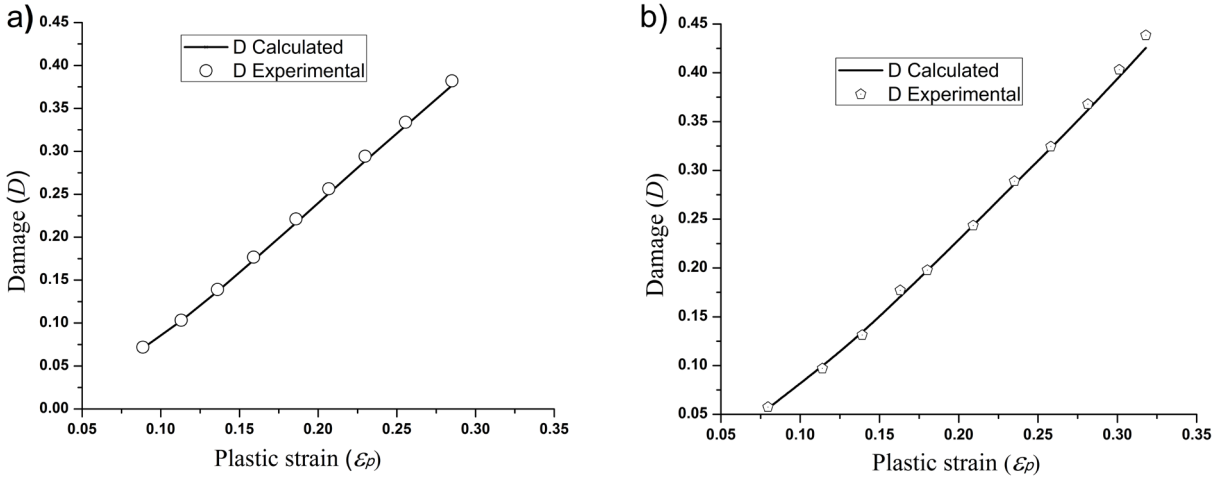

Fig. 6. *A comparison of damage parameter; a) for C-Mn-440, and b) for IFHS*

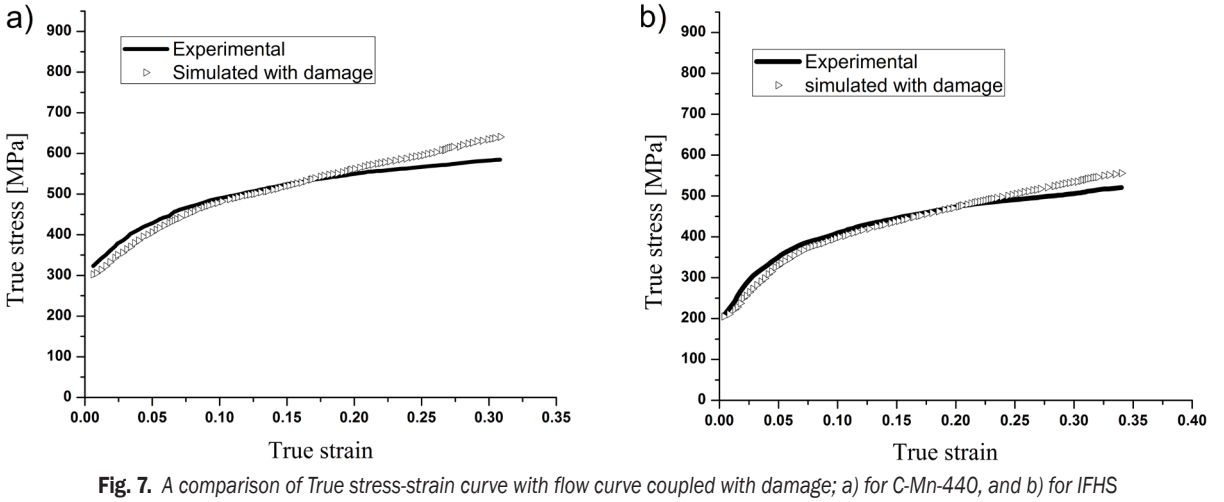

Fig. 7. *A comparison of True stress-strain curve with flow curve coupled with damage; a) for C-Mn-440, and b) for IFHS*

from uniaxial tensile test for both the materials are compared with the simulated CDM-based flow results using the effective stress concept. The flow curves are in close agreement. The chosen model helped to establish that an estimation of strain hardening exponent from load-unload cyclic test is possible, and

it can be used for ductile behaviour estimation. The test data confirms the chosen materials display good ductile in response.

4 REFERENCES

[1] Bhattacharya, B., Ellingwood, B. (1999). A new CDM-based approach to structural deterioration. *International Journal of Solids and Structures*, vol. 36, no. 12, p. 1757-1779, **DOI:10.1016/S0020-7683(98)00057-2**.

[2] Lemaitre, J., Dufailly, J. (1987). Damage measurements. *Engineering Fracture Mechanics*, vol. 28, no. 5-6, p. 643-661, **DOI:10.1016/0013-7944(87)90059-2**.

[3] Kachanov, L.M. (1999). Rupture time under creep conditions. *International Journal of Fracture*, vol. 97, no. 1, p. 11-18, **DOI:10.1023/A:1018671022008**.

[4] Rabotanov, Y.N. (1969). *Creep Problem in Structural Members.* Wiley, Amsterdam.

[5] Lemaitre, J. (1984). How to use damage mechanics. *Nuclear Engineering and Design*, vol. 80, no. 2, p. 233-245, **DOI:10.1016/0029-5493(84)90169-9**.

[6] Krajcinovic, D. (1985). Continuous damage mechanics revisited: Basic concepts and definitions. *Journal of Applied Mechanics*, vol. 52, no. 4, p. 829-834, **DOI:10.1115/1.3169154**.

[7] Chaboche, J.L. (1981). Continuous damage mechanics - A tool to describe phenomena before crack initiation. *Nuclear Engineering and Design*, vol. 64, no. 2, p. 233-247, **DOI:10.1016/0029-5493(81)90007-8**.

[8] Bhattacharya, B., Ellinwood, B. (1998). Continuum damage mechanics analysis of fatigue crack initiation. *International Journal of Fatigue*, vol. 20, no. 9, p. 631-639, **DOI:10.1016/S0142-1123(98)00032-2**.

[9] Lemaitre, J. (1985). A continuous damage mechanics model for ductile fracture. *Journal of Engineering Materials and Technology*, vol. 107, no. 1, p. 83-89. **DOI:10.1115/1.3225775**.

[10] Chaboche, J.L. (1988). Continuum damage mechanics: Part I-General concept. *Journal of Applied Mechanics*, vol. 55, no. 1 p. 59-64, **DOI:10.1115/1.3173661**.

[11] Chaboche, J.L. (1988). Continuum damage mechanics: Part II-damage growth, crack initiation, and crack growth. *Journal of Applied Mechanics*, vol. 55, no. 1, p. 65-72, **DOI:10.1115/1.3173662**.

[12] ASTM E8 / E8M-15a (2015). Standard Test Methods for Tension Testing of Metallic Materials. ASTM International, West Conshohocken, **DOI:10.1520/E0008_E0008M-15A**.

[13] Hollomon, J.H. (1945). Tensile deformation. *Transactions of the Metallurgical Society of AIME*, vol. 162, p. 268-290.

[14] Dieter, G.E. (1928). *Mechanical Metallurgy*, McGraw- Hill book co., Singapore.

[15] Gautam, S.S., Dixit, P.M. (2010). Ductile failure simulation in spherodized steel using a continuum damage mechanics coupled finite element formulation. *International Journal of Computational Methods*, vol. 7, no. 2, p. 319-348, **DOI:10.1142/S0219876210002180**.

[16] Ajit, K.P., Gautam, A., Sarkar, P.K. (2015). Ductile fracture behavior of low carbon high strength steel using continuum damage mechanics. *International Journal of Materials Research*, vol. 106, no. 6, p. 1110-1113, **DOI:10.3139/146.111271**.

Strojniški vestnik - Journal of Mechanical Engineering 62(2016)5, 307-317
DOI:10.5545/sv-jme.2015.3234
Original Scientific Paper
Received for review: 2015-11-24
Received revised form: 2016-03-08
Accepted for publication: 2016-03-21

Using Newton's Method to Model the Spatial Light Distribution of an LED with Attached Secondary Optics

David Kaljun[1,*] – Jože Petrišič[1] – Janez Žerovnik[1,2]
[1]University of Ljubljana, Faculty of Mechanical Engineering, Slovenia
[2]Institute of Mathematics, Physics and Mechanics, Slovenia

In the design of optical systems based on light emitting diode (LED) technology, a crucial task is to handle the unstructured data describing the properties of optical elements in standard formats. This leads to the problem of data fitting within an appropriate model. Newton's method is used as an upgrade of the previously developed most promising discrete optimization heuristics showing an improvement in both performance and the quality of solutions. This experiment also indicates that a combination of an algorithm that finds promising initial solutions as a preprocessor and Newton's method may be a winning idea, at least on some datasets of instances.
Keywords: least squares function fitting, Newton's method, discrete optimization, local search, light distribution, LED

Highlights
- *Model for data fitting of LED photometry with the evaluation function is presented.*
- *The effects of a numerical method in conjunction with heuristics are studied.*
- *Algorithms are developed with the use of C++ programing language.*
- *The success of developed algorithms is tested on real and artificial datasets.*
- *The results are statistically evaluated.*
- *The numerical Newton's method prevails on both datasets, and provides substantial runtime shortening.*

0 INTRODUCTION

The light emitting diode (LED) industry has been evolving rapidly over the past several years. The fast pace of research and development in the field has had a number of impacts. One of the results is the massive use and implementation of LED elements in all kind of luminaires. While some of these luminaires are designed for ambient illumination, the majority are technical luminaires that have to conform not only to electrical and mechanical safety regulations but also to regulations that define and restrict the photometry of a certain luminaire. This means that the photometry of a luminaire has to be defined prior to production. In order to do that efficiently and with minimal errors the design engineer must virtually test the luminaires performance. Tools that can be used for this (OpticsWorks **[1]**, LigthTools **[2]**, TracePRO **[3]**) do exist and they offer a vast repository of sub-modules to develop and design custom lenses, reflectors, light guides, etc. However, these universal tools do not completely exploit the luminaire design possibilities that were introduced by the transition from conventional light source technologies to LED. One of the possibilities, which is also the main aim of a larger study that incorporates the research presented here, is to have an expert or intelligent system that would be capable of suggesting a secondary lens combination that would result in a user defined end photometry. In other words, the system would take some stock secondary LED lenses from different manufactures, place them on a defined LED array and search for the optimal combination of the lenses so that the resulting photometry would be as close as possible to the user defined one.

The method could enable the luminaire designer to custom design the light engine to a specific area of illumination, while keeping the mechanical and electrical parts of a luminaire untouched. This would in turn provide a customer with a tailored solution that would guarantee maximum efficiency, lower prices, less light pollution and the possibility of individualizing the illumination effect while maintaining a consistent visual appearance of the luminaries. There are several optimization tasks related to the development of the above idea.

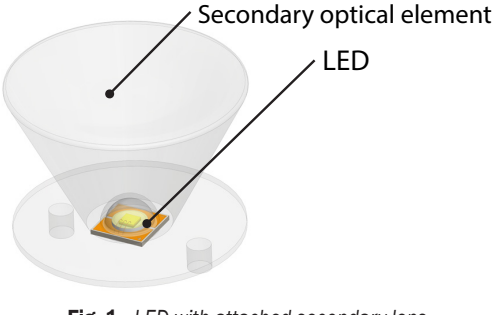

Fig. 1. *LED with attached secondary lens*

*Corr. Author's Address: University of Ljubljana, Faculty of Mechanical Engineering, Aškerčeva 6, 1000 Ljubljana, Slovenia, david.kaljun@fs.uni-lj.si

Here we focus on the approximation of spatial light distribution with a moderate number of suitable basis functions ([4] and [5]). The problem that is defined formally in the next section is motivated by the following. The data describing the properties of the lenses and/or of the desired light distribution is nowadays usually given in some standard format files that correspond to the measured (or desired) values at a number of points in space. This results in relatively large data files of unstructured data. Clearly, if the data can be well enough approximated i.e. as a linear combination of certain basis functions, this may enable faster computations using less computer storage. Indeed, for some special cases including LED lenses with symmetric light distribution, it is possible to find reasonably good approximations quickly (8 minutes' runtime on an Intel Core I7-4790K CPU @ 4 Ghz, the code is written in C++ and is not fully optimized). Sufficiently good approximation here means 2 % to 5 % *RMS* error (to be defined later) for target light distribution, taking into account expected noise in measurement using current technology. Recent experiments show that sufficiently good approximations can be obtained using some basic optimization algorithms, including local search algorithms and genetic algorithms ([6] to [8]). However, when using predefined lenses to design a luminaire that closely approximates a desired light distribution, it may be necessary for the approximation error to be much lower. The same task can also be seen as solving a problem of data compression, replacing a long unstructured data file with a much shorter one, in this case a sequence of parameters. It makes sense to aim at 0 % approximation when considering the data compression task. As the functions to be approximated are smooth, it is natural to try to improve the basic discrete optimization methods with continuous optimization techniques, i.e. Newton's method [9]. Here we consider Newton's method both as a standalone (restarted) algorithm and as a post-processor of other algorithms. The datasets used for testing and analysis are a selection of real lenses as used in previous studies and an artificial dataset that is large enough for statistical analysis. The artificial dataset is also generated in a way which assures that 0 % approximation is possible. Note that we have no guarantee that the realistic lenses can be approximated within our model with an arbitrary low *RMS* error. The rest of the paper is organized as follows: in Section Two we discuss the problem and present the mathematical model, Section Three is all about the algorithms and Newton's method implementation, Section Four presents the datasets used in the experiment, Section Five provides the experiment set-up, Section Six unveils the results, and Section Seven wraps everything up in the conclusion. The Appendix provides some formal details related to the application of Newton's method.

1 THE MODEL

The method mentioned above seems natural and straightforward, but looking closer, we observe some fundamental problems related to the realization of the main idea. Namely, both the spatial light distribution of LED lenses and the desired illumination are given in the standard data formats, which are just long unstructured lists of data. In particular, when the aim is to construct a lighting system that provides the desired illumination of the environment, it is necessary or at least very convenient to have the data in some more structured format. It is known that the spatial light distribution of some LED lenses can be approximated by the sum of a small number of certain basis functions [4]. Provided the approximation is sufficiently good, it may be possible to provide designs combining several lenses with a controlled error rate. This naturally opens several research avenues. For example, it is important to have error free or at least very good approximations of the basic lenses, and to have methods that are stable, in the sense that they are not too sensitive to the noise in the presentation of basic elements. Here we focus on the first abovementioned task, approximation of the unstructured spatial light distribution data. We search for an approximation of the Luminous intensity $I(\Phi, \boldsymbol{a}, \boldsymbol{b}, \boldsymbol{c})$ at the polar angle of Φ in the form:

$$I\left(\Phi, \boldsymbol{a}, \boldsymbol{b}, \boldsymbol{c}\right) = I_{max} \sum_{k=1}^{K} a_k cos^{c_k}\left(\Phi - b_k\right), \qquad (1)$$

where K is the number of functions to sum and a_k, b_k, c_k are the function coefficients that we search for. For brevity, coefficients are written as vectors $\boldsymbol{a}=(a_1, a_2, ..., a_K)$, $\boldsymbol{b}=(b_1, b_2, ..., b_K)$, $\boldsymbol{c}=(c_1, c_2, ..., c_K)$. The interval range of the coefficients is: $a=[0,1]$, $b=[-90,90]$, $c=[0,100]$. Discrete optimization algorithms will work on the finite subsets where the possible values will be: $\boldsymbol{a}_* \in \{0, 0.001, 0.002, ..., 1\}$, $\boldsymbol{b}_* \in \{-90, 89.9, 89.8, ..., 90\}$, $\boldsymbol{c}_* \in \{0, 1, 2, ..., 100\}$.

Here we need to note two restrictions on the model. The first restriction emerges from the LEDs physical design. LED's cannot emit any light to the back side which is the upper hemisphere in our case. That is why all intermediate values that are calculated at the combined angle $(\Phi - b_k)$ greater than 90° equal 0. The second restriction deals with the

slightly unusual description of the light distribution in standard files such as Elumdat (file extension .ldt) [10] and IESNA (.ies) [11]. These files at present provide measured candela values per angle Φ on so called C planes which can be observed on Fig. 2. One C plane is actually only one half of the corresponding cross-section and does not describe the other half. But from a physical point of view we need to consider the impact from the other half of the cross-section.

Taking into account that all lenses used here are symmetric, we can simplify the calculation of the intermediate values and incorporate the impact of the other half by mirroring (multiplying by –1) all values that are calculated with the combined angle $(\Phi - b_k)$ less than 0°. Note however that this only works with symmetrical distributions, and should be reconsidered carefully when the method is to be applied to asymmetrical distributions.

The goodness of fit is defined as the root mean square error, formally defined by the expression:

$$RMS(\boldsymbol{a},\boldsymbol{b},\boldsymbol{c}) = \sqrt{\frac{1}{N}\sum_{i=1}^{N}\left[I_m(\Phi_i) - I(\Phi_i,\boldsymbol{a},\boldsymbol{b},\boldsymbol{c})\right]^2}, \quad (2)$$

where N is the number of measured points in the input data, $I_m(\Phi_i)$ the measured Luminous intensity value at the polar angle Φ_i from the input data, and $I(\Phi_i, \boldsymbol{a}, \boldsymbol{b}, \boldsymbol{c})$ the calculated Luminous intensity value at the given polar angle Φ_i *RMS* represents the error of the approximation. Later in tables we provide the relative *RMS* error (*RMSp*) defined by Eq. (2a).

$$RMSp(\boldsymbol{a},\boldsymbol{b},\boldsymbol{c}) = \frac{100 \times N \times RMS(\boldsymbol{a},\boldsymbol{b},\boldsymbol{c})}{\sum_{i=1}^{N}\left[I_m(\Phi_i)\right]}[\%]. \quad (2a)$$

Remark. The model was successfully applied to LED's with attached secondary optics and symmetric light distribution [4] showing that sufficiently good approximations (*RMS* error below 5 %) can be obtained using a sum of only three functions, $K = 3$. Approximation of spatial light distribution of a LED with uniform distribution and without a secondary lens using this type of functions was first proposed in [5]. The model was slightly modified in [4] where a new normalizing parameter was introduced and, consequently, all other parameters will have values at fixed intervals known in advance. It should be noted that the modified model is equivalent to the original, only the number of parameters and their meaning differ. It is interesting to note that due to the symmetries in the examples, $K = 3$ is sufficient for both applications ([4] and [5]). In the general case, we expect that $K > 3$ functions will be needed for sufficiently good approximations, and in view of the optimization of the design of a luminaire it is interesting to have an idea how large the parameter K can grow to assure that the light distribution fits the desired (and/or standard) sufficiently well. We do not address this question here.

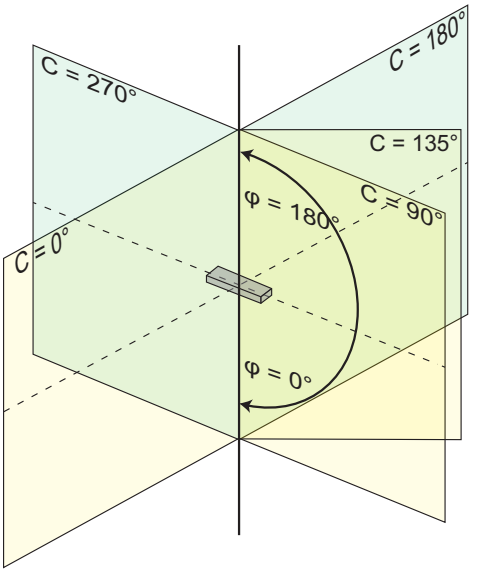

Fig. 2. *C-planes according to standard; C-planes angles: 0° to 360° | Φ angles: 0° to 180°*

When applying the model to the data compression problem, the target *RMS* error is 0 %. Therefore, we aim to improve the approximation results that were obtained previously ([6] and [7]) and restrict attention to the symmetric light distributions. We also fix $K = 3$ functions in the model. Besides the dataset of 14 realistic lenses that was used in some previous studies, here we also generate an artificial dataset in which a sample is simply a sum of three basis functions with randomly chosen parameters. This assures that a zero error approximation is possible for the instances of the artificial dataset. We are interested first in minimizing the approximation error and second in the computational time of the methods. In the next section we briefly outline the algorithms we use in the experiments.

2 THE ALGORITHMS

In previous work ([6] and [7]), the model described above was applied in conjunction with several custom built algorithms that are based on local search heuristics and some meta-heuristics. The algorithms implemented include a steepest descend algorithm, two iterative improvement algorithms with

different neighborhoods, and two genetic algorithms, a standard one and a hybrid one in which the best individuals of every generation are optimized with the iterative improvement algorithm. For a more detailed description of the algorithms we refer to ([6] and [7]). The results of the experiments showed that all of the algorithms applied are capable of providing satisfactory results on all tested instances, and differed mainly in computational time needed. The average *RMS* values obtained on real lenses were around $RMS = 2\,\%$. Hence, the results mentioned proved that the model is accurate and that sufficiently good approximations can be found with a variety of algorithms. However, recall that the model can also be used for data compression task. Zero or very low *RMS* error is also essential in the foreseen application, in which the pre-manufactured lenses are to be combined into a more complex luminaire with prescribed light distribution. In the model we use a sum of functions that are smooth and hence the first and second derivatives can be calculated allowing application of continuous optimization methods, in addition to the general discrete optimization meta-heuristics that were used before. We have chosen to use Newton's (also known as Newton - Raphson) iterative method [9] to find the solution that we seek. It is understood that the convergence of Newton's method largely depends on the initial solution. Therefore, we have applied the method in two ways. First, we use Newton's method as an optimizer which will pinpoint the local minimum of the solutions found by the heuristic algorithms. In a sense this implementation of Newton's method will be an extension of the discrete optimization algorithm, used to finalize the search to end in a local minimum. (Note that the local minima may be missed by the discrete optimization algorithms due to predefined length of the discrete moves.)

Secondly, we use Newton's method as a standalone algorithm that will on initialization generate a number of random (initial) solutions that are uniformly scattered over the whole search space and then the algorithm will use Newton's method on a number of best initial solutions to find the local minima. Of course, for both implementations to be comparable, the iteration count has to be controlled so that the overall maximum amount of computation time will be roughly the same.

Preprocessor multi-start IF. The **multi-start iterative improvement with fixed neighborhood (IF)** algorithm ([7] and [8]) first initializes several initial solutions. The initial solutions are randomly chosen from the whole search space. Each of the initial solutions is then optimized using the following steps. In the beginning the search step values (step for numerical differentiation) $da = 0.01$, $db = 1$ and $dc = I_{max}/10$, are initialized, giving 512 neighbors of the initial solution: ($a_1 \pm da$, $b_1 \pm db$, $c_1 \pm dc$, $a_2 \pm da$, $b_2 \pm db$, $c_2 \pm dc$, $a_3 \pm da$, $b_3 \pm db$, $c_3 \pm dc$).

Then the algorithm randomly chooses a neighbor, and immediately moves to the neighbor if its *RMS* value is better than the current *RMS* value. If no better neighbor is found after 1000 trials, it is assumed that no better neighbor exists. In this case the algorithm morphs the neighborhood by changing the step according to the formula $d_{i+1} = d_i + d_0$. More precisely, $da_{i+1} = da_i + da_0$ where da_0 is the initial step value. Analogously for *db* and *dc*. This is repeated until $i = 10$. If there still is no better solution, the initial step value is multiplied by 0.9 and the search resumes from the current solution with a finer initial step. The algorithm stops when the number of generated solutions reaches T_{max}.

Newton's method. Newton's method ([9], [12] and [13]) is a well-known numerical optimization method that can provide very good results under certain assumptions on the evaluation function and on the initial solution. Newton's method indirectly minimizes the evaluation function by looking for a solution for a system of nonlinear equations (first derivatives of the evaluation function). Newton's method solves the system of nonlinear equations iteratively by approximating it with a system of linear equations in each step which produce the delta vector. The delta vector is a part of the iterative scheme $x_k^{i+1} = x_k^i - d_k^i$. Newton's method converges when the delta vector vanishes, $d = 0$. At this point the evaluation coefficients found are the local minimum. Details are given in the Appendix. An obvious assumption is that the evaluation function has to be a continuous non-linear function for which the first and second order derivatives are defined. The initial solution has to be close enough to a local or global optimum for Newton's method to converge. Hence, the method may be very sensitive to the choice of the initial solution.

3 THE DATASETS

The experimental study uses two batches of instances, a dataset of 14 instances that correspond to real LED lenses and a dataset of artificial instances generated for purpose of this experiment. The artificial lenses are used to obtain more conclusive results on the statistical test, because a sample of 14 is rather small and may provide statistically insignificant results. The

real lenses on the other hand show that the algorithms are useful in real life scenarios.

Real lenses. We have chosen 14 different symmetrical lenses which are meant to be used with a CREE XT-E series LED, from one of the world's leading lens manufacturer LEDIL from Finland. We acquired the photometric data from LEDIL's on-line catalogue [14]. The data was provided in .ies format, which we then converted to a vector list that is more suitable to use in our algorithms. LEDIL measured the individual lenses with a 1° polar precision on four C panels. This means that from every .ies file we extracted 720 vectors. As the lenses are symmetric we only needed one C panel and, because we are only working on the lower half of the sphere (DLOR), we end up with 91 vectors (counting the 0° vector) on which we approximate the model.

Artificial lenses. In the dataset of 100 artificial examples, each element in the dataset was generated as follows.

A value from an interval was generated using uniform random distribution. (Intervals are $[0,1]$, $[0,90]$, or $[0,10]$, depending on the parameter. More precisely, the random generator chose one of the values from the finite sets:

$$a_1, a_2, a_3 \in \{0, 0.001, 0.002, ..., 0.999, 1\},$$
$$b_1, b_2, b_3 \in \{0, 0.01, 0.02, ..., 89.99, 90\},$$
$$c_1, c_2, c_3 \in \{0, 0.1, 0.2, ..., 9.9, 10\}.$$

Then the function values or candela values were computed for each polar angle $\Phi \in \{0, 1, 2, ..., 89\}$. The candela values for polar angles $\Phi \in \{90, 91, 92, ..., 180\}$ were set to 0. The data was then encoded into an .ies file structure, yielding a data file in the same format as the real lenses have. Note that the data generated assure that in each case zero *RMS* error approximation is possible within our model. Second, the dataset of 100 samples is sufficiently large for a meaningful statistical analysis of the experimental results.

4 THE EXPERIMENT SETUP

Before we go ahead and explain the experimental set-up, let us first remember the evaluation function that is the basis of Newton's method [9]. We already showed that the goodness of fit is measured using the *RMS* value that is calculated from Eq. (2). From this we can define the evaluation function as:

$$E(\boldsymbol{a},\boldsymbol{b},\boldsymbol{c}) = \frac{1}{N}\sum_{i=1}^{N}\left[I_{max}\left(G_1(\Phi_i)+G_2(\Phi_i)+G_3(\Phi_i)\right)-I_m(\Phi_i)\right]^2, \quad (3)$$

$$G_k(\Phi) = a_k cos^{c_k}(\Phi - b_k), \quad (4)$$

and

$$RMSp(\boldsymbol{a},\boldsymbol{b},\boldsymbol{c}) = \frac{100\times N\times\sqrt{E(\boldsymbol{a},\boldsymbol{b},\boldsymbol{c})}}{\sum_{i=1}^{N}\left[I_m(\Phi_i)\right]}[\%].$$

Here E represents the error to be minimized, N the number of measured points in the input data, I_{max} the maximum candela value, and $I_m(\Phi_i)$ the measured Luminous intensity value at the polar angle Φ_i from the input data. The experiment was set-up to provide data from different algorithms. This in turn enables an objective comparison and a statistical test to determine the best algorithm. Recall that we implemented Newton's method in two distinct ways. The first implementation uses the multi-start version of iterative improvement (**IF**) to find a good approximation which is then optimized via Newton's method. The second implementation uses the random generator to generate initial solutions of which 100 best are optimized with Newton's method. Table 1 shows different algorithms that were prepared for the experiment. After each run Newton's optimization method is applied.

Table 1. *Experiment algorithms*

	Config.	Algorithm	Multi-start	IF steps
Short runs 1 million	1	S-Newton	1000000	NA
	3	IF10	10	100000
	4	IF20	20	50000
	5	IF50	50	20000
	6	IF100	100	10000
Long runs 4 million	2	L-Newton	4000000	NA
	7	IF40	40	100000
	8	IF80	80	50000
	9	IF200	200	20000
	10	IF400	400	10000

Time. We ran the algorithms for two different lengths of time. The short run evaluates approximately one million possible solutions per instance (lens) in just under 45 s, and the long run approximately four million possible solutions per instance in about 3 minutes on a Core I7 - 4790K CPU. Newton's method took an average of 3 to 4 iterations to converge, which means that the time it took to run Newton's method is negligible in comparison to the time it took the whole algorithm run. Expressed in seconds, the Newton's method took approximately 2×10^{-3} s, opposed to minutes of CPU for the heuristics. In addition to the different time/iteration spans we ran the algorithms on two instance sets.

Datasets. Recall the two datasets of instances explained above, the dataset of 14 real lenses and the dataset of 100 randomly generated artificial instances.

Algorithms. We apply Newton's method both as a standalone algorithm (restarted on a selection of randomly generated initial solutions) and as a final step after discrete local search algorithm (**IF**) outlined above. There are several algorithms that vary in the number of multi-starts (or, equivalently in the length of each local search). Depending on the length (short run, long run) and the number of restarts we denote the algorithms **IF10, IF20, IF50, IF100** and **IF40, IF80, IF200, IF400**. The versions without a local search are denoted by **S-Newton** and **L-Newton** for short and long runs, respectively. See Table 1.

5 EXPERIMENTAL RESULTS

We begin the section with a comparison of the raw experimental data followed by the performance (quality of results) ranking and finish with the results of the Wilcoxon Signed rank test.

Experimental results are given in Figs. 3 to 6 and are summarized in Tables 2 and 3.

Comparison of the algorithms based on raw experimental results. Obviously, the pure multi-start Newton's method is by far the best in artificial instances. On the real lenses, the situation is a bit different. The Iterative improvement on several occasions outperforms Newton's method with random initial solutions. On both datasets, the long run yields

Table 2. *Artificial lenses statistical data in RMSp for short and long runs*

	Alg.	Mean	Std. dev.	Min.	Max.
Short runs 1 million	S-Newton	1.38E–04	8.51E–05	3.51E–05	3.91E–04
	IF10	2.34E+01	3.04E+01	5.81E–05	2.43E+02
	IF20	1.12E+01	1.64E+01	4.96E–05	1.33E+02
	IF50	6.33E+00	9.22E+00	4.13E–05	6.87E+01
	IF100	7.23E–01	2.71E+00	3.49E–05	1.91E+01
Long runs 4 million	L-Newton	1.38E–04	8.51E–05	3.51E–05	3.91E–04
	IF40	1.21E+01	2.54E+01	4.89E–05	2.43E+02
	IF80	1.75E+00	4.30E+00	3.51E–05	1.95E+01
	IF200	4.04E–01	1.96E+00	3.51E–05	1.42E+01
	IF400	6.17E–01	2.41E+00	3.49E–05	1.89E+01

Table 3. *Real lenses statistical data in RMSp for short and long runs*

	Alg.	Mean	Std. dev.	Min.	Max.
Short runs 1 million	S-Newton	5.39E+00	3.74E+00	1.79E+00	1.58E+01
	IF10	3.45E+00	1.52E+00	1.29E+00	5.79E+00
	IF20	8.95E+00	8.30E+00	1.60E+00	3.17E+01
	IF50	6.46E+00	4.78E+00	1.60E+00	2.09E+01
	IF100	4.91E+00	2.46E+00	1.60E+00	9.35E+00
Long runs 4 million	L-Newton	4.61E+00	2.65E+00	1.13E+00	1.03E+01
	IF40	3.20E+00	1.44E+00	1.19E+00	5.79E+00
	IF80	3.13E+00	1.75E+00	6.81E-01	6.33E+00
	IF200	3.56E+00	2.06E+00	1.07E+00	8.02E+00
	IF400	3.90E+00	1.85E+00	1.38E+00	7.56E+00

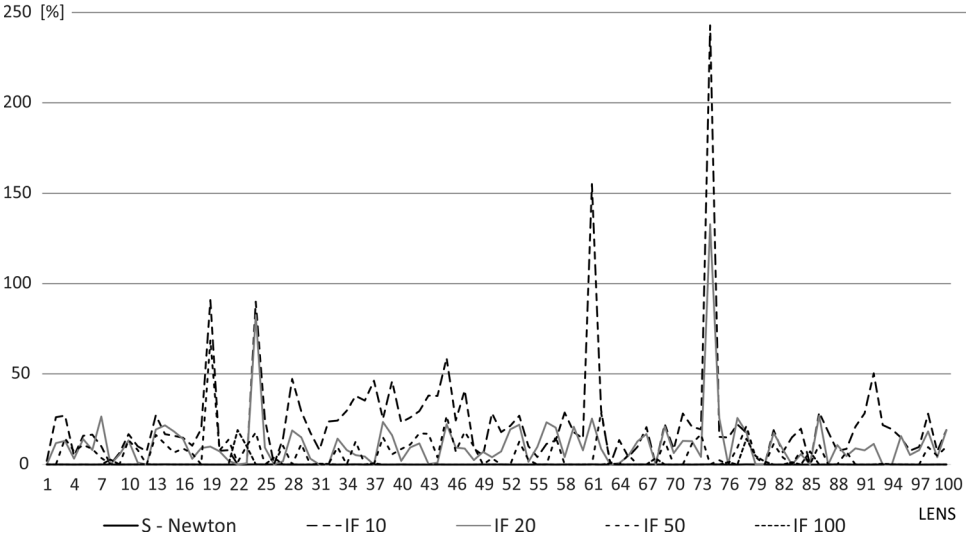

Fig. 3. *Best found solution on a short run; Artificial lenses per algorithm*

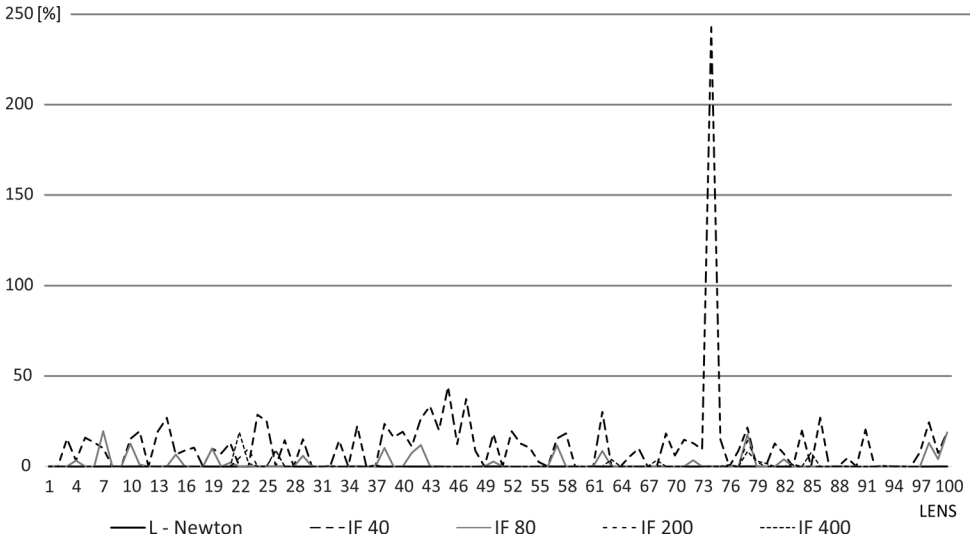

Fig 4. *Best found solution on a long run; Artificial lenses per algorithm*

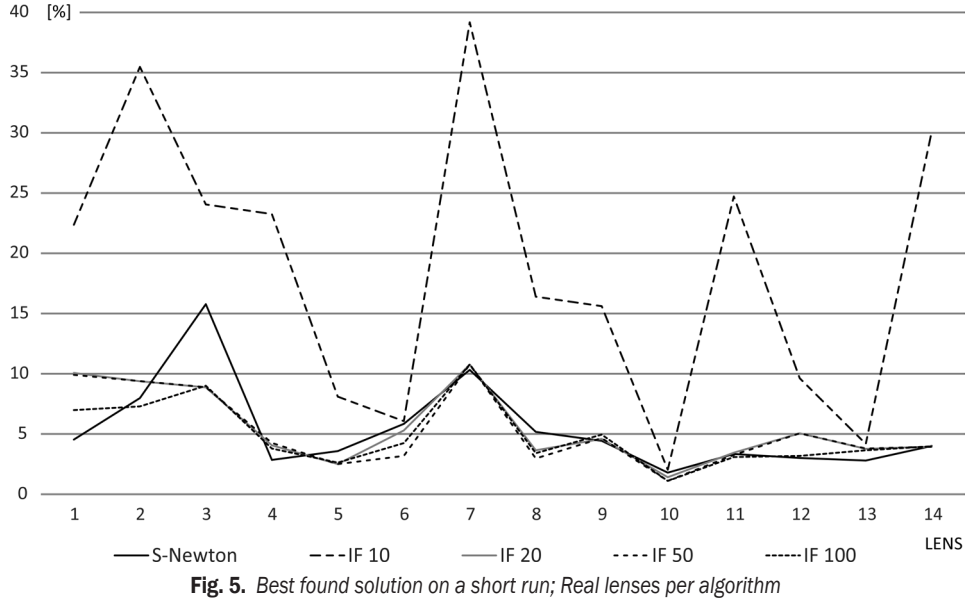

Fig. 5. *Best found solution on a short run; Real lenses per algorithm*

only slightly better results than the short run does (and the short run is executed four times faster). While we have no idea how far from optimal solutions the achieved values are for real lenses, we know that, by construction, a solution with 0 % *RMS* error exists for each of the artificial lenses. Because of that it is worth to note that on the artificial set, the random algorithms found nearly optimal solutions in all cases. The *RMS* errors are in the range of E-04, which still is not pure 0 % *RMS* error, but the very small difference could be due to rounding of the values in the .ies files. On the other hand, we did not find very low *RMS* values on the real set. The values that were found corresponded with the values of previous tests that were performed without any numerical assistance. We did however perform an experiment on the real set with a longer running time, in which we generated 16 million and 64 million initial solutions that showed similar behavior. The mean error and the minimum error over 14 lenses decreased under 3 % and 1.5 % with 16 million generated solutions, and under 2 % and 1 % *RMS* error after 64 million. Recall that 0 % error approximation may not be possible in these instances. While the success of Newton's method on artificial lenses is not surprising, it is not clear why the method is struggling on the realistic dataset. It may be that the

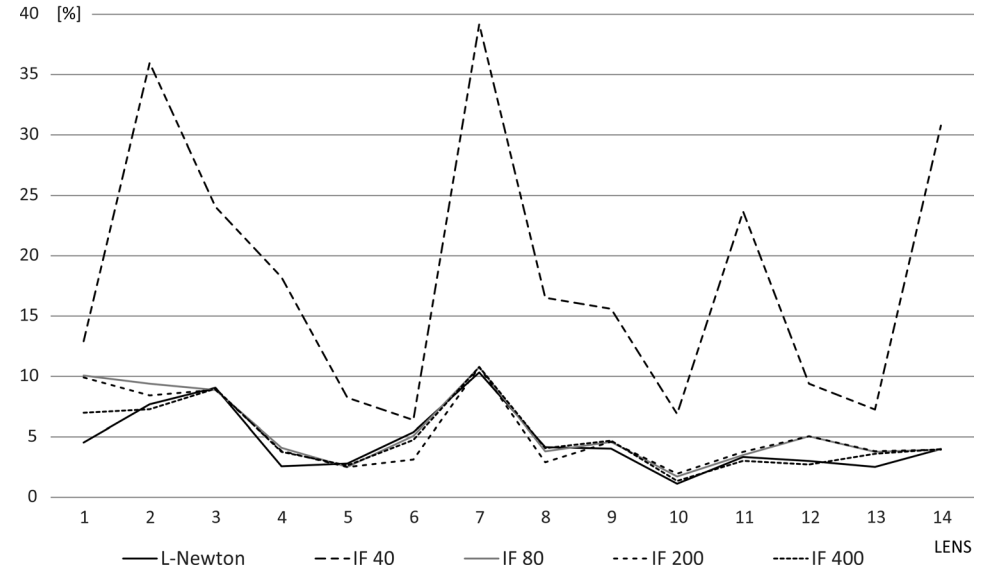

Fig. 6. *Best found solution on a long run; Real lenses per algorithm*

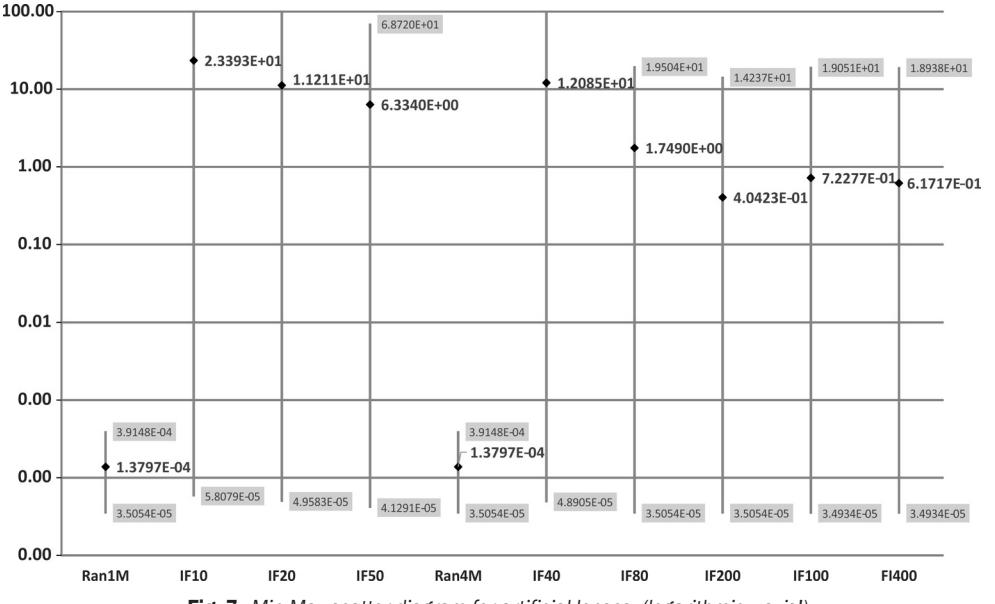

Fig. 7. *Min-Max scatter diagram for artificial lenses; (logarithmic y axis!)*

delta vector was too large due to a bad initial solution. One solution to that problem is the dampened Newton's method, which introduces a dampening factor to vector d to slow down the convergence and allow for more maneuvering space. But as we set out to evaluate the benefits of a standard Newton's method we did not implement any dampening in our algorithms.

The winners in this comparison are the same for both sets, but on the real set the differences between the random Newton and IF assisted Newton algorithms are a lot smaller than on the artificial set, we even see that on some instances the IF algorithms are better. This could be due to the fact that the IF algorithm was previously developed for real lenses that are from a limited range in search space and thus has a slight advantage on the set. The advantage of the pure Newton's method over the artificial dataset can be nicely observed from the data scatter in Fig. 7. We see that the IF algorithms provide a very high degree of data scatter whereas the random ones provide a very narrow result window. This may be due to the

Table 4. *Weighted ranking score of the algorithms*

RANK	Artificial				Real			
	Best		Mean		Best		Mean	
	Alg.	Score	Alg.	Score	Alg.	Score	Alg.	Score
1	L-Newton	944	L-Newton	1000	L-Newton	102	L-Newton	140
2	S-Newton	940	S-Newton	900	IF 100	97	S-Newton	124
3	IF 200	836	IF 20	588	IF 400	96	IF 10	114
4	IF 80	810	IF 100	585	IF 50	94	IF 50	89
5	IF 100	678	IF 10	559	S-Newton	90	IF 20	77
6	IF 400	660	IF 50	538	IF 20	88	IF 100	72
7	IF 50	529	IF 400	385	IF 200	86	IF 40	61
8	IF 40	514	IF 40	358	IF 80	83	IF 80	39
9	IF 20	379	IF 80	304	IF 10	23	IF 400	34
10	IF 10	212	IF 200	283	IF 40	21	IF 200	20

nature of the search because the IF algorithms focus in one defined direction which may not be the best one. Because of that, Newton's optimization cannot escape the potential pitfall of the direction. In contrast, the randomly generated solutions generally find lower quality results, while at the same time providing more maneuvering space for Newton's method to find the best direction on more takes.

A comparison of the algorithms based on weighted ranking. We assign a weight from 1 to 10 to each instance solution per algorithm. If the algorithm found the best solution on an instance it would get the weight 10 and if it found the second best solution it would get the weight 9, and so on until 1 for the worst solution. The total score of the algorithm is the sum of the scores on each instance.

In the same way, we compute the score based on the average values per algorithm and lens. The results are presented in Table 4. Note that the ranking here compares both short and long runs. As expected, Table 4 confirms the superiority of the pure Newton's method with the artificial dataset. However, the situation is much more complicated on the dataset of real lenses. Despite Newton's methods (long and short run) being the two best when considering the average results, they are not both when looking at the best solutions! The long run Newton is still the overall best, but the short run Newton is in fifth place, outrun by two short IF algorithms and one long IF algorithm. We can also observe that the score differences are much smaller on the real set, which indicates that the pure Newton's method is not as superior as it was on the artificial set. The lesser superiority could be explained in part by the fact that the IF algorithms were developed using the real lens set. Hence the IF could have some unexpected advantages. However, Newton's method improves the results in all cases.

Wilcoxon test. The third comparison is based on the statistical paired signed Wilcoxon **[15]** rank test. This statistical test compares algorithms pair by pair to estimate the difference between them. This is done via the asymptotic difference. If the value of the asymptotic difference is lower than 0.05 then the algorithms in the pair significantly differ one from another. The asymptotic differences in the algorithm pairs is presented in Tables 5 to 8.

Table 5. *Asymptotic significances of Wilcoxon Signed rank test for results for short runs on artificial lenses*

algorithm	IF10	IF20	IF50	IF100	S-Newton
IF10		4.078E–11	1.020E–13	1.000E–13	1.000E–13
IF20			7.162E–04	3.120E–13	1.000E–13
IF50				3.628E–06	1.650E–13
IF100					3.234E–08

Table 6. *Asymptotic significances of Wilcoxon Signed rank test for results for long runs on artificial lenses*

algorithm	IF40	IF80	IF200	IF400	L-Newton
IF40		1.736E–11	3.917E–11	7.950E–09	1.899E–12
IF80			3.269E–02	5.563E–01	3.411E–06
IF200				4.818E–06	7.044E–05
IF400					1.176E–08

Table 7. *Asymptotic significances of Wilcoxon Signed rank test for results for short runs on real lenses*

algorithm	IF10	IF20	IF50	IF100	S-Newton
IF10		9.815E–04	9.815E–04	9.815E–04	9.815E–04
IF20			4.326E–01	4.133E–02	5.936E–01
IF50				5.098E–01	9.750E–01
IF100					4.703E–01

Table 8. Asymptotic significances of Wilcoxon Signed rank test for results for long runs on real lenses

algorithm	IF40	IF80	IF200	IF400	L-Newton
IF40		9.815E–04	9.815E–04	9.815E–04	9.815E–04
IF80			5.509E–01	5.553E–02	3.546E–02
IF200				4.703E–01	1.240E–01
IF400					4.703E–01

A look over the Wilcoxon test results reveals that there are mostly no similarities between the algorithms when they ran on the artificial set. We can see that the asymptotic significance values are very low, which means that there are significant differences between algorithms in pairs. We do however have one exception in the pair IF 80 to IF 400, where the asymptotic difference is just over the margin, so we could say that these two have some similarities. The story is completely different on the real dataset, where we can find that most IF algorithms are similar to random algorithms. Thus, based on the statistical test we cannot conclude that either of them is superior. This also corresponds with the findings of the ranking and *RMS* error comparison. The Wilcoxon test provided similar conclusions as the previous tests did, but we need to be careful because the data sets differ in size and the real lenses set can be a bit inconclusive as it is a rather small sample with only 14 instances. That is why the artificial lenses with 100 instances could give a more accurate result.

Table 9. *Real lens RMSp for RAN 4M with and without Newton's method; Quality increase Δ*

Instance	RAN 4M	Newton	Δ [%]
CP12632	27.996	7.6908	72.53
CP12634	45.8986	9.05513	80.27
CP12633	10.7706	2.57185	76.12
CA11934	10.2492	2.7982	72.70
CA11268	15.1818	5.38851	64.51
CP12817	29.6252	10.3279	65.14
CA11265	9.6437	4.1553	56.91
CP12636	7.62895	4.03813	47.07
CA13013	2.70647	1.12548	58.42
FP13030	10.1866	3.34882	67.13
CA11525	12.0224	3.00557	75.00
CA12392	6.87747	2.51916	63.37
CA11483	24.5813	4.0032	83.71

6 CONCLUSION

Here we presented an upgrade of a previously developed most promising discrete optimization heuristics with a continuous optimization method. It was shown that the application of Newton's method led to an improvement of both performance and quality of solutions. In terms of raw performance, we got from the initial 8 minutes' runtime for one algorithm on one lens to an approx. 45 s runtime using the upgraded IF 10 or S-Newton algorithm. The stated runtime is accurate for symmetric lenses and an input of 91 vectors. When working on asymmetric lenses the input will be around 33,000 vectors, and this is when the problem becomes a big data problem. Because of the algorithms' design, the runtime is expected to increase to about 2 hours and 15 minutes. The increase will be by a factor of 180, while the number of vectors is increased by a factor 360. On the asymmetric lenses, the runtime will be lowered from around 24 hours to 2 hours and 15 minutes. Despite the drastic time shortening the quality of the solutions was not worse thanks to Newton's method, which enabled us to find local minimums on the majority of solutions found by the heuristic algorithms. In fact, Newton's method successfully minimized the *RMS* error on all of the experiment cases with the average of 60 % increased quality (minimized *RMS*) over previous experiments done in ([4] and [7]). This can be well observed in Table 9, where we can see the *RMS* error found by the RAN 4M algorithm before the application of Newton's method and after. We can conclude that the integration of a numerical approach with previously developed heuristics significantly improved the application performance to the level at which it is useful in the main research. On the other hand, we have learned that due to the sensitivity of Newton's method to the choice of initial solutions, it may be rewarding to use a preprocessor that may provide promising initial solutions. In particular, on the dataset consisting of real lenses, the experiment showed that the initial solutions provided by a discrete local search algorithm improved the overall performance of the algorithm. This leads to the conclusion that a combination of an algorithm that finds promising initial solutions as a preprocessor to Newton's method may be a winning combination, at least on some datasets of instances. Hence, in a practical application, it may be worth developing good heuristics that may handle specific properties of the instances and thus provide promising initial solutions for final optimization.

7 ACKNOWLEDGEMENT

This work was supported in part by ARRS, the Research agency of Slovenia, grants P1-0285 and ARRS-1000-15-0510. We sincerely thank two

anonymous reviewers for detailed reading of the manuscript and for constructive remarks.

8 REFERENCES

[1] Optis, Optisworks, from *http://bit.ly/1CjKp4t*, accessed: on 2015-06-07.

[2] Lighttools, from *http://optics.synopsys.com/lighttools/*, accessed on 2015-06-07.

[3] Lambardes, Tracepro, from *http://www.lambdares.com/*, accessed on 2015-06-07.

[4] Kaljun, D., Žerovnik, J. (2014). Function fitting the symmetric radiation pattern of a led with attached secondary optic. *Optics Express*, vol. 22, no. 24, p. 29587-29593, **DOI:10.1364/OE.22.029587**.

[5] Moreno, I., Sun, C.-C. (2008). Modeling the radiation pattern of leds. *Optics Express*, vol. 16, no. 3, p. 1808-1819, **DOI:10.1364/OE.16.001808**.

[6] Kaljun, D., Žerovnik, J. (2014). On local search based heuristics for optimization problems. *Croatian Operational Research Review*, vol. 5, no. 2, p. 317-327, **DOI:10.17535/crorr.2014.0016**.

[7] Kaljun, D., Poklukar, D.R., Žerovnik, J. (2015). Heuristics for optimization of led spatial light distribution model. *Informatica*, vol. 39, no. 2, p. 317-327.

[8] Kaljun, D., Žerovnik, J. (2015). Developing led illumination optics design. Papa, G. (ed.), *Advances in Evolutionary Algorithms Research*. Nova Science Publishers, Inc., Hauppauge, p. 11788-3619.

[9] Quarteroni, A., Sacco, R., Saleri, F. (2015). Nonlinear systems and numerical optimization. Marsden, J., Sirovich, L., Antman, S. (eds.), *Numerical Mathematics*. Springer-Verlag GmbH, Heidelberg.

[10] EN 13032-1:2004+a1:2012. *Light and lighting - measurement and presentation of photometric data of lamps and luminaries - part 1: Measurement and file format*. CEN, Brussels.

[11] IESNA, LM-63-02. *Standard file format for the electronic transfer of photometric data and related information*, ANSI, Washington D.C.

[12] Thukral, R. (2008). Introduction to a Newton-type method for solving nonlinear equations. *Applied Mathematical Computation*, vol. 195, p. 663-668, **DOI:10.1016/j.amc.2007.05.013**.

[13] Herceg, D. (2013). Means based modifications of Newton's method for solving nonlinear equations. *Applied Mathematical Computation*, vol. p. 216, 6126-6133.

[14] Ledil oy. (2015). from *http://www.ledil.com/products/?y,* accessed on 2015-06-07.

[15] Wilcoxon F. (1945). Individual comparisons by ranking methods. *Biometrics*, vol. 1, p. 80-83, **DOI:10.2307/3001968**.

[16] Kaljun, D., Petrišič, J., Žerovnik, J. (2016). *Using Newton's method to model a spatial light distribution of a LED with attached secondary optics*, ArXiv:1603.01090.

9 APPENDIX

Jacobian matrix:

$$J(a_1,...,c_3)=\begin{bmatrix} \frac{\partial^2 E(a,b,c)}{\partial a_1 \partial a_1} & \cdots & \frac{\partial^2 E(a,b,c)}{\partial c_3 \partial a_1} \\ \vdots & \ddots & \vdots \\ \frac{\partial^2 E(a,b,c)}{\partial a_1 \partial c_3} & \cdots & \frac{\partial^2 E(a,b,c)}{\partial c_3 \partial c_3} \end{bmatrix}.$$

As the evaluation function is clear enough that it is not difficult to find the first and second derivatives using any of several available systems for symbolic computations, we only present the basic components of Newton's method here. An earlier version of the manuscript with an extended appendix is available at ArXiv **[16]**.

Delta vector:

$$d=\begin{bmatrix} da_1 & da_2 & da_3 & db_1 & db_2 & db_3 & dc_1 & dc_2 & dc_3 \end{bmatrix}.$$

Right side:

$$R(a_1,...,c_3)=\begin{bmatrix} \frac{\partial E(a,b,c)}{\partial a_1} & \cdots & \frac{\partial E(a,b,c)}{\partial c_3} \end{bmatrix}^T.$$

System of equations to solve for d:

$$J(x_i)\times d_i = R(x_i).$$

Coeficient vector:

$$x=\begin{bmatrix} a_1 & a_2 & a_3 & b_1 & b_2 & b_3 & c_1 & c_2 & c_3 \end{bmatrix}.$$

Iterative scheme:

$$x_{i+1}=x_i-d_i.$$

Strojniški vestnik - Journal of Mechanical Engineering 62(2016)5, 318-328

DOI:10.5545/sv-jme.2015.3339 Original Scientific Paper
Received for review: 2015-12-26
Received revised form: 2016-03-03
Accepted for publication: 2016-03-21

Study on the Performance and Control of a Piezo-Actuated Nozzle-Flapper Valve with an Isothermal Chamber

Mohammadreza Kamali[1,*] – Seyed Ali Jazayeri[1] –Farid Najafi[2] – Kenji Kawashima[3]– Toshiharu Kagawa[4]

[1] K. N. Toosi University of Technology, Faculty of Mechanical Engineering, Iran
[2] University of Guilan, Engineering Faculty, Iran
[3] Tokyo Medical and Dental University, Institute of Biomaterials and Bioengineering, Japan
[4] Tokyo Institute of Technology, Japan

A new integrated nozzle-flapper valve equipped with a piezoelectric actuator and an isothermal chamber has been developed and studied in detail. The designed single stage valve controls the pressure and flow rate simply, effectively, and separately. This idea can easily be used in the pilot stage of a two-stage valve as well. Application of isothermal condition in the valve load chamber eliminates the dynamic malfunction that may persist from temperature variation within the valve load chamber; consequently, the governing equations for the prediction of pressure dynamics in the chamber are much more accurate and simpler. The valve has been equipped with a stacked type piezoelectric actuator which has a unique behaviour. Furthermore, stiffness, in the selected actuator, is enhanced against the thrust of the discharging flow from the nozzle, thus decreasing the complexity of dynamic equations of the valve. A detail mathematical model and simulation was developed to study the dynamic performance analysis of the proposed valve. An experimental test rig was built to validate the results of simulations. The unique features and performance of the proposed valve were studied thoroughly. The valve's governing equations are nonlinear in nature, and some variables of the equations are a source of some uncertainties; sliding mode approach was used to control the steady and unsteady pressure and output flow rate of the valve.

Keywords: nozzle-flapper (NF) valve, isothermal chamber, piezoelectric actuator, sliding mode approach

Highlights

- *A new nozzle-flapper valve was designed and manufactured.*
- *Its dynamics were improved using an isothermal chamber.*
- *A stacked piezoelectric actuator was utilized to actuate the proposed valve.*
- *A sliding mode approach was used to precisely control the output flow rate or pressure.*

0 INTRODUCTION

Pneumatic actuation systems have been extensively utilized in high technology and complex industries, such as the semiconductor manufacturing process, for precise positioning to isolate vibration. A key element in the pneumatic control system is electro-pneumatic valve which not only converts the electrical signal to pneumatic one but also constructs a close-loop for control system; therefore, its structure and parameters play an important role to reach a necessary performance. Many research works have been conducted to increase the efficiency of pneumatic control systems through improved design and development of pneumatic valves with a new structure and improved dynamic characteristics. A new pneumatic valve that benefits from a piezoelectric actuator was developed to increase dynamic properties and reduce energy consumption **[1]**. In **[2]** a pneumatic positioner with a piezoelectric actuator was modeled, and its advantages were introduced. A pneumatic servo valve driven by a piezoelectric actuator with a simple amplification mechanism was presented in **[3]**. In contrast, some other research works have attempted to attain a reasonable and detailed mathematical model of the valve to optimize the control effort of the pneumatic system. Richer and Hurmuzlu **[4]** developed detailed mathematical models for each element of a pneumatic system to control the output of the actuator accurately. Wang et al. **[5]** made a new model for a nozzle-flapper (NF) valve to decrease the output thrust effect of the nozzle on the flapper. One of the effective structures in control valves is the NF mechanism, which can be used for obtaining quick response and precise control action due to its simple structure with high sensitivity and wide frequency range; many research works are being focused on studying and profiting from its advantages in the new structures of the fluid power valves. Kawashima et al. **[6]** designed and manufactured a new NF valve to minimize noise level and pressure fluctuations in the output flow of the valve. There have also been some research works that studied NF valves numerically to optimize their dimensional features **[7]** or suggested new structures to decrease detrimental effects of the output flow on it **[8]**. The load chamber is one of the main subdivisions of the NF valve, and its dynamics have an important role in the whole dynamic of the

*Corr. Author's Address: K.N.Toosi University of Technology , Vanak Sq., Tehran, Iran, mohammadrkamali@gmail.com

valve. The lack of an accurate model for the state change of air in the load chamber of the NF valve makes the control of the system rather difficult. The state change model of the pressurized air in the load chamber is usually assumed as adiabatic or isothermal [9]. Realization of the isothermal condition in the load chamber makes the mathematical models of the NF valve simpler and improves its heat transfer criteria and dynamic characteristics. Therefore, implementing an isothermal condition in the load chamber of the valve facilitates its control. In other words, through only one pressure sensor, installed on the valve's load chamber, both pressure or flow rate can be controlled more easily [10]. Kawashima et al. [11] proposed a new method to measure the unsteady flow rate of pressurized air using an isothermal chamber. Using benefits of such a chamber, Kawashima et al. [12] presented a system to determine the characteristics of the pneumatic solenoid valves. In the following of [12], Wang et al. [13] developed the same system in a way that it was possible to determine the characteristics for electrically modulated pneumatic control valves using an isothermal chamber.

Traditional NF valves use electromagnetic transducers to drive the flapper. However, this has shortcoming such as large dimensions, high electrical power consumption, slow response and susceptible to electromagnetic interference [3]. The most effective actuator that can overcome these limitations is a piezoelectric actuator. The unique properties of piezoelectric actuator make it the most appropriate choice for cases such as hazardous and sensitive industrial or medical environments. Piezoelectric actuators have much less electrical energy consumption along with much faster response time; also, the mechanism is spark- and magnetic-field free. These unique properties have made it much more applicable to be used as an actuator in pneumatic valves [1] to [3]. Furthermore, the stacked type of piezoelectric actuator simplifies the mathematical model of the valve due to its sturdy construction [5].

In this study, a detailed description of a new NF mechanism with isothermal load chamber and piezoelectric actuator is introduced. The proposed valve profits from both the isothermal load chamber and the piezoelectric actuator to simply, precisely, and effectively control the pressure or flow rate of the air without any concerns that may exist even in hazardous industrial environments. The theoretical analysis of the valve was developed to derive a more precise mathematical and simulation model. The static and dynamic performance of the proposed valve was assessed experimentally in order to validate the developed model and to highlight the advantages of the proposed valve. Due to the nonlinear behaviour of the proposed valve and existence of uncertainties in some variables of the valve's equations, sliding mode approaches have been designed and implemented to control the output flow rate and pressure of the proposed valve more precisely. Experimental data showed the effectiveness of the new NF valve; extended measurements were also carried out using steady and unsteady oscillatory output flow rate or pressure of the valve to prove its effectiveness.

1 PROPOSED VALVE

1.1 NF Mechanism

A schematic drawing of the proposed NF system is shown in Fig. 1, which consists of two fixed flow restrictors ((a) and (f)), a nozzle (d), a load chamber (c), and a piezoelectric actuator set that moves a flapper (e). Pressure-regulated air is delivered to orifice (a) and the variable flow restrictor (d) connected in series. The variable flow restrictor is made possible by moving the flapper that changes the distance X_n between the nozzle head and the flapper. The flow rate through the nozzle and output orifice (f) is controlled by the distance between the flapper and nozzle. This would cause pressure changes of p_b in the load chamber, which is usually referred as nozzle back-pressure.

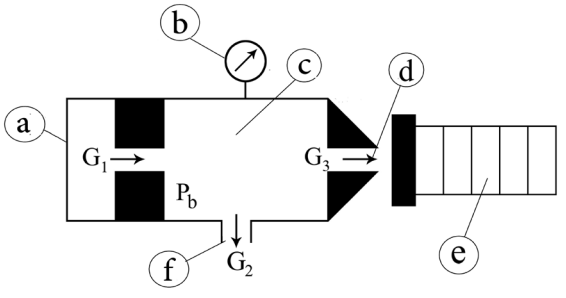

Fig. 1. *Layout of the proposed NF system; (a) input orifice, (b) pressure sensor, (c) isothermal load chamber, (d) nozzle, (e) piezoelectric actuator and flapper, (f) output orifice*

To realize the isothermal condition in the load chamber (c) of the proposed valve, thin copper wires are inserted into the load chamber, which is specially designed and manufactured for the NF system [10]. Copper wires not only decrease the effective volume of the control chamber but also improve heat transfer conditions within the chamber. Copper wires absorb the heat generated during the compressing and filling process of air far more effectively. Several studies

have proved the effectiveness of such systems in their research [10] to [13].

When pressurized air is ejected from the nozzle, flow force is exerted on the flapper. Wang et al. studied flow force effects on the moving flapper that improve the control performance, but dynamic analysis of a standard NF valve is far more complicated [5]. In proposed piezoelectric actuator, the flapper becomes sturdier by the flow forces so that there is no need to model its displacement in dynamic equations.

1.2 Piezoelectric Actuator

Piezoelectric actuators convert electrical energy directly into mechanical energy. There are no moving parts to limit their resolution and mechanical performance. As shown in Fig. 2, there are two major types of piezoelectric actuator arrangements. These are either bending transducer or stacking transducer [14].

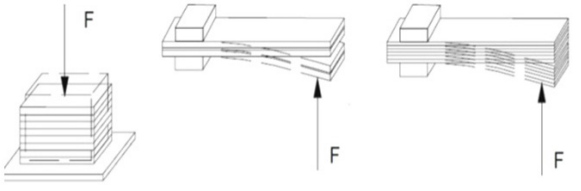

Fig. 2. *Different piezoelectric actuators, stacked and bending transducer*

Figs. 3 and 4 illustrate a typical hysteresis characteristic of stacked and bending piezoelectric transducer, respectively. The rigidity of stacked piezoelectric actuator improves the hysteresis criteria and, due to lower deflection, the control pressure that is produced within the load chamber of NF mechanisms for the same supply pressure will be much higher.

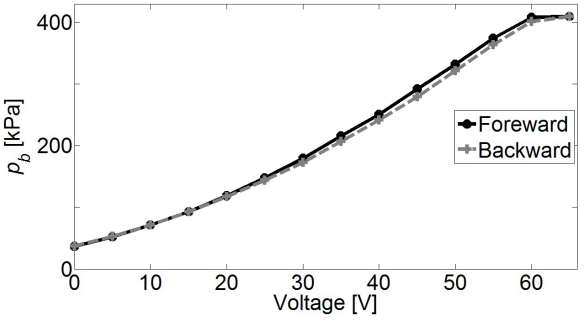

Fig. 3. *Hysteresis behaviour of stacked type piezoelectric actuator*

Faster response is one of the main characteristic features of stacked type piezoelectric actuators. This characteristic is especially advantageous in actuating pneumatic valves. The stacked type piezoelectric actuator utilized in the proposed valve can reach its nominal displacement in approximately one third of the period at the resonant frequency, based on its specification in [15], which was also verified here.

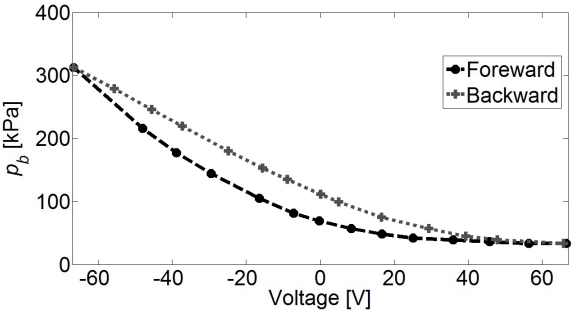

Fig. 4. *Hysteresis behaviour of bending-type piezoelectric actuator*

The dynamic behaviour of a flapper equipped with a piezoelectric actuator, which has a very fast response, has a minor effect on the overall dynamic response of the NF mechanism; therefore, the dynamics of the flapper can be neglected.

1.3 Dynamic Model of an NF Mechanism with Isothermal Load Chamber

Using state equation for pressurized air within the load chamber is shown in Fig. 1

$$p_b = \frac{R\theta_b}{V} W, \tag{1}$$

where p_b denotes the load chamber's absolute pressure, R is the gas constant, θ_b is the load chamber temperature, W is mass of the air in the load chamber and V denotes the load chamber volume. Differentiating above equation with respect to time t:

$$\frac{dp_b}{dt} = \frac{R\theta_b}{V} \cdot \frac{dW}{dt} + \frac{RW}{V} \cdot \frac{d\theta_b}{dt}. \tag{2}$$

Using continuity equation for air in the load chamber:

$$\frac{dW}{dt} = G_1 - G_2 - G_3, \tag{3}$$

where, G is mass flow rate through orifices. Using above governing equations:

$$\frac{dp_b}{dt} = \frac{R\theta_b}{V} . \left(G_1 - G_2 - G_3\right) + \frac{RW}{V} . \frac{d\theta_b}{dt}. \tag{4}$$

Since during charge and discharge, the state of air in the load chamber is assumed to be isothermal, the above equation can be simplified:

$$\frac{dp_b}{dt} = \frac{R\theta_b}{V}.\left(G_1 - G_2 - G_3\right). \quad (5)$$

For the isothermal chamber, the average temperature is assumed to be equal to the room temperature [10]. It is concluded from Eq. (5) that for a fixed chamber volume of V and the room temperature of θ_b, an instantaneous desired mass flow rate G_2 could be produced by controlling solely the pressure changes. The mass flow rate G is easily converted to volumetric flow rate Q under standard conditions:

$$Q = G / \rho, \quad (6)$$

where ρ is pressurized air density.

The compressed air flow rate through fixed or variable orifices could be either sonic or subsonic depending upon the upstream/downstream pressure ratio [16]. The mass flow rate through a restriction is a function of geometric parameters, the upstream and downstream pressures. Therefore, mass flow rates, G_1, G_2, and G_3 are calculated as follows:

$$G = \begin{cases} \rho_0 C p_1 \sqrt{\dfrac{293}{\theta_1}} & ; \text{ if } \dfrac{p_2}{p_1} \le b \\ \rho_0 C p_1 \sqrt{\dfrac{293}{\theta_1}} . \sqrt{1 - \left[\dfrac{\dfrac{p_2}{p_1} - 1}{b - 1}\right]^2} & ; \text{ if } \dfrac{p_2}{p_1} > b \end{cases}, \quad (7)$$

where coefficient C is the sonic conductance, which represents the flow's passing ability, and is represented by $C = S_e / 5$ where S_e is effective area of orifices or nozzle and b is the critical pressure ratio. If G is calculated for input orifice then $p_1 = p_s$ and $p_2 = p_b$, but if G is calculated for output orifice and nozzle then $p_1 = p_b$ and $p_2 = p_a$.

1.4 Simulation Program

A simulation model based on the above analysis is established and shown in Fig. 5. The input is the flapper displacement of X_n, while the outputs are the control pressure p_b, and the flow rate Q. According to the reasoning mentioned earlier, the dynamic response of the piezoelectric actuator has a minor effect and is not taken into account.

To validate the valve performance and developed model, a MATLAB/SIMULINK model of the system as shown in Fig. 5 was constructed. Some experiments were carried out to determine the parameters of the developed model, which included the effective area coefficients of the orifices and nozzle, as well as the critical pressure ratio. Through comparison of simulation results and experimental data, the selected mentioned parameters are optimized. The effective area coefficients of the NF valve were chosen as 0.86 for input and output orifices and 1.0 for the variable orifice. The best critical pressure for designed structure is derived to be 0.53.

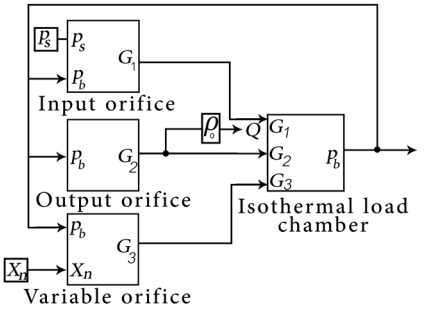

Fig. 5. *Simulation model for the proposed valve*

1.5 Experimental Setup and Results

An experimental test rig, shown in Fig. 6 for NF mechanism was designed and manufactured to validate the developed simulation model and prove the effectiveness of the proposed valve.

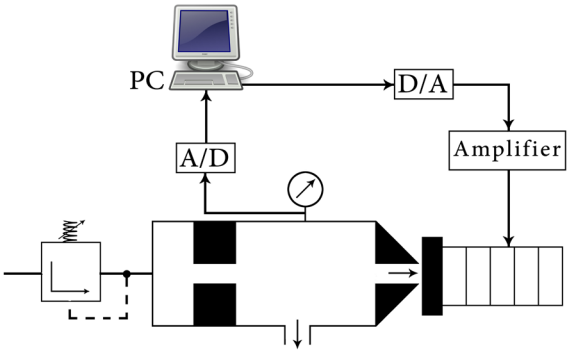

Fig. 6. *Developed NF mechanism layout*

Table 1. *Main parameters of the valve*

Symbol	Description	Value
D_{oi}	Diameter of the input orifice	0.4 mm
D_{oo}	Diameter of the output orifice	0.3 mm
V	Volume of the load chamber	0.7 cm^3
X_n	Displacement domain of the piezoelectric actuator	0 mm to 0.09 mm
b	Critical pressure ratio	0.53

A pressure regulator was used to stabilize the air supply. Stabilized air is fed to the proposed valve through the input orifice. The dimensions of the main subdivisions of the proposed valve have been presented in Table 1. They were estimated using the simulation model before manufacturing the proposed valve and were estimated based on required output flow rate and dynamic behaviour.

The load chamber of the valve was filled with copper wire of 50×10^{-3} cm diameter. Compact mass density was greater than 300 kg·m^{-3}. These circumstances fulfil the isothermal condition in the load chamber [10]. The utilized piezoelectric actuator in the proposed valve is specified with part number P-841.6 and is produced by Physik Instrumente. The control approach was developed and implemented in a MATLAB/SIMULINK environment. Digitally generated control signals using a MATLAB/Real-Time Workshop environment with a CSI-360116 data acquisition board (made by Interface) were used to drive the piezoelectric actuator through a power amplifier. A semi-conductive-type pressure sensor was used to measure the pressure of the isothermal chamber. The output flow rate is derived from Eq. (3) by differentiating the pressure; five sets of data were used for this purpose. A low-pass filter was used to smooth out the pressure curve. The cut-off frequency of the filter was 2.5 times greater than that of the input frequency. Tests were performed at a constant ambient temperature of 20 °C and supply air pressure of 400 kPa.

1.5.1 Results to Compare Isothermal and Conventional Settings

Initially, some tests were carried out to show the effectiveness of the suggested isothermal chamber in comparison to the conventional chamber, which is a chamber without any metal wool for the setup, even though many previous studies had already shown its effectiveness [10] to [13]. The chamber volume was selected as 29.5 cm³.

The isothermal chamber temperature fluctuation is shown in Fig. 7 for simulation results and experimental data. The input voltage to the piezoelectric actuator was $[45-44.5\times\sin(2\pi f\cdot t)]\,V$. Using the stop method [11], the average temperature in the chamber was measured. The ambient temperature was 293 K in the test room. The frequency was 20 Hz. The experimental data are shown by dark points, and the solid line represents the simulation results. The temperature deviation is about 2 K, which suggests that isothermal condition by metal wool in the chamber is well established.

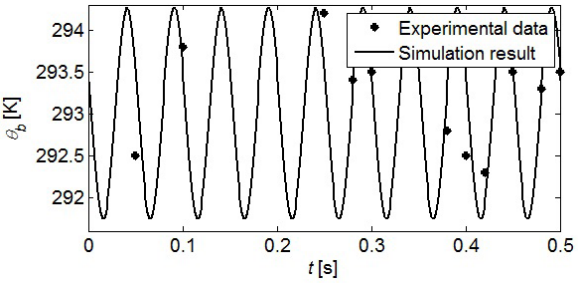

Fig. 7. *Temperature variation in the valve load chamber*

The step response of isothermal and conventional chambers is shown in Fig. 8. Initially, the distance between the flapper and head of the nozzle was at the upper limit and suddenly was reduced to zero. The response for isothermal chamber became faster due to both volume decrease and heat transfer effects. The pressure drop at the beginning of the figure in the isothermal case is due to utilization of copper wire in the load chamber.

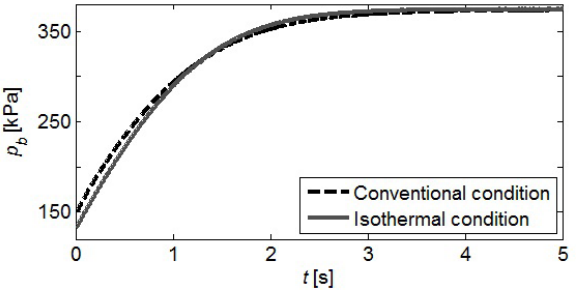

Fig. 8. *Step response of both isothermal and conventional chambers*

In [11], for unsteady flow rate generation, the advantages of the isothermal chamber over the conventional chamber were well defined. According to the presented experimental data and simulation results, when the unsteady flow rate is generated by the pressure change with the conventional chamber, not only the gain but also the phase shows far larger errors, so it makes the control of the proposed valve more difficult; the control effort is also much higher. In the case of the isothermal chamber, the generated unsteady flow rate from the pressure change shows negligible error in the gain, and there is no phase delay. So the effectiveness of the isothermal chamber on the unsteady oscillatory flow generation is evident.

1.5.2 Performance of the Proposed Valve

For the proposed valve, the static behaviour of the simulation model and experimental data are shown in Fig. 9. The steady- state control pressure p_b was plotted against the input displacement of the flapper X_n. Using the laser displacement measurement unit Acuity AR700-0125, X_n was measured precisely. Excellent agreement between simulation model and experimental data is observed despite some small differences which are thought to be due to the uncertainty in the volume of the load chamber and measurement of ambient temperature θ_b. There is almost a linear relationship between the input displacement and steady state pressure of the load chamber when X_n varies within the small range of 0.018 mm to 0.075 mm displacement.

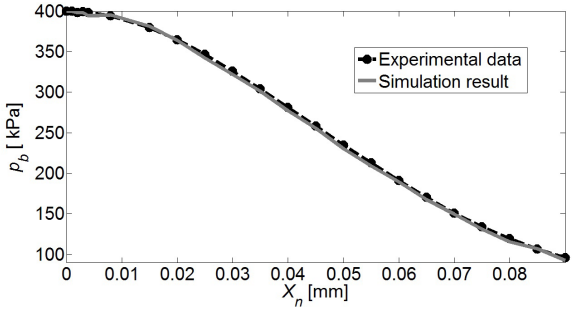

Fig. 9. *Static behaviour of the valve compared with simulation model*

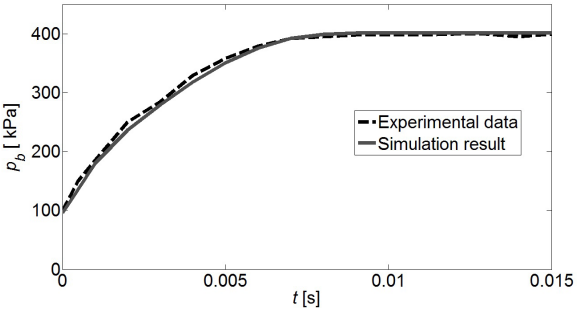

Fig. 10. *Step response of the proposed valve*

The dynamic response of the proposed valve is analysed using step and frequency responses. As illustrated in Fig. 10, the step response of the isothermal chamber for the proposed valve validates the mathematical model and simulation results. From Fig. 10, it can easily be concluded that there is no significant delay in pressure response of the proposed valve. The response time of the designed valve is about 2.5 ms, so the proposed valve can be classified as a fast switching valve. Therefore, it can be employed as a pilot stage for much bigger pneumatic valves. Fast response without any notable delay is a result of the utilization of piezoelectric actuator to actuate the valve, as was predicted in **[2]** and **[3]**. In this case, the maximum error between the simulation result and experimental data is only about 2 %.

Another way to assess the compliance between the simulation model and experimental data is through sinusoidal inputs. When the flapper is excited to move in in a sinusoidal form, experimental data and simulation results are in good agreement at different frequencies. The experiments were performed for wide frequencies, ranging from 0.1 Hz to 100 Hz, and it is concluded that for all frequencies, simulation results and experimental data are in very good agreement. For a test result, mathematical models of the proposed valve have been linearized at one operating point, which is p_b = 350 kPa at v = 65 V.

The relevant valve transfer function is **[10]**:

$$\frac{p(s)}{v(s)} = \frac{K_c}{T_c s + 1}, \tag{8}$$

where T_c is the time constant, and K_c is the proportional gain of the pressure response:

$$T_c = \frac{V}{aR\theta_a}, \tag{9}$$

where a is the flow rate gain with respect to load chamber pressure.

A sinusoidal input signal with amplitude voltage of 5 V and biased input voltage of 65 V was put to the valve at various frequencies. The frequency characteristics of the valve's pressure response were analysed with a Bode diagram as shown in Fig. 11. The bandwidth for the proposed valve with isothermal load chamber is about 50 Hz.

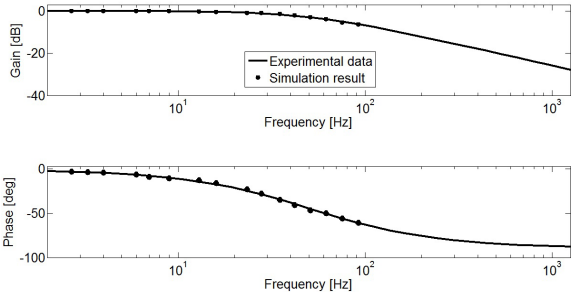

Fig. 11. *Frequency response of the proposed valve, magnitude is normalized by static gain*

Studying existing pneumatic control system having actuators with slow response (≈20 Hz) reveals the importance of the proposed NF mechanism with suitable responses.

2 DESIGN OF THE CONTROLLER FOR THE PROPOSED VALVE

The governing equations of the designed valve are highly nonlinear and contain some parametric uncertainties. Use of nonlinear control criteria would give a far more precise control of the desired output flow rate or pressure. One of the well-known effective nonlinear robust control approaches is sliding mode control [17] and [18]. Primarily, a sliding mode controller was designed to control the output flow rate and pressure in the load chamber. The sliding mode control approach can be used to overcome the significant system nonlinearities initiated during pressure or flow rate control process in the presence of uncertainties. The proposed valve is considered as a single input-single output (SISO) nonlinear system, which can be easily described with the following state-space equation:

$$\dot{p}_b = f_1(p_b) - f_2(p_b) - f_3(p_b)\cdot u, \tag{10}$$

where f_1, f_2 and f_3 are nonlinear mass flow rate functions through the input, output, and variable orifices, respectively. They are also results of product ($R\theta_a/V$) in mass flow rate Eq. (7), for the orifices corresponding to f_i where $i=1,2$ and 3. Variable u is the control input denoted as the distance between nozzle head and flapper X_n.

The main variables that contain uncertainties are volume of the control chamber V and its temperature θ_a. The overestimated variation of the load chamber's volume is about ±5 %. Temperature fluctuation is about ±2 K. The upper and lower bounds of the functions fi are given by:

$$f_{i_{max}} = \frac{R\theta_{amax}}{0.95V_i}\cdot G_i \quad ; \quad i=1,2,3, \tag{11}$$

$$f_{i_{min}} = \frac{R\theta_{amin}}{1.05V_i}\cdot G_i \quad ; \quad i=1,2,3. \tag{12}$$

The control objective is designed to guarantee the state of p_b to track a desired state of p_{bd} in the presence of uncertainties. The relevant tracking error is introduced as follows:

$$e = p_b - p_{bd}. \tag{13}$$

Furthermore, the sliding surface is described by [18]:

$$S(e,t) = \left[\frac{d}{dt}+\lambda\right]^{n-1}\int e\cdot dt, \tag{14}$$

where n is system order and λ is a strictly positive constant that can be interpreted as the slope of the sliding surface in the phase plane. It can be seen that the integral of system error in the sliding surface (Eq. (14)) minimizes the reaching time. It is easy to show that this integral term will also increase the system order by one. Therefore, the system order for the proposed valve as pressure control is two. The sliding surface equation where $n = 2$ is given by:

$$S(e,t) = \left[\frac{d}{dt}+\lambda\right]^{2-1}\int e\cdot dt = e + \lambda\int e\cdot dt, \tag{15}$$

time derivatives of the above equation lead to a linear error equation:

$$\dot{S}(e,t) = \dot{e} + \lambda e, \tag{16}$$

rearranging above equations:

$$\dot{S}(e,t) = \dot{p}_b - \dot{p}_{bd} + \lambda e, \tag{17}$$

using Eq. (17) and Eq. (10), results in:

$$\dot{S}(e,t) = f_1(p_b) - f_2(p_b) - f_3(p_b)u - \dot{p}_{bd} + \lambda e, \tag{18}$$

satisfying the sliding condition:

$$\frac{1}{2}\cdot\frac{d}{dt}S^2 < \eta|S|, \tag{19}$$

η is a positive constant, guaranteeing that the surface S will nonetheless be reached in a finite time smaller than $S(t=0)/\eta$; see [18] for more details. The sliding mode control law is also well presented by:

$$u = u_{eq} + u_s, \tag{20}$$

where u_{eq} is the equivalent control signal that keeps the state within sliding surface and u_s is the switch function that compensates the state when leaving the sliding surface. The best estimation for u_{eq} is obtained by setting $\dot{S}=0$ then from Eq. (18) u_{eq} is derived:

$$f_1(p_b) - f_2(p_b) - f_3(p_b)u - \dot{p}_{bd} + \lambda e = 0, \tag{21}$$

where f_1 and f_2 are unknown functions that are presented by upper and lower bounds and are easily estimated by $\widehat{f}_1$ and $\widehat{f}_2$ which present the mean value of upper and lower bounds so:

$$u_{eq} = \widehat{f}_3^{-1}\left(\widehat{f}_1 - \widehat{f}_2 - \dot{p}_{bd} + \lambda e\right). \tag{22}$$

Error estimation of (f_1-f_2) is considered to be bounded by function $F(e,t)$:

$$F(e,t) \geq \left|\left(\widehat{f}_1 - \widehat{f}_2\right) - \left(f_1 - f_2\right)\right|. \tag{23}$$

Furthermore, f_3 is estimated as follows:

$$\hat{f}_3 = \sqrt{f_{3_{max}} \cdot f_{3_{min}}}, \tag{24}$$

taking a simple form for switching control input:

$$u_s = -K \cdot Sat\left(\frac{S}{\varphi}\right), \tag{25}$$

φ is a strictly positive constant that is explained as a boundary layer thickness neighbouring the sliding surface which prevents chattering and $Sat(s/\varphi)$ is:

$$Sat\left(\frac{S}{\varphi}\right) = \begin{cases} \dfrac{S}{\varphi} & ; \quad \text{if } |S| < \varphi \\ Sign\left(\dfrac{S}{\varphi}\right) & ; \quad \text{if } |S| \geq \varphi \end{cases}. \tag{26}$$

To fulfil essential conditions for Eq. (19) K has to be defined large enough [18]:

$$K = \beta\left(F + \eta\right) + \left(\beta - 1\right)\left|u_{eq}\right|, \tag{27}$$

where $\beta = (f_{3max}/f_{3min})^{0.5}$ is defined as gain margin. The control law which ensures existence of sliding motion in the state – space, provided that $\hat{f}_3 \neq 0$ is:

$$u = \hat{f}_3^{-1}\left[u_{eq} - K \cdot sat\left(\frac{S}{\varphi}\right)\right]. \tag{28}$$

The specified tuning constants of λ and η are set so that the tracking error approaches zero with guaranteed stability. In this case, using trial and error experiments for realizing stability condition in Eq. (19) these constants were suitably adjusted to be 3500 s^{-1} and 550 $kg\cdot(m\cdot s^3)^{-1}$, respectively.

As previously mentioned, the proposed control approach in this part is implemented through a MATLAB/SIMULINK environment. The generated control signals using MATLAB/ Real-time workshop environment with the data acquisition board are used to drive the piezoelectric actuator through the power amplifier. The block diagram of this system is shown in Fig. 12, which clearly indicates that the desired flow rate Q_d is converted to the desired pressure p_{bd}, through reverse function f_2^{-1} which is a simple result from Eq. (7). This is an indication that the desired flow rate is derived simply by controlling the pressure of the load chamber. Any time the operators want to run the control program, they should simply introduce one of the reference inputs, either the pressure or flow rate separately, and set the other input to zero. Through first box in Fig. 12 the desired pressure is initiated and determined, then the controller based on this data and, from the pressure sensor installed on the load chamber, generates appropriate control input to decrease the error between the desired and measured pressure.

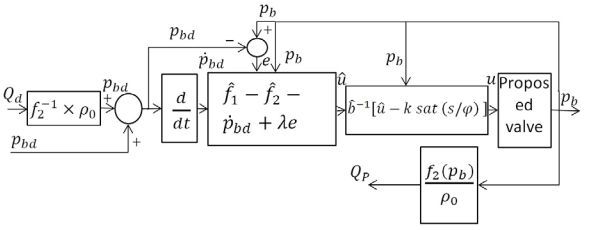

Fig. 12. *Block diagram of the apparatus*

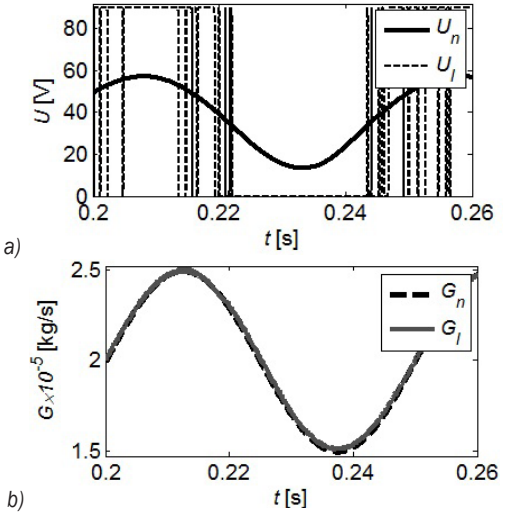

Fig. 13. *Comparison between PI and nonlinear controller; a) input voltage b) mass flow rate*

The first controller that is selected to control a process is a linear controller, such as a PI-controller. To illustrate the effectiveness of the selected nonlinear controller, a set of simulations using a PI-controller were performed and compared with simulation results of the sliding mode approach that was selected to control the proposed valve. A computer program was arranged, both controllers were tuned, and their optimum control coefficients were calculated. Fig. 13 shows simulation results of the proposed valve with a PI- controller and the valve with sliding mode controller. The desired output flow rate was set at $[2+0.5sin(\omega t)]\times 10^{-5}$ kg/s at the frequency of 20 Hz. Part (a) of the figure shows the input voltage to the piezoelectric actuator with PI-controller U_l and nonlinear controller U_n. Part (b) of the figure shows simulation results using a sliding mode approach G_n and simulation results using a PI-controller G_l. The performance of the nonlinear controller and PI-controller is almost the same. There are only some venial oscillations, particularly at an extreme amplitude of the sinusoidal curve of

the linear controller. Also, there is no phase delay in either controller. Part (a) of the figure illustrates that actuating frequency of the piezoelectric actuator with a nonlinear controller is similar to the frequency of the desired flow rate, but the actuating frequency of the actuator with a linear controller is much bigger than the frequency of the same desired flow rate. Furthermore, the nonlinear controller does not need a full range of actuation which is the case for the linear one. Since high actuating frequencies in the full range of motion could be harmful to piezoelectric material and decreases its life expectancy, it is much better to use a sliding mode approach to control output the flow rate or pressure of the valve.

3 RESULTS AND DISCUSSIONS

3.1 Generation of Steady Flow and Pressure

Steady flow or pressure of the proposed valve was generated separately. To evaluate the steady pressure generation ability of the proposed valve, output orifice in Fig. 1 was closed. Results are shown in Fig. 14, where the target pressures are set at 350 kPa and 450 kPa, respectively. The figure shows the reference pressure p_{br} and the actual pressure of the closed load chamber p_b. The results illustrate effective pressure control of the load chamber so that error between the desired pressure p_{br} and the actual pressure p_b is less than 1.5 % at any set pressure.

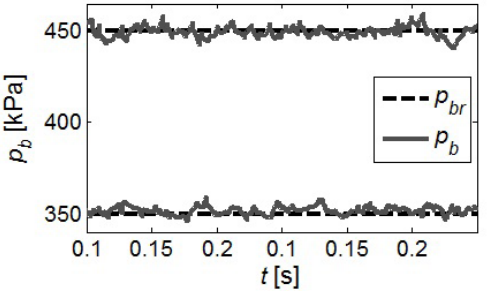

Fig. 14. *Steady pressure generation within the closed load chamber*

To evaluate the proposed valve's steady flow production ability through the output orifice, similar to above-mentioned method, some desired flow was introduced as reference flow to the computer of the controller; the generated flow through the output orifice was then measured by a QFS a quick response laminar flow sensor. Fig. 15 shows the results when the reference flow was set at 0.6×10^{-5} m³/s and 1.1×10^{-5} m³/s. Fig. 15 shows the reference flow Q_r and the measured generated flow Q_p resulted from the pressure change using Eq. (5). The difference between the reference flow Q_r and the generated flow Q_p is less than 2.5 %.

The results of steady pressure and flow generation, demonstrate that the proposed valve can deliver the desired steady flow from output orifice or produce a reference pressure conditions in a closed chamber with acceptable accuracy.

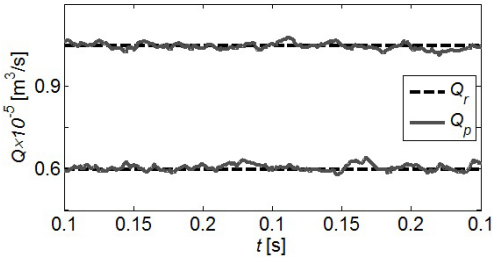

Fig. 15. *Steady flow rate delivery*

3.2 Generation of Unsteady flow and Pressure

The experimental results from the oscillatory pressure condition in the closed load chamber of the valve at two different frequencies of 1 Hz and 25 Hz are presented in Figs. 16 and 17, respectively. The desired pressure was set at the sinusoidal pressure of $[3.5+sin(\omega t)]\times10^5$ Pa. The figures show the reference

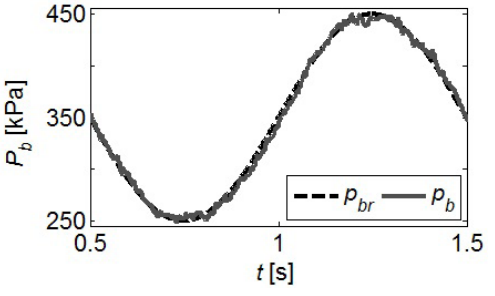

Fig. 16. *Unsteady pressure generation in closed chamber (f = 1 Hz)*

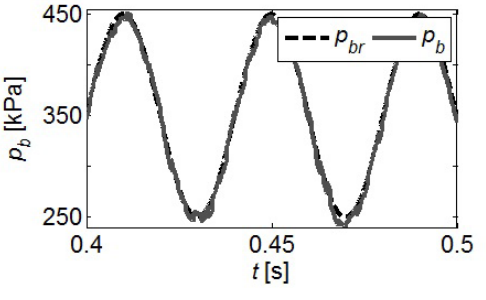

Fig. 17. Unsteady pressure generation in closed chamber (f = 25 Hz)

pressure p_{br} and the actual pressure of the closed load chamber p_b. There is a small difference between p_{br} and p_b at the top and bottom of the sinusoidal curves. Since the pressure change becomes smaller in these areas, the effect of the noise of the pressure sensor becomes larger, but p_{br} and p_b show acceptable limits, as the maximum error between p_{br} and p_b is less than 2.5 %. In particular, the phase has no delay.

The experimental results for oscillatory flow rate are shown in Figs. 18 and 19, similar to Figs. 16 and 17 for pressure results. The desired output flow rate was set at $[0.75+0.45sin(\omega t)]\times10^{-5}$ m³/s at different frequencies of 1 Hz and 25 Hz, respectively. The following figures show the desired flow Q_r and the produced output flow Q_p, which was derived from pressure sensor data based on Eq. (5). The effect of the noise of the pressure sensor was increased and therefore small differences between Q_r and Q_p are detectable. Hence, the flow Q_p obtained from the pressure using Eq. (5) is affected by the noise, Q_r and Q_p are within acceptable limits. In particular, there is no phase delay. The flow Q_p is calculated from the measured pressure based on Eq. (5) and is estimated within an uncertainty of 3.5%. Therefore, the experimental results indicate that the proposed valve can produce oscillatory flow within the same accuracy. Results obtained for Q_r and Q_p at a wide range of frequencies from 1 Hz to 25 Hz, represent excellent agreement for the developed valve model and the experimental data.

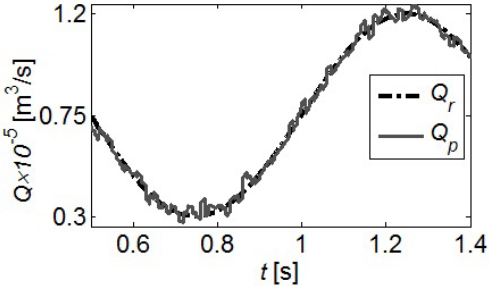

Fig. 18. *Unsteady flow rate delivery (f = 1 Hz)*

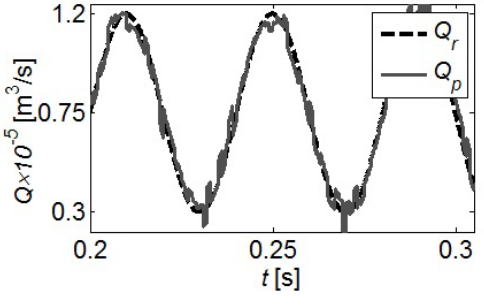

Fig. 19. *Unsteady flow rate delivery (f = 25 Hz)*

4 CONCLUSION

A new piezo-actuated NF valve with isothermal load chamber is introduced. This valve can control pressure or output flow rate separately using only a single pressure sensor. The valve could also be used as a pilot stage of a multistage valve. The effectiveness of the proposed valve has been confirmed and validated experimentally both for steady and unsteady conditions, where it can be operated as a pressure control valve or flow rate generator. The error is less than 2 %, in creating steady and unsteady pressure conditions. As a flow control valve, the designed valve setup can generate steady or sinusoidal oscillatory flow up to 25 Hz within an uncertainty of 3.5 %. Accurate controlling of pressure or flow rate of the valve with nonlinear dynamic behaviour with uncertainty is possible by using the sliding mode control method. It was proved that nonlinear controller is better than a linear one for this valve.

5 NOMENCLATURE

a	flow rate gain with respect to load chamber pressure [kg·(s·Pa)$^{-1}$]
b	critical pressure ratio [–]
e	tracking error of the load chamber pressure [kPa]
C	sonic conductance [m³·(s·Pa)$^{-1}$]
D_{oi}	diameter of the input orifice [mm]
D_{oo}	diameter of the output orifice [mm]
G	mass flow rate [kg·s^{-1}]
n	order of the control system [–]
p_b	control chamber pressure [kPa]
p_s	supply pressure [kPa]
Q	volumetric flow rate [m³·s^{-1}]
R	gas constant [J·(kg·K)$^{-1}$]
S_e	orifice effective area [mm²]
T_c	time constant of the pressure response [s]
K_c	proportional gain of the pressure response [Pa·V^{-1}]
v	piezoelectric actuating voltage [V]
V	control chamber volume [m³]
W	air mass in chamber [kg]
X_n	gap between flapper and head of nozzle [mm]
Θ_b	temperature in control chamber [K]
β	gain margin [–]
ρ	air density [kg·m^{-3}]
λ	slope of sliding surface [s^{-1}]
φ	thickness of boundary layer [m³·s^{-1}]

6 REFERENCES

[1] Herakovic, N., Noe, D. (2006). Analysis of the operation of pilot-stage piezo-actuator valves. *Strojniški vestnik - Journal of Mechanical Engineering*, vol. 52, no. 12, p. 835-851.

[2] Huang, W., Zhao, Z., Zhao, Y., Qi, Q., Huang, Q. (2008). Dynamic characteristic research for piezo pneumatic intelligent valve positioner. *3rd IEEE Conference on Industrial Electronics and Applications*, p. 665–669, **DOI:10.1109/ICIEA.2008.4582598**.

[3] Zeng, H., Yuan, R.-B., Sun, C., Zhang, Z. (2012).Study on performance of laminated piezoelectric pneumatic servo valve. *Procedia Engineering*, vol. 31, p. 1140-1148, **DOI:10.1016/j.proeng.2012.01.1154**.

[4] Richer, E., Hurmuzlu, Y. (2000). A high performance pneumatic force actuator system: Part I—nonlinear mathematical model. *Journal of Dynamic Systems, Measurement, and Control*, vol. 122, no. 3, p. 416-425, **DOI:10.1115/1.1286336**.

[5] Wang, T., Cai, M., Kawashima, K., Kagawa, T. (2005). Modelling of a nozzle-flapper type pneumatic servo valve including the influence of flow force. *International Journal of Fluid Power*, vol. 6, no. 3, p. 33-43, **DOI:10.1080/14399776.2005.10781228**.

[6] Kawashima, K., Youn, C., Toshiharu, K. (2006). Development of a nozzle-flapper-type servo valve using a slit structure. *Journal of Fluids Engineering*, vol. 129, no. 5, p. 573-578, **DOI:10.1115/1.2717617**.

[7] Peng, Z., Sun, C., Yuan, R., Zhang, P. (2012). The CFD analysis of main valve flow field and structural optimization for double-nozzle flapper servo valve. *Procedia Engineering*, vol. 31, p. 115-121, **DOI:10.1016/j.proeng.2012.01.1000**.

[8] Aung, N.Z., Li, S. (2014). A numerical study of cavitation phenomenon in a flapper-nozzle pilot stage of an electrohydraulic servo-valve with an innovative flapper shape. *Energy Conversion and Management*, vol. 77, p. 31-39, **DOI:10.1016/j.enconman.2013.09.009**.

[9] Kagawa, T. (1985). Heat transfer effects on the frequency response of a pneumatic nozzle flapper. *Journal of Dynamic Systems, Measurement, and Control*, vol. 107, no. 4, p. 332-336, **DOI:10.1115/1.3140744**.

[10] Kawashima, K., Kagawa, T. (2003). Unsteady flow generator for gases using an isothermal chamber. *Measurement*, vol. 33, no. 4, p. 333-340, **DOI:10.1016/S0263-2241(03)00003-4**.

[11] Kawashima, K., Fujita, T., Kagawa, T. (1997) Unsteady flow rate measurement of air using isothermal chamber. *Transaction of The Society of Instrument and Control Engineers*, vol. 33, no. 3, 149–154, **DOI:10.9746/sicetr1965.33.149**.

[12] Kawashima, K., Ishii, Y., Funaki, T., Kagawa, T. (2004). Determination of flow rate characteristics of pneumatic solenoid valves using an isothermal chamber. *Journal of Fluids Engineering*, vol. 126, no. 2, p. 273-279, **DOI:10.1115/1.1667888**.

[13] Wang, T., Kawashima, K., Kagawa, T. (2007).Determination of characteristics for electrically modulated pneumatic control valves using isothermal chambers. *International Journal of Fluid Power*, vol. 8, no. 3, p. 5-11, **DOI:10.1080/14399776.2007.10781281**.

[14] Zhao, Y., Jones, B. (1991). A power air-jet actuator with piezotranslator drive stage. *Mechatronics*, vol. 1, no. 2, p. 231-243, **DOI:10.1016/0957-4158(91)90045-C**.

[15] PI Piezo Nano Positioning Catalog (2014/2015). *from http://www.physikinstrumente.com/info/catalogs-brochures-certificates.html*, accessed at 2015-12-26.

[16] ISO6358-1:2013 (2013). *Pneumatic fluid power–Determination of flow-rate characteristics of components using compressible fluids -- Part 1: General rules and test methods for steady-state flow.* International Organization for Standardization, Geneva.

[17] Slotine, J.-J.E., Li, W. (1991). *Applied Nonlinear Control*. Prentice-Hall Englewood Cliffs.

[18] Valiloo, S., Khosrowjerdi, M.J., Salari, M. (2014). LMI based sliding mode surface design with mixed H2/H∞optimization. *Journal of Dynamic Systems, Measurement, and Control*, vol. 136, no. 1, art. no. 11016, **DOI:10.1115/1.4025553**.

Vsebina

Strojniški vestnik - Journal of Mechanical Engineering
letnik 62, (2016), številka 5
Ljubljana, maj 2016
ISSN 0039-2480

Izhaja mesečno

Razširjeni povzetki (extended abstracts)

Jurij Iljaž, Leopold Škerget, Mitja Štrakl, Jure Marn: Optimizacija zadnjega krila pri formuli SAE SI 49
Ayyanar Athijayamani, Raju Ganesamoorthy, Konda Thulasiraman Loganathan, Susaiyappan Sidhardhan: Modeliranje in analiza mehanskih lastnosti kompozita iz vinil estra in vlaken Agave sisalana variageta po metodologiji odzivne površine z zasnovo Box-Behnken SI 50
Van Tuan Do, Le Cuong Nguyen: Adaptivna empirična dekompozicija oblik za odkrivanje napak na ležajih SI 51
Luca Petan, José Luis Ocaña, Janez Grum: Efekti LSP obdelave na integriteto površine 18 % Ni maraging jekla SI 52
K Priya Ajit, Abhinav Gautam, Prabir Kumar Sarkar: Opis duktilnega vedenja maloogljičnega jekla po pristopu CDM SI 53
David Kaljun, Jože Petrišič, Janez Žerovnik: Uporaba Newtonove metode pri modeliranju prostorske porazdelitve svetlobe LED z nameščenimi sekundarnimi optičnimi elementi SI 54
Mohammadreza Kamali, Seyed Ali Jazayeri, Farid Najafi, Kenji Kawashima, Toshiharu Kagawa: Študija učinkovitosti in krmiljenja ventila s piezoaktuatorjem, šobo, odbojno ploščico in izotermno komoro SI 55

Osebne vesti SI 56

Strojniški vestnik - Journal of Mechanical Engineering 62(2016)5, SI 49

Prejeto v recenzijo: 2015-11-25
Prejeto popravljeno: 2016-03-10
Odobreno za objavo: 2016-04-01

Optimizacija zadnjega krila pri formuli SAE

Jurij Iljaž – Leopold Škerget – Mitja Štrakl – Jure Marn
Univerza v Mariboru, Fakulteta za strojništvo, Slovenija

Formula SAE je mednarodno tekmovanje s ciljem zasnove in izdelave dirkalnika ter udeležbe na različnih mednarodnih tekmovanjih po celem svetu, in sicer v različnih disciplinah, od statičnih do dinamičnih. Zaradi varnosti je hitrost vozila oziroma dirkalnika omejena na relativno nizko povprečno hitrost, in sicer z oblikovano zaprto progo. Tako je izziv med posameznimi ekipami za najboljša mesta toliko večji. Ravno zaradi te omejitve je izziv tudi oblikovati primerno aerodinamiko, ki je sestavljena iz sprednjega in zadnjega krila ter oblikovanega dna z zadnjim difuzorjem, saj je cilj oblikovati aerodinamični paket na način zagotavljanja maksimalne potisne sile, kar vodi v hitrejšo vožnjo skozi ovinek in posledično hitrejši krog na tekmi.

Tako pričujoče delo obravnava problematiko dizajniranja oziroma optimizacijo zadnjega krila pri formuli SAE za nizke hitrosti. Zaradi nizkih hitrosti se pojavi problematika prekrmarjenosti dirkalnika sredi ovinka, kar je seveda nezaželeno. Z optimizacijo dizajna zadnjega krila je možno povečati potisno silo na zadnjih kolesih, kar izboljša oprijem ter nevtralnost dirkalnika. V delu je predstavljena problematika in način dizajniranja aerodinamičnih komponent, kot je zadnje krilo, za nizke hitrosti, kar predstavlja novost na tem področju prav tako pa prednost predkrilca pred dodatnim zakrilcem.

Sodobna inženirska orodja, kot je RDT, nam omogočajo numerično testiranje in analiziranje posameznih komponent, kar omogoča hitrejši napredek tudi v moto športu. Tako je bil za ovrednotenje posameznega dizajna in analizo zadnjega krila uporabljen numerični pristop oziroma 3D numerična simulacija na osnovi SST-RANS modela. Pri tem model ne obravnava osamljenega krila, kot drugi avtorji, temveč celoten dirkalnik z vsemi komponentami. Le tako je mogoče zajeti medsebojni vpliv komponent in s tem natančneje simulirati aerodinamiko vozila. Zaradi zahtevnosti modeliranja tokovnih razmer okoli vozila, je bil posamezni dizajn krila ovrednoten pri konstantni vožnji naravnost. Prav tako je bila zaradi simetrije dirkalnika modelirana le njegova polovica, kar močno skrajša računski čas in poveča število numeričnih testiranj. V delu prav tako podrobneje opisana analiza računskega območja in mreže ter potrebni robni pogoji za realen fizikalni opis problem ob upoštevanju vrtečih se koles in gibanja ceste. Delo analizira dva različna dizajna zadnjega večdelnega krila v okviru pravilnika, in sicer prvi osnovni dizajn je sestavljen iz glavnega dela in dveh zakrilc, medtem ko je drugi, naprednejši dizajn, sestavljen iz glavnega dela, 3D zavitega zakrilca in sprednjega predkrilca, ki omogoča večje vpadne kote. Pri tem imata oba dizajna še veliki stranski plošči in Gurney zakrilce na zadnjem zakrilcu. Narejena je bila analiza višine zadnjega krila ter analiza vpadnega kota, kot tudi vpliv sprednjega krila na zadnje krilo.

Rezultati numeričnih simulacij kažejo, da je smiselna čim višja postavitev zadnjega krila, ki pa je omejena s pravilnikom. Osnovni dizajn doseže pri višini 760 mm od tal maksimalno potisno silo pri vpadnem kotu 8°, medtem ko naprednejši dizajn doseže le-to pri kotu 24°, in sicer za 6 % večjo. Sila upora krila je zaradi večje potisne sile drugega dizajna tudi večja, vendar je pri nizkih hitrostih formule nepomembna, saj ne predstavlja velikega odjema moči motorja pri pospeševanju. Še večja razlika med osnovnim in naprednejšim dizajnom se pojavi pri višji hitrosti saj aerodinamična sila raste s kvadratom hitrosti. Razlika se pojavi tudi pri velikih vpadnih kotih, ko pride do odcepitve oziroma porušitve toka. Pri osnovnem dizajnu je porušitev toka z večanjem vpadnega kota izrazita, medtem ko pri naprednem dizajnu ne pride do izrazite porušitve. Rezultati kažejo na prednost predkrilca pred dodatnim zakrilcem. Numerične analize tudi kažejo, da ima močno ukrivljeno sprednje krilo pozitiven vpliv na aerodinamiko zadnjega krila oziroma da je potrebno sprednje in zadnje krilo dizajnirati vzajemno.

Ključne besede: RANS simulacija, zadnje krilo, optimizacija, računska dinamika tekočin (RTD), potisna sila, aerodinamika vozil

*Naslov avtorja za dopisovanje: Univerza v Mariboru, Fakulteta za strojništvo, Smetanova ulica 17, 2000 Maribor, Slovenija jurij.iljaz@um.si

Strojniški vestnik - Journal of Mechanical Engineering 62(2016)5, SI 50

Prejeto v recenzijo: 2015-04-29
Prejeto popravljeno: 2015-09-22
Odobreno za objavo: 2015-10-19

Modeliranje in analiza mehanskih lastnosti kompozita iz vinil estra in vlaken Agave sisalana variageta po metodologiji odzivne površine z zasnovo Box-Behnken

Ayyanar Athijayamani[1,*] – Raju Ganesamoorthy[2] – Konda Thulasiraman Loganathan[1] – Susaiyappan Sidhardhan[3]

[1] Kolidž za inženiring in tehnologijo Alagappa Chettiar, Oddelek za strojništvo, Indija
[2] Tehniški kolidž Sayasuriya, Oddelek za strojništvo, Indija
[3] Vladni tehniški kolidž, Oddelek za gradbeništvo, Indija

V literaturi ni mogoče najti nobenih virov o kompozitu, sestavljenem iz vinil estra in vlaken Agave sisalana variegata. Namen te raziskave je preučitev vpliva procesnih parametrov na mehanske lastnosti vinil estra (FRVE), ojačenega z vlakni Agave sisalana variegata (ASC), po metodologiji odzivne površine (RSM) z zasnovo Box-Behnken (BB).

Glavni cilj študije je osvetlitev vpliva procesnih parametrov kot so dolžina, vsebnost in premer vlaken na natezno in upogibno trdnost kompozitov ASVFRVE. Da bi bolje razumeli odvisnosti med parametri in odzivom ter določili mehanske lastnosti kompozitov, so avtorji uporabili metodo RSM z zasnovo eksperimenta BB.

Na podlagi te zasnove so bili nato opravljeni eksperimentalni preizkusi, pri čemer je bilo zajetih več setov podatkov. Na podlagi eksperimentalnih podatkov so bili nato razviti matematični modeli za opis vpliva posameznih procesnih parametrov in njihovih interakcij na mehanske lastnosti kompozitov ASVFRVE. S primerjavo je bilo analizirano ujemanje napovedanih vrednosti z eksperimentalnimi.

Ujem eksperimentalno določene trdnosti in napovedane trdnosti je bil določen z multiplo regresijsko analizo in opredeljen s polinomsko enačbo drugega reda. Razviti modeli pojasnijo 98,54 % variance pri natezne trdnosti in 99,24 % variance pri upogibne trdnosti. Validacija je pokazala, da se napovedane vrednosti dobro ujemajo z rezultati eksperimenta.

Optimalni parametri procesa izdelava kompozitov ASVFRVE z vidika natezne in upogibne trdnosti so bili določeni z grafikoni in modeli odzivne površine. Optimalni parametri procesa izdelave so 3. raven dolžine vlaken (13 mm), 2. raven vsebnosti vlaken (35,19 ut. %) in 1. raven premera vlaken (0,24 mm). V potrditveni študiji je bilo opravljenih tudi pet eksperimentalnih preskusov z optimalnimi ravnmi procesnih parametrov. Napovedani odzivni vrednosti za natezno in upogibno trdnost v optimalnih pogojih sta bili 41,7 MPa oz. 52,1 MPa.

Lastnosti polimernih kompozitov, ojačenih z naravnimi vlakni, so odvisne tako od procesnih parametrov, kot sta temperatura in tlak, kakor tudi od vlaken in matriksa. Z upoštevanjem teh parametrov se bo izboljšala točnost napovedi.

Kompozit vinil estra, ojačenega z vlakni Agave sisalana variegata, spada v novo družino polimernih kompozitov. Mehanske lastnosti kompozita, kot sta natezna in upogibna trdnost, so bile napovedane s polinomsko enačbo drugega reda po metodi multiple regresijske analize. Optimalne ravni procesnih parametrov pri izdelavi so bile določene z grafikonom odzivne površine in z modeli.

Predstavljeno delo dokazuje, da je zasnova BB pri metodologiji odzivne površine primerna za modeliranje in optimizacijo mehanskih lastnosti polimernih kompozitov z naravnimi vlakni. Obenem predstavlja tudi ekonomično sredstvo za pridobivanje največje količine informacij v najkrajšem času in z najmanjšim številom eksperimentov.

Ključne besede: vlakna Agave sisalana variegata, kompozit, natezna trdnost, upogibna trdnost, zasnova Box Behnken, metodologija odzivne površine

*Naslov avtorja za dopisovanje: Kolidž za inženiring in tehnologijo Alagappa Chettiar, Oddelek za strojništvo, Indija, athimania@rediffmail.com

Strojniški vestnik - Journal of Mechanical Engineering 62(2016)5, SI 51

Prejeto v recenzijo: 2015-09-29
Prejeto popravljeno: 2016-03-08
Odobreno za objavo: 2016-03-21

Adaptivna empirična dekompozicija oblik za odkrivanje napak na ležajih

Van Tuan Do* – Le Cuong Nguyen
Univerza za elektroenergetiko, Oddelek za elektroniko in telekomunikacije, Vietnam

Članek predstavlja poskus izboljšanja učinkovitosti odkrivanja napak na nizkohitrostnih ležajih z adaptivno empirično dekompozicijo oblik (AEDO) v primerjavi z izvirno metodo EDO in analizo ovojnic.

Izvirna metoda EDO se včasih ne izkaže najbolje, če so podatki močno obremenjeni s šumom ali z drugimi viri. Težave se še potencirajo, če v signalu dominirajo druge komponente in imajo signifikantne amplitude v bližini frekvenc dela signala, ki izvira iz napake. Metoda EDO v procesu ekstrahiranja funkcij lastnih oblik (IMF) odstranjuje nizkofrekvenčne komponente, dokler ne pride do ostanka, ki postane IMF. Dokler IMF ni najdena, se lahko torej odstrani tudi določen del signala napake in se nato pojavi v naslednjih IMF. Zato se lahko zgodi, da se energija signala napake razširi po več IMF in v tem primeru bo možnost zaznavanje lastnosti napak v katerikoli od teh IMF majhna. Po predlagani novi metodi se funkcije IMF ustvarijo tako, da ena od njih vsebuje večino energije signala napake.

Razlog za neučinkovitost metode EDO leži v tem, da se energija dela signala, ki nastane zaradi napake, pri veliki pasovni širini porazdeli med več IMF. Ekstrahiranje IMF pri adaptivni EDO zato poteka tako, da se energija frekvenčnih komponent ostanka izračunava z osredotočenjem na segment frekvenčnega območja, ki vsebuje imensko frekvenco in njene harmonike. Ta energija se imenuje vršna energija in določa, ali so nizke frekvence povezane z napakami ali ne. IMF postane ostanek v točki, kjer ima vršna energija ostanka največjo vrednost. Če so nizkofrekvenčne komponente povezane z napako, se ohranijo v ekstrahirani IMF, sicer pa se odstranijo in se pojavijo v naslednjih IMF.

Rezultati simulacij in eksperimentov kažejo, da je metoda AEDO uspešnejša od metode EDO in analize ovojnice pri odkrivanju napak na nizkohitrostnih ležajih.

Predlagana je nova metoda na podlagi EDO, ki daje boljše rezultate od metode EDO in analize ovojnic. Metoda je primerna za realnočasovno uporabo v industriji za samodejno odkrivanje napak na ležajih.

Ključne besede: odkrivanje napak na ležajih, Hilbert-Huangove transformacije, empirična dekompozicija oblik, funkcije lastnih oblik, analiza ovojnice, imenska frekvenca

*Naslov avtorja za dopisovanje: Univerza za elektroenergetiko, Oddelek za elektroniko in telekomunikacije, 235 Hoang Quoc Viet, Hanoi, Vietnam, tuandv@epu.edu.vn

Strojniški vestnik - Journal of Mechanical Engineering 62(2016)5, SI 52

Prejeto v recenzijo: 2015-12-16
Prejeto popravljeno: 2016-03-11
Odobreno za objavo: 2016-03-21

Efekti LSP obdelave na integriteto površine 18 % Ni maraging jekla

Luca Petan[1] – José Luis Ocaña[2] – Janez Grum[1,*]
[1] Univerza v Ljubljani, Fakulteta za strojništvo, Slovenija
[2] Politehnična univerza v Madridu, Laserski center UPM, Španija

Izločevalno utrjevalna in visoko-trdnostna maraging jekla se uporabljajo za izdelavo zahtevnih konstrukcijskih delov v letalstvu in vesoljski industriji kot tudi za izdelavo orodij za tlačno litje. Komponente iz maraging jekla so pogosto med obratovanjem izpostavljene nezaželenim pojavom, kot so mehansko in termično utrujanje, korozija, obraba, ki vplivajo na nastanek različnih površinskih poškodb in na iniciacijo ter rast razpok, kar vodi do odpovedi strojne komponente. V zadnjih nekaj letih obstaja povečan interes za raziskovanje integritete udarno utrjenih površin in za ocenjevanje odpornosti maraging ter orodnih jekel na mehansko in termično utrujanje.

V okviru predstavljene raziskave so bili analizirani efekti laserskega udarnega utrjevanja (LSP) na integriteto površine maraging jekla X2NiCoMo18-9-5 s poudarkom na doseženi hrapavosti površine, poteka zaostalih napetosti in mikrotrdote v tankem površinskem sloju. Ploščati vzorci iz valjanega maraging jekla z dimenzijami 40 mm × 40 mm, so bili topilno žarjeni na temperaturi 820 °C (1 h) in nato gašeni na zraku. Polovica vzorcev je bila izločevalno utrjena na 480 °C (3 h). Gašeni in izločevalno utrjeni vzorci so bili brušeni in nato v drugi fazi priprave lasersko udarno utrjeni s tremi gostotami laserskih pulzov (900 cm^{-2}, 1600 cm^{-2}, 2500 cm^{-2}). Uporabljen je bil Q-stikalni Nd:YAG laser z energijo pulza 2,8 J, trajanjem pulza 10 ns in lasersko pego premera 1,5 mm.

Hrapavost površine neobdelanih in LSP vzorcev je bila analizirana v longitudinalni ter transverzalni smeri in popisana z aritmetično srednjo hrapavostjo *Ra* (ISO 4287) in srednjo globino hrapavosti *Rz* (DIN 4768) z upoštevanjem poti vodenja laserskega snopa. Efekt laserskih udarnih valov LSP postopka na mehanske lastnosti površinskega sloja je bil raziskan z meritvami zaostalih napetosti in mikrotrdote v površinskem sloju. Meritve zaostalih napetosti so bile izvedene z relaksacijsko metodo z vrtanjem slepe izvrtine v skladu s standardom ASTM E837. Potek mikrotrdote je bil določen z uporabo Vickersove metode (ISO 6507-1) pri obremenitvi z maso 200 g in časom vtiskovanja 15 s.

Rezultati raziskave so pokazali izrazito povečanje hrapavosti površine *Ra* in *Rz* po laserskem udarnem utrjevanju, kot posledica kombiniranega efekta mehanskega pritiska nastale plazme in ablativne narave laserskega postopka. Na brušenih vzorcih je bila dosežena hrapavost 0,17 μm, ki se je po laserskem udarnem utrjevanju povečala na 1,11 μm, kar predstavlja še vedno ugodno hrapavost površine. Mehanski efekt induciranih udarnih valov je povzročil trajno deformacijo površinskega sloja z nastankom želenih tlačnih zaostalih napetosti pod obsevanim področjem. Na površini izločevalno utrjenih vzorcev so bile dosežene tlačne napetosti okoli –450 MPa in v gašenem stanju –750 MPa. Analiza mikrotrdote gašenega in izločevalno utrjenega vzorca je potrdila mehansko utrditev površinskega sloja. Rezultati nakazujejo, da se s povečevanjem gostote laserskih pulzov poveča tako hrapavost površine kot tudi mikrotrdota in globina s tlačnimi zaostalimi napetostmi.

Študija potrjuje, da LSP v površinskem sloju 18 % Ni maraging jekla ustvari zaželene tlačne zaostale napetosti tako po vnosu kot po poteku z globino. Izkazalo se je tudi, da je dosežena hrapavost površine relativno nizka, zato se pričakuje minimalen vpliv porasta hrapavosti med obratovanjem LSP obdelane komponente. Dosežena kombinacija površinskih karakteristik lahko prepreči nastanek in rast obstoječih razpok med obratovanjem 18 % Ni maraging jekla pri temperaturi okolice in pri povišanih temperaturah. Slednje bi bilo mogoče potrditi z nadgradnjo študije z izvedbo analize odpornosti lasersko udarno utrjene površine na mehansko in termično utrujanje.

Ključne besede: lasersko udarno utrjevanje, tlačne zaostale napetosti, mikrotrdota, hrapavost površine

*Naslov avtorja za dopisovanje: Univerza v Ljubljani, Fakulteta za strojništvo, Aškerčeva 6, 1000 Ljubljana, Slovenija, janez.grum@fs.uni-lj.si

Strojniški vestnik - Journal of Mechanical Engineering 62(2016)5, SI 53

Prejeto v recenzijo: 2015-11-15
Prejeto popravljeno: 2016-01-29
Odobreno za objavo: 2016-03-21

Opis duktilnega vedenja malooglјičnega jekla po pristopu CDM

K Priya Ajit[1,*] – Abhinav Gautam[2] – Prabir Kumar Sarkar[2]
[1] Indijska rudarska šola, Oddelek za tehnično rudarstvo, Indija
[2] Indijska rudarska šola, Oddelek za strojništvo, Indija

Duktilne poškodbe v materialu so posledica zmanjševanja togosti ob povečevanju plastičnih deformacij, vse dokler ne pride do zloma nosilnega elementa. Velja razlaga, da je mikroločevanje v kovinskih polikristaliničnih agregatih ob močnem lokalnem plastičnem tečenju posledica procesa razvoja praznin oz. votlin. Opredelitev primernih meril za poškodbe pomaga pri oblikovanju zakonov razvoja, ki so potrebni za popis duktilnega odziva do zloma za določen razred tehničnih materialov. Pristop mehanike poškodb v kontinuumu (CDM) obravnava poškodbe na podlagi efektivne površinske gostote razpok. Z uporabo konstitutivne enačbe CDM je mogoče analizirati raven poškodb pri različnih materialih in s podobnim vrednotenjem je mogoče pripraviti potrebne smernice za nadzor in zagotavljanje boljše izkoriščenosti materialov. Pristop lahko pomaga tudi pri analizi komponent po zlomu za identifikacijo vzroka odpovedi. Vrednotenje poškodb je priročno orodje pri izdelavi konstrukcijskih delov avtomobilov in letal, pri katerih je kritična oblika.

Predstavljena študija obravnava oceno duktilnih poškodb pri dveh vrstah malooglјičnega jekla po pristopu CDM – IFHS (jeklo brez intersticijsko raztopljenih elementov) in C-Mn-440. Za obe jekli je značilna kombinacija trdnosti in preoblikovalnosti. Enoosni model duktilnih poškodb, ki sta ga razvila Bhattacharya in Ellingwood, opisuje poškodbe kot funkcijo plastičnih deformacij in deformacijskega utrjanja. V študiji je bil opravljen preizkus s cikli obremenitve/razbremenitve za neposredno oceno poškodbene spremenljivke in drugih parametrov z namenom opredelitve vpliva eksponenta deformacijskega utrjanja na poškodbeno spremenljivko D. Preizkus je bil opravljen na stroju Instron 8801 s hitrostjo obremenjevanja 10^{-3}/s za vrednotenje osnovnih mehanskih lastnosti. Iz rezultatov eksperimenta so izpeljani vsi obravnavani parametri, ovrednotena pa je tudi odvisnost duktilnih poškodb od eksponenta utrjanja. Duktilno tečenje tako postane napovedljivo po modelu tečenja, rezultat pa je poškodbena spremenljivka D v odvisnosti od efektivnih napetosti. Napovedani rezultati se dobro ujemajo z eksperimenti do stabilnega plastičnega območja.

Novost predstavljenega dela je v identifikaciji neposrednega vpliva eksponenta deformacijskega utrjanja na poškodbeno spremenljivko. Vpliv eksponenta deformacijskega utrjanja n na poškodbeni parameter za namene določitve duktilnega vedenja materiala po pristopu CDM do danes še ni bil eksplicitno upoštevan, čeprav je že vdelan v več poškodbenih modelov. Eksponent predstavlja merilo za preoblikovalnost, ki je neposredno povezana z duktilnostjo in gostoto praznin, in deformacijsko utrjanje je tako primerno merilo za duktilne poškodbe. Podatki so ocenjeni iz krivulj odvisnosti pravih deformacij od pravih napetosti za vsak korak v cikličnem preizkusu z obremenitvijo/razbremenitvijo. Variabilnost eksponenta utrjevanja je bila uporabljena za napoved poškodbene spremenljivke po poškodbenem zakonu Bhattacharyje in Ellingwooda. Z rastjo poškodb se zmanjšuje velikost eksponenta utrjanja, funkcija pa je nelinearna. Napovedi poškodb na podlagi modela razvoja se dobro ujemajo z eksperimentalnimi rezultati.

Pristop CDM je uporaben za karakterizacijo duktilnih poškodb pri malooglјičnih jeklih. V predstavljenem delu se je izkazalo, da lahko z vrednostjo eksponenta deformacijskega utrjanja v pravem zakonu razvoja zelo dobro napovemo eksperimentalno krivuljo tečenja. Študija ne upošteva vpliva vibracij ali cikličnih obremenitev na rast poškodb in ekipa avtorjev načrtuje to za prihodnje raziskave. Pristop daje konstruktorjem potrebne informacije za odločanje pri izbiri materialov. Malooglјična jekla se pogosto uporabljajo v avtomobilskih karoserijah, kjer so podvržena različnim dinamičnim obremenitvam, poznavanje utrujenostnega poškodbenega vedenja pa je zato nujno za boljši izkoristek teh materialov.

Ključne besede: poškodbe, mehanika poškodb v kontinuum, degradacija modula, malooglјično jeklo

*Naslov avtorja za dopisovanje: Indijska rudarska šola, Oddelek za tehnično rudarstvo, Dhanbad, Indija, ajit160984@gmail.com

Strojniški vestnik - Journal of Mechanical Engineering 62(2016)5, SI 54

Prejeto v recenzijo: 2015-11-24
Prejeto popravljeno: 2016-03-08
Odobreno za objavo: 2016-03-21

Uporaba Newtonove metode pri modeliranju prostorske porazdelitve svetlobe LED z nameščenimi sekundarnimi optičnimi elementi

David Kaljun[1,*] – Jože Petrišič[1] – Janez Žerovnik[1,2]
[1]Univerza v Ljubljani, Fakulteta za strojništvo, Slovenija
[2]Inštitut za matematiko, fiziko in mehaniko, Slovenija

Zagotavljanje učinkovitih delovnih procesov je ključ do uspešnega in konkurenčnega podjetja. Še posebej velja to za proces razvoja svetil. Tako se v želji po hitrejšem in cenejšem razvoju velikokrat poslužujemo računalniških simulacij prostorske porazdelitve svetilnosti svetila (fotometrija), namesto realnih meritev. Simulacije namreč omogočajo testiranje svetila z različnimi optičnimi elementi v relativno kratkem času, kar omogoča preizkus več variant izdelka. Vendar pa so rezultati simulacij v celoti odvisni od vhodnih podatkov. Tako se lahko kar hitro zgodi, da se simulacijski rezultati ne skladajo z dejanskimi meritvami.

Velikokrat je za razkorak kriv prav standardni zapis fotometrije svetil, ki predvideva datoteko, katera je sestavljena iz seznama prostorskih vektorjev. Vsak vektor predstavlja žarek svetlobe z določeno svetlobno intenziteto v določeni smeri. Za natančen opis fotometrije bi tako v datoteki moralo biti zapisano več sto tisoč vektorjev, vendar jih večinoma najdemo le okoli tri do deset tisoč. Razlog za majhno število vektorjev je prenosljivost datotek, ki z večjim številom vektorjev postanejo prevelike, datoteke z majhnim številom vektorjev pa vnašajo prevelike pogreške, ki se tekom simulacije dodatno potencirajo.

Očitna rešitev je boljši zapis fotometrije, ki bi ob ohranjanju kakovosti podatkov zmanjšal število potrebnih parametrov. Leta 2008 sta Moreno in Sun predstavila fenomenološki matematični model, ki je z nekaj parametri uspešno opisal fotometrijo LED brez nameščenih leč. Avtorjema je uspelo zapisati fotometrije posameznih LED z matematičnim modelom, ki je vseboval vsega devet parametrov v nasprotju s standardnim zapisom. Model smo prevzeli in ga za apliciranje na LED z nameščenimi lečami modificirali. Podrobnosti modifikacije modela in dokaz ustreznosti smo predstavili v prejšnjih objavah. Model je sestavljen iz vsote kosinusnih funkcij. Vsaka funkcija ima tri parametre. Vsota funkcij pa je normirana z najvišjo vrednostjo svetilnosti iz obravnavane fotometrije, kar doda en parameter, ki je skupen vsem funkcijam. Dodaten parameter omogoča, da so vrednosti vseh parametrov v omejenih intervalih. Definicija modela pa je samo polovica rešitve, kajti za vsako fotometrijo je potrebno poiskati nabor parametrov, ki jo dovolj dobro opiše. Glede na velikost množice dopustnih rešitev ($6{,}85\times10^9$ setov pri devetih funkcijskih parametrih in osnovni diskretizaciji iskalnega prostora) je smiselno uvesti iskalne algoritme. Do sedaj smo implementirali sedem različnih hevrističnih algoritmov od klasičnega preiskovanja z izbiro soseščine do genetskih algoritmov.

V članku predstavljamo implementacijo numerične metode z namenom pohitritve delovanja. Model je sestavljen iz zveznih funkcij, kar omogoča uporabo različnih numeričnih metod vendar smo se odločili za implementacijo Newtonove metode zaradi robustnosti in relativno enostavnega delovanja ter kvadratične konvergence, ki bi morala zagotavljati vidno pohitritev delovanja sistema.

Pripravili smo eksperiment, ki je vključeval iskanje parametrov za sto umetnih in trinajst realnih leč z desetimi različnimi algoritmi. Rezultate eksperimenta smo primerjali po treh kriterijih: kakovosti rešitev, računskem času in statistično obdelavo z uporabo Wilcoxon-ovega testa. Rezultati pokažejo, da je vsaj na naših primerih, posrečena rešitev, kombinacija lokalnega iskanja izbranih začetnih približkov z diskretnimi optimizacijskimi algoritmi, ki jim sledi hitra in na teh približkih zanesljiva konvergenca Newtonove metode. V primerjavi s prej objavljenimi rezultati nova metoda v krajšem času (tudi do 10 krat) najde rešitve, ki znatno zmanjšajo napako, (tudi do 60 %).
Ključne besede: metoda najmanjših kvadratov, Newtonova metoda, diskretna optimizacija, lokalno iskanje, porazdelitev svetlobe, LED

*Naslov avtorja za dopisovanje: Univerza v Ljubljani, Fakulteta za strojništvo, Aškerčeva 6, 1000 Ljubljana, Slovenija, david.kaljun@fs.uni-lj.si

Strojniški vestnik - Journal of Mechanical Engineering 62(2016)5, SI 55

Prejeto v recenzijo: 2015-12-26
Prejeto popravljeno: 2016-03-03
Odobreno za objavo: 2016-03-21

Študija učinkovitosti in krmiljenja ventila s piezoaktuatorjem, šobo, odbojno ploščico in izotermno komoro

Mohammadreza Kamali[1,*] – Seyed Ali Jazayeri[1] –Farid Najafi[2] – Kenji Kawashima[3]– Toshiharu Kagawa[4]

[1] Tehniška univerza K. N. Toosi, Fakulteta za strojništvo, Iran
[2] Univerza v Guilanu Tehniška fakulteta, Iran
[3] Medicinska in stomatološka univerza v Tokiu, Institut za biomateriale in bioinženiring, Japonska
[4] Tehnološki institut v Tokiu, Japonska

Namen predstavljene raziskave je uvedba novega ventila s šobo in odbojno ploščico (NF), za katerega so značilni spremenjen razpored delovnih elementov za izboljšanje dinamike, poenostavitev enačb ter odprava nekaterih omejitev tradicionalnih NF-ventilov. Za izpolnitev teh ciljev je bil novi ventil s šobo in odbojno ploščico zasnovan in opremljen s piezoelektričnim aktuatorjem in izotermno polnilno komoro.

Dinamika polnilne komore, ki je glavni podsestav ventila, ima v celotni dinamiki ventila pomembno vlogo. Neobstoj točnega modela za spreminjanje stanja zraka v komori otežuje krmiljenje ventila. Zagotovitev izotermnih pogojev v komori ventila odpravlja dinamične napake zaradi temperaturnih sprememb v komori, vodilne enačbe za napovedovanje tlaka v komori pa so zato veliko točnejše in preprostejše. Izotermno stanje v komori ventila torej poenostavi njegovo krmiljenje, saj je le z enim samim tlačnim tipalom v komori ventila mogoče krmiliti tlak in pretok.

Tradicionalni NF-ventili so opremljeni z elektromagnetnim pretvornikom za pogon odbojne ploščice. Med njihove slabosti štejejo velike dimenzije, velika poraba električnega toka, počasen odziv in občutljivost na elektromagnetne motnje. Ventil, ki je predstavljen v tem članku, je opremljen s piezoelektričnim aktuatorjem v sestavi zloga. Le-ta je zaradi svojih edinstvenih lastnosti obenem tudi najprimernejša izbira za nevarna in občutljiva industrijska ali medicinska okolja. Piezoelektrični aktuatorji namreč porabijo bistveno manj električne energije in se hitreje odzivajo, mehanizem pa se ne iskri in ne oddaja magnetnih polj. Zaradi naštetih lastnosti so primerni za pnevmatske ventile. Togost izbranega aktuatorja pri praznilnem toku iz šobe zmanjšuje kompleksnost dinamičnih enačb ventila.

Opravljena je bila teoretična analiza ventila za izpeljavo natančnejšega matematičnega in simulacijskega modela in postavljeno je bilo preizkuševališče za validacijo rezultatov simulacij. Eksperimentalno so bile ovrednotene statične in dinamične lastnosti predlaganega ventila za validacijo razvitega modela in osvetlitev prednosti ventila. Zaradi nelinearnega vedenja predlaganega ventila in negotovosti pri nekaterih spremenljivkah v enačbah ventila je bil oblikovan in uporabljen drseči pristop za natančnejše krmiljenje izhodnega pretoka in tlaka.

Učinkovitost ventila je bila potrjena in eksperimentalno validirana v stacionarnih in nestacionarnih pogojih, kjer lahko deluje kot ventil za regulacijo tlaka ali kot generator pretoka. Napaka v pogojih stacionarnega in nestacionarnega tlaka je manjša od 2 %. Ventil v konfiguraciji za regulacijo pretoka lahko ustvarja stacionarne ali sinusne oscilirajoče tokove do 25 Hz z negotovostjo 3,5 %. Točna regulacija tlaka ali pretoka z ventilom, za katerega je značilna nelinearna dinamika, je možna po metodi drsečega krmiljenja. Dokazano je, da je nelinearen krmilnik primernejši za ta ventil od linearnega krmilnika.

Raziskava temelji na teoretičnih analizah in na eksperimentalnih preizkusih, ki uvajajo novo zgradbo NF-mehanizma. Njegove vodilne dinamične enačbe so bistveno preprostejše. Ventil je uporaben za regulacijo tlaka ali pretoka in je primeren za predkrmilno stopnjo dvostopenjskega ventila. Predlagani ventil je dovolj hiter tudi za predkrmilno stopnjo bistveno večjih ventilov in v našem laboratoriju se že izvajajo dodatne raziskave uporabnosti ventila v predkrmilni stopnji za upravljanje glavne stopnje večjega pnevmatskega ventila.

Ključne besede: ventil s šobo in odbojno ploščico (nozzle-flapper), izotermna komora, piezoelektrični aktuator, drseči pristop, ventil za regulacijo tlaka, generator pretoka

*Naslov avtorja za dopisovanje: K.N.Toosi University of Technology , Vanak Sq., Teheran, Iran, mohammadrkamali@gmail.com

DOKTORSKA DISERTACIJA, ZNANSTVENO MAGISTRSKO DELO

DOKTORSKA DISERTACIJA

Na Fakulteti za strojništvo Univerze v Ljubljani je obranili svojo doktorsko disertacijo:

- dne *8. aprila 2016* **Luka ČERČE** z naslovom: »Napovedovanje obstojnosti rezalnih orodij z upoštevanjem njihove prostorske obrabe« (mentor: prof. dr. Janez Kopač);

Obraba rezalnih orodij ima značilen vpliv na kakovost izdelkov in učinkovitost procesa obdelave. Kljub trenutno visoki stopnji avtomatizacije v obdelovalni industriji obstaja nekaj ključnih področij, ki preprečujejo popolno avtomatizacijo procesa odrezavanja. Eno od teh področij je karakterizacija obrabe rezalnega orodja, saj meritev običajno opravljamo izven obdelovalnega stroja, ročno z uporabo orodjarskega mikroskopa. Zato ima sprotna karakterizacija obrabe rezalnega orodja neposredno na obdelovalnem stroju ključen pomen pri zmanjšanju časa in stroškov obdelave ter pri večanju skupne učinkovitosti odrezovalnega procesa.

Odgovor na to je inovativen, robusten in zanesljiv merilni sistem za sprotno merjenje obrabe rezalnega orodja, ki je razvit in predstavljen v tem delu. Sistem omogoča prostorsko merjenje obrabe s podrobnejšo analizo prečnih prerezov meritev, kar predstavlja veliko prednost pred trenutno uporabljanimi metodami (orodjarski mikroskop itd.). Z uporabo razvitega merilnega sistema ni več potrebe po izpenjanju rezalnega orodja, prav tako se izognemo ročni kontroli stanja rezalnega orodja in dosežemo objektivno merjenje obrabe. S tem razviti sistem omogoča avtomatsko in robustno karakterizacijo obrabe ob zmanjšanju časa, potrebnega za izvedbo meritve obrabe rezalnega orodja.

Poleg navedenega je v delu opravljena karakterizacija obstojnosti rezalnega orodja na podlagi tridimenzionalne analize geometrije in obrabe rezalnega orodja. Kot rezultat je na podlagi prostorskih značilnosti izmerjene obrabe rezalnega orodja predlagana nova metodologija napovedovanja obstojnosti rezalnega orodja.

ZNANSTVENO MAGISTRSKO DELO

Na Fakulteti za strojništvo Univerze v Ljubljani je z uspehom zagovarjal svoje magistrsko delo:

- *dne 12. aprila 2016* **Ivan MARC** z naslovom: »Projekt vzporednega razvoja izdelka in vitka proizvodnja« (mentor: prof. dr. Marko Starbek)

Information for Authors

All manuscripts must be in English. Pages should be numbered sequentially. The manuscript should be composed in accordance with the Article Template given above. The maximum length of contributions is 10 pages. Longer contributions will only be accepted if authors provide juastification in a cover letter. For full instructions see the Information for Authors section on the journal's website: http://en.sv-jme.eu .

SUBMISSION:

Submission to SV-JME is made with the implicit understanding that neither the manuscript nor the essence of its content has been published previously either in whole or in part and that it is not being considered for publication elsewhere. All the listed authors should have agreed on the content and the corresponding (submitting) author is responsible for having ensured that this agreement has been reached. The acceptance of an article is based entirely on its scientific merit, as judged by peer review. Scientific articles comprising simulations only will not be accepted for publication; simulations must be accompanied by experimental results carried out to confirm or deny the accuracy of the simulation. Every manuscript submitted to the SV-JME undergoes a peer-review process.

The authors are kindly invited to submit the paper through our web site: http://ojs.sv-jme.eu. The Author is able to track the submission through the editorial process - as well as participate in the copyediting and proofreading of submissions accepted for publication - by logging in, and using the username and password provided.

SUBMISSION CONTENT:

The typical submission material consists of:

- A **manuscript** (A PDF file, with title, all authors with affiliations, abstract, keywords, highlights, inserted figures and tables and references),
- Supplementary files:
  - a **manuscript** in a WORD file format
  - a **cover letter** (please see instructions for composing the cover letter)
  - a ZIP file containing **figures** in high resolution in one of the graphical formats (please see instructions for preparing the figure files)
  - possible **appendicies** (optional), cover materials, video materials, etc.

Incomplete or improperly prepared submissions will be rejected with explanatory comments provided. In this case we will kindly ask the authors to carefully read the Information for Authors and to resubmit their manuscripts taking into consideration our comments.

COVER LETTER INSTRUCTIONS:

Please add a **cover letter** stating the following information about the submitted paper:

1. Paper **title**, list of **authors** and their **affiliations**.
2. **Type of paper**: original scientific paper (1.01), review scientific paper (1.02) or short scientific paper (1.03).
3. A **declaration** that neither the manuscript nor the essence of its content has been published in whole or in part previously and that it is not being considered for publication elsewhere.
4. State the **value of the paper** or its practical, theoretical and scientific implications. What is new in the paper with respect to the state-of-the-art in the published papers? Do not repeat the content of your abstract for this purpose.
5. We kindly ask you to suggest at least two **reviewers** for your paper and give us their names, their full affiliation and contact information, and their scientific research interest. The suggested reviewers should have at least two relevant references (with an impact factor) to the scientific field concerned; they should not be from the same country as the authors and should have no close connection with the authors.

FORMAT OF THE MANUSCRIPT:

The manuscript should be composed in accordance with the Article Template. The manuscript should be written in the following format:

- A **Title** that adequately describes the content of the manuscript.
- A list of **Authors** and their **affiliations**.
- An **Abstract** that should not exceed 250 words. The Abstract should state the principal objectives and the scope of the investigation, as well as the methodology employed. It should summarize the results and state the principal conclusions.
- 4 to 6 significant **key words** should follow the abstract to aid indexing.
- 4 to 6 **highlights;** a short collection of bullet points that convey the core findings and provide readers with a quick textual overview of the article. These four to six bullet points should describe the essence of the research (e.g. results or conclusions) and highlight what is distinctive about it.
- An **Introduction** that should provide a review of recent literature and sufficient background information to allow the results of the article to be understood and evaluated.
- A **Methods** section detailing the theoretical or experimental methods used.
- An **Experimental section** that should provide details of the experimental set-up and the methods used to obtain the results.
- A **Results** section that should clearly and concisely present the data, using figures and tables where appropriate.
- A **Discussion** section that should describe the relationships and generalizations shown by the results and discuss the significance of the results, making comparisons with previously published work. (It may be appropriate to combine the Results and Discussion sections into a single section to improve clarity.)
- A **Conclusions** section that should present one or more conclusions drawn from the results and subsequent discussion and should not duplicate the Abstract.
- **Acknowledgement** (optional) of collaboration or preparation assistance may be included. Please note the source of funding for the research.
- **Nomenclature** (optional). Papers with many symbols should have a nomenclature that defines all symbols with units, inserted above the references. If one is used, it must contain all the symbols used in the manuscript and the definitions should not be repeated in the text. In all cases, identify the symbols used if they are not widely recognized in the profession. Define acronyms in the text, not in the nomenclature.
- **References** must be cited consecutively in the text using square brackets [1] and collected together in a reference list at the end of the manuscript.
- **Appendix(-icies)** if any.

SPECIAL NOTES

Units: The SI system of units for nomenclature, symbols and abbreviations should be followed closely. Symbols for physical quantities in the text should be written in italics (e.g. *v*, *T*, *n*, etc.). Symbols for units that consist of letters should be in plain text (e.g. ms^{-1}, K, min, mm, etc.). Please also see: http://physics.nist.gov/cuu/pdf/sp811.pdf .

Abbreviations should be spelt out in full on first appearance followed by the abbreviation in parentheses, e.g. variable time geometry (VTG). The meaning of symbols and units belonging to symbols should be explained in each case or cited in a **nomenclature** section at the end of the manuscript before the References.

Figures (figures, graphs, illustrations digital images, photographs) must be cited in consecutive numerical order in the text and referred to in both the text and the captions as Fig. 1, Fig. 2, etc. Figures should be prepared without borders and on white grounding and should be sent separately in their original formats. If a figure is composed of several parts, please mark each part with a), b), c), etc. and provide an explanation for each part in Figure caption. The caption should be self-explanatory. Letters and numbers should be readable (Arial or Times New Roman, min 6 pt with equal sizes and fonts in all figures). Graphics (submitted as supplementary files) may be exported in resolution good enough for printing (min. 300 dpi) in any common format, e.g. TIFF, BMP or JPG, PDF and should be named Fig1.jpg, Fig2.tif, etc. However, graphs and line drawings should be prepared as vector images, e.g. CDR, AI. Multi-curve graphs should have individual curves marked with a symbol or otherwise provide distinguishing differences using, for example, different thicknesses or dashing.

Tables should carry separate titles and must be numbered in consecutive numerical order in the text and referred to in both the text and the captions as Table 1, Table 2, etc. In addition to the physical quantities, such as *t* (in italics), the units [s] (normal text) should be added in square brackets. Tables should not duplicate data found elsewhere in the manuscript. Tables should be prepared using a table editor and not inserted as a graphic.

REFERENCES:

A reference list must be included using the following information as a guide. Only cited text references are to be included. Each reference is to be referred to in the text by a number enclosed in a square bracket (i.e. [3] or [2] to [4] for more references; do not combine more than 3 references, explain each). No reference to the author is necessary.

References must be numbered and ordered according to where they are first mentioned in the paper, not alphabetically. All references must be complete and accurate. Please add DOI code when available. Examples follow.

Journal Papers:

Surname 1, Initials, Surname 2, Initials (year). Title. Journal, volume, number, pages, DOI code.

[1] Hackenschmidt, R., Alber-Laukant, B., Rieg, F. (2010). Simulating nonlinear materials under centrifugal forces by using intelligent cross-linked simulations. *Strojniški vestnik - Journal of Mechanical Engineering,* vol. 57, no. 7-8, p. 531-538, DOI:10.5545/sv-jme.2011.013.

Journal titles should not be abbreviated. Note that journal title is set in italics.

Books:

Surname 1, Initials, Surname 2, Initials (year). Title. Publisher, place of publication.

[2] Groover, M.P. (2007). *Fundamentals of Modern Manufacturing*. John Wiley & Sons, Hoboken.

Note that the title of the book is italicized.

Chapters in Books:

Surname 1, Initials, Surname 2, Initials (year). Chapter title. Editor(s) of book, book title. Publisher, place of publication, pages.

[3] Carbone, G., Ceccarelli, M. (2005). Legged robotic systems. Kordić, V., Lazinica, A., Merdan, M. (Eds.), Cutting Edge Robotics. Pro literatur Verlag, Mammendorf, p. 553-576.

Proceedings Papers:

Surname 1, Initials, Surname 2, Initials (year). Paper title. Proceedings title, pages.

[4] Štefanić, N., Martinčević-Mikić, S., Tošanović, N. (2009). Applied lean system in process industry. *MOTSP Conference Proceedings*, p. 422-427.

Standards:

Standard-Code (year). Title. Organisation. Place.

[5] ISO/DIS 16000-6.2:2002. *Indoor Air – Part 6: Determination of Volatile Organic Compounds in Indoor and Chamber Air by Active Sampling on TENAX TA Sorbent, Thermal Desorption and Gas Chromatography using MSD/FID.* International Organization for Standardization. Geneva.

WWW pages:

Surname, Initials or Company name. Title, from http://address, date of access.

[6] Rockwell Automation. Arena, from *http://www.arenasimulation.com,* accessed on 2009-09-07.

EXTENDED ABSTRACT:

When the paper is accepted for publishing, the authors will be requested to send an **extended abstract** (approx. one A4 page or 3500 to 4000 characters). The instruction for composing the extended abstract are published on-line: http://www.sv-jme.eu/information-for-authors/ .

COPYRIGHT:

Authors submitting a manuscript do so on the understanding that the work has not been published before, is not being considered for publication elsewhere and has been read and approved by all authors. The submission of the manuscript by the authors means that the authors automatically agree to transfer copyright to SV-JME when the manuscript is accepted for publication. All accepted manuscripts must be accompanied by a Copyright Transfer Agreement, which should be sent to the editor. The work should be original work by the authors and not be published elsewhere in any language without the written consent of the publisher. The proof will be sent to the author showing the final layout of the article. Proof correction must be minimal and executed quickly. Thus it is essential that manuscripts are accurate when submitted. Authors can track the status of their accepted articles on http://en.sv-jme.eu/.

PUBLICATION FEE:

Authors will be asked to pay a publication fee for each article prior to the article appearing in the journal. However, this fee only needs to be paid after the article has been accepted for publishing. The fee is 240.00 EUR (for articles with maximum of 6 pages), 300.00 EUR (for articles with maximum of 10 pages), plus 30.00 EUR for each additional page. The additional cost for a color page is 90.00 EUR. These fees do not include tax.

Strojniški vestnik -Journal of Mechanical Engineering
Aškerčeva 6, 1000 Ljubljana, Slovenia,
e-mail: info@sv-jme.eu

9 770039 248001
ISSN 0039-2480

http://www.sv-jme.eu

Contents

Papers

263 Jurij Iljaž, Leopold Škerget, Mitja Štrakl, Jure Marn:
Optimization of SAE Formula Rear Wing

273 Ayyanar Athijayamani, Raju Ganesamoorthy, Konda Thulasiraman Loganathan, Susaiyappan Sidhardhan:
Modelling and Analysis of the Mechanical Properties of Agave Sisalana Variegata Fibre / Vinyl Ester Composites Using Box-Behnken Design of Response Surface Methodology

281 Van Tuan Do, Le Cuong Nguyen:
Adaptive Empirical Mode Decomposition for Bearing Fault Detection

291 Luca Petan, José Luis Ocaña, Janez Grum:
Effects of Laser Shock Peening on the Surface Integrity of 18% Ni Maraging Steel

299 K Priya Ajit, Abhinav Gautam, Prabir Kumar Sarkar:
Ductile Behaviour characterization of Low Carbon Steel: a CDM Approach

307 David Kaljun, Jože Petrišič, Janez Žerovnik:
Using Newton's Method to Model the Spatial Light Distribution of an LED with Attached Secondary Optics

318 Mohammadreza Kamali, Seyed Ali Jazayeri, Farid Najafi, Kenji Kawashima, Toshiharu Kagawa:
Study on the Performance and Control of a Piezo-Actuated Nozzle-Flapper Valve with an Isothermal Chamber